DEPARTMENT OF COMMERCE
LUTHER H. HODGES, Secretary

WEATHER BUREAU
F. W. REICHELDERFER, Chief

MONTHLY WEATHER REVIEW

JAMES E. CASKEY, JR., Editor

Volume 89, Number 12 | Washington, D.C. | December 1961

ON THE RADIATIVE EQUILIBRIUM AND HEAT BALANCE OF THE ATMOSPHERE

SYUKURO MANABE

U.S. Weather Bureau, Washington, D.C.
and

FRITZ MÖLLER

Meteorological Institute, University of Munich
[Manuscript received April 20, 1961; revised September 22, 1961]

ABSTRACT

In order to incorporate the effect of radiation into the numerical experiment of the general circulation of the atmosphere, a simplified scheme for computing the radiative temperature change is constructed. The effects included are long wave radiation by water vapor, carbon dioxide, and ozone and the absorption of solar radiation by these three gases. The absorptivities of these gases are determined based upon the recent results of laboratory experiments and those of theoretical computations. The effects of clouds are not included.

By use of this scheme the radiative equilibrium temperature is computed for various latitudes and seasons as asymptotic solutions of an initial value problem. To a certain degree the radiative equilibrium solutions reveal some of the typical characteristics of stratospheric temperature and tropopause height variations.

Radiative heat budgets of the atmosphere are also computed and compared with the results of the computations of radiative equilibrium. This comparison is helpful for understanding the role of radiative processes and also suggests the kinds of effect we should expect from other thermal processes in the atmosphere.

CONTENTS

1. Introduction 503
2. Temperature change due to long wave radiation 505
Water vapor 506
Carbon dioxide and ozone 506
Pressure and temperature effect 507
Overlapping 507
3. Temperature change due to absorption of solar radiation 507
4. Absorptivities of long wave radiation 508
Water vapor 508
Carbon dioxide 509
Ozone 510
5. Absorptivities of solar radiation 511
Water vapor 511
Carbon dioxide 512
Ozone 513
6. Distribution of gases 513
Water vapor 513
Carbon dioxide 514
Ozone 514
7. Computation of radiative equilibrium 514
8. Discussion of results 517
Radiative equilibrium 517
Heat budget 525
9. Conclusions 528
10. Critical comments and future work 529
Acknowledgments 529
Appendix I. Vertical coordinate system 529
Appendix II. Emissivities and absorptivities 530
Appendix III. Finite difference equations 530
References 530

1. INTRODUCTION

One of the most successful attempts in the study of the general circulation of the atmosphere was the numerical experiment performed by Phillips [49]. Assuming a steady heat source and sink in low and high latitudes respectively, and numerically integrating the system of the equations of motion and the thermodynamical equation, he obtained a latitudinal distribution of temperature

with such typical characteristics of the actual atmosphere as the polar front accompanied by a strong jet stream. This study has been further extended by Smagorinsky [57]. After assuming distributions of heat source and sink corresponding to winter and summer, his calculation exhibited the typical polar front accompanied by very strong cyclone waves in winter, and rather small pole to equator temperature contrast with very weak baroclinic activities in summer. Though the contrast between summer and winter which he obtained is too large, due to the lack of oceans in his model, this experiment provides very good clues to our understanding of the mechanism of seasonal variations of temperature and wind field in the atmosphere.

However, for the sake of computational simplicity, both of these calculations are based upon a two-level model. As a natural consequence of this simplification the static stability was assumed constant with space and time. This model, therefore, is not capable of simulating the vertical temperature distribution of the atmosphere. It is a very challenging problem, however, to simulate the latitudinal distribution of the height of the tropopause, that of the temperature in the stratosphere, and the polar inversion in the lower troposphere. In order to do this it is necessary to build a model which has a high resolution (many levels) in the vertical direction and which includes the various thermal processes acting in the atmosphere, i.e., radiation, condensation, and the eddy flux of sensible and latent heat from the earth's surface. In the present work, a scheme was constructed for the numerical computation of radiative temperature change suitable for incorporation into an advanced general circulation model.

In order to ascertain provisionally the behavior of this scheme, we performed many numerical computations and obtained various distributions of radiative equilibrium temperature as the asymptotic solutions of marching computations from certain initial conditions. In spite of the extreme simplicity of the model, this approach appeared to be very effective for obtaining insight into the role of the radiative processes in maintaining the observed atmospheric temperature distributions.

Theoretical study of the radiative equilibrium of the atmosphere started just after the discovery of the tropopause by Teisserenc de Bort and Assman in 1902. The pioneer theories were those of Humphreys [24], Gold [19], and Emden [12], which were based upon the assumption of gray radiation. Emden computed the vertical distribution of radiative equilibrium temperature as the balance between the heating due to the absorption of solar radiation by water vapor and the cooling due to the long wave radiation of water vapor. His result showed a nearly isothermal layer above the level of 6–8 km. supposedly corresponding to the stratosphere. Below this level there existed the layer of superadiabatic lapse rates which could cause strong convection and corresponds to the troposphere.

This was a successful first step in the study of this field. However, the water vapor absorptivity of terrestrial radiation adopted by Emden, under the assumption of gray radiation, is very different from that obtained by many authors from observations and laboratory experiments. Möller [39] pointed out this difference and recomputed the radiative equilibrium by subdividing the water vapor spectrum into two intervals. His revised computation shows a very low stratospheric temperature approaching −137° C. at the top of the atmosphere and a lapse rate of 0.3° C./100 m. in the stratosphere instead of the isothermal layer obtained by Emden. Based upon these results, he concluded that it is impossible to explain the temperature distribution of the stratosphere by a radiative equilibrium computation including only the effect of water vapor. More recently, King [33] and Yamamoto [71] computed the line absorbing atmosphere in which the absorption coefficients were given by Lorentz's collision broadening formula and Elsasser line shape respectively. Neither of these results shows the inversion in the stratosphere. Although Kaplan [31] obtained the inversion by schematically interpolating the King results, this schematic interpolation seems to be ambiguous.

On the other hand, Gowan [22] computed the distribution of radiative equilibrium temperature of the stratosphere and obtained an *increase* of temperature with altitude by taking into consideration the heating due to the absorption of solar ultraviolet radiation by ozone as well as the effect of long wave radiation by water vapor. In the improved version of his computation [23] he also included the effects of the 15μ band of carbon dioxide, the 9.6μ band of ozone, and the absorption of solar radiation by water vapor. The equilibrium temperature of the stratosphere thus obtained increases with altitude and qualitatively coincides with observed features. Quantitatively, however, the temperatures are much warmer than those observed. This computation could be further improved by adopting recent observations of the extraterrestrial solar spectrum and the distribution of gases in the stratosphere as well as the absorptivities recently obtained in the laboratory.

The explanation of the temperature increase in the lower stratosphere with increasing latitude is also a difficult task. Möller [40] presented the theory that the overlapping of the ozone band at 14μ and the carbon dioxide band at the same wavelength might be responsible for this increase. As the total amount of ozone increases with increasing latitude, its sheltering effect also increases and a smaller part of carbon dioxide emission leaves the atmosphere. Accordingly, the temperature of the stratosphere could increase with increasing latitude. Quantitatively speaking, however, the intensity of the 14μ band of ozone is much too weak to cause the observed sharp increase of temperature with latitude.

In 1946, Dobson, Brewer, and Cwilong [10] presented a theory of radiative equilibrium which considered the effect

of the 9.6μ band of ozone and the 15μ band of carbon dioxide as well as the long wave radiation by water vapor. In this paper, they beautifully explained the latitudinal distributions and seasonal variation of stratospheric temperature based mainly on the distributions of ozone. Though the 9.6μ band of ozone is much stronger than the 14μ band of ozone, and might have significant effects, the discussion was qualitative and somewhat unverified.

On the other hand, Goody [20] presented a theory which seems to be rather contradictory to the ideas of Dobson's group. He insists that the effect of ozone is of minor importance and explained the latitudinal variation of the tropopause height and of the temperature as a balance between the heating effect of carbon dioxide and the cooling effect of water vapor.

More recently, Ohring [48] computed the radiative heat balance of the stratosphere and concluded that the radiative processes tend to heat the stratosphere in lower latitudes and cool it in higher latitudes. The remarkable differences among the results of these authors suggest the necessity of careful examination of these results as well as quantitative studies of the thermal equilibrium and the heat balance of the atmosphere.

In the present work we took into consideration the effects of the absorption of solar radiation by water vapor, carbon dioxide, and ozone as well as those of the long wave radiation of these three gases. With the aid of recent information on the distributions and absorptivities of these gases, we then computed the distribution of equilibrium temperature for various latitudes and seasons. In addition, in order to investigate the degree of radiative imbalance in observed conditions, the distribution of radiative heat budget was also computed. Based upon these results and the examination of the results of other authors, we tried to determine to what degree we could explain the temperature distribution of the atmosphere by radiative processes and what we should attribute to thermal processes other than radiation, e.g., heat transfer due to large scale disturbances, to the meridional circulation, and to dry or moist convection in the atmosphere.

In recent years, various speculations on the general circulation of the upper troposphere and stratosphere have been inferred from the distribution of the gases such as ozone and water vapor and of radioactive debris introduced into the high atmosphere by atomic explosions (Machta [38]). It is therefore hoped that the comparison of present results with these speculations will shed some light in understanding the thermal processes of the atmosphere.

2. TEMPERATURE CHANGE DUE TO LONG WAVE RADIATION

The absorption bands which mainly contribute to the long wave radiation of the atmosphere are the 6.3μ band and the rotation band of water vapor, the 15μ band of carbon dioxide, and the 9.6μ band of ozone. The rate of the resultant change of temperature at height z due to the long wave radiation is

$$\left(\frac{\partial T_z}{\partial t}\right)_{LR}^{G}=-\frac{1}{c_p\rho}\frac{\partial F_z^G}{\partial z} \tag{1}$$

where subscript LR is the abbreviation of long wave radiation, superscript G stands for water vapor (W), carbon dioxide (C), or ozone (O), c_p is the specific heat of air under constant pressure, ρ is the density of air, and the net flux F_z^G is the difference of upward and downward flux, for each wave number interval chosen i.e.,

$$F_z^G=U_z^G-D_z^G. \tag{2}$$

Adding the contribution of the above mentioned three gases, we get the total rate of temperature change due to the long wave radiation as

$$\left(\frac{\partial T_z}{\partial t}\right)_{LR}=\left(\frac{\partial T_z}{\partial t}\right)_{LR}^{W}+\left(\frac{\partial T_z}{\partial t}\right)_{LR}^{C}+\left(\frac{\partial T_z}{\partial t}\right)_{LR}^{O}. \tag{3}$$

Next, we shall describe how we computed the net flux due to these gases. By solving the equation of radiative transfer with the boundary condition that downward long wave radiation is zero at the top of the atmosphere and adopting the method of integration by parts we can express the downward flux of radiation at height z due to any absorption band as

$$D_z=\int_{\nu_1}^{\nu_2}\pi B_\nu(T_z)d\nu-\int_{\nu_1}^{\nu_2}\pi B_\nu(T_\infty)\cdot\tau_f(\chi_\infty)d\nu+\int_{\nu_1}^{\nu_2}\left\{\int_{T_z}^{T_\infty}\pi\frac{dB_\nu}{dT}\tau_f(\chi)dT\right\}d\nu \tag{4}$$

where $B_\nu(T)$ is the blackbody radiation of frequency ν at temperature T, τ_f is the transmission function of the slab, ν_1 and ν_2 are the band limits, T_z and T_∞ are the temperature at level z and at the top of the atmosphere respectively, and

$$\chi(T)=\left|\int_{u(T_z)}^{u(T)}k_\nu du\right|, \qquad (\chi_\infty=\chi(T_\infty)). \tag{5}$$

In equation (5), k_ν is the absorption coefficient at frequency ν, and $u(T)$ is the amount of absorber existing between the earth's surface and the level of temperature T. Assuming that the upward radiation at the earth's surface is equal to the blackbody radiation of surface temperature, we could obtain the upward flux of atmospheric radiation at height z in the same way, i.e.,

$$U_z=\int_{\nu_1}^{\nu_2}\pi B_\nu(T_z)d\nu+\int_{\nu_1}^{\nu_2}\left\{\int_{T_z}^{T_s}\pi\frac{dB_\nu}{dT}\tau_f(\chi)dT\right\}d\nu \tag{6}$$

where T_s is the temperature of the earth's surface.

Exact integration of equations (4) and (6) requires a

tremendous amount of computation. Therefore, an attempt was made to simplify these equations. The absorption bands of water vapor cover almost the entire spectrum of atmospheric radiation, whereas those of carbon dioxide and ozone have rather narrow band widths. Accordingly, there are some differences between our approximations adopted for the computation of long wave radiation by water vapor and those adopted for the computation for carbon dioxide and ozone. For the sake of convenience we shall describe them separately hereafter.

WATER VAPOR

In order to simplify the computation of equations (4) and (6) Yamamoto [68] introduced the following mean transmissivity of slab:

$$\tilde{\tau}_f(u,T)=\frac{1}{\frac{dB}{dT}}\int_0^\infty \frac{dB_\nu}{dT}\,\tau_f(k_\nu u)d\nu \tag{7}$$

where

$$\frac{dB}{dT}=\int_0^\infty \frac{dB_\nu}{dT}\,d\nu. \tag{8}$$

Corresponding to this mean transmissivity of the slab, one can define the mean absorptivity of the slab as

$$\tilde{\epsilon}_f(u,T)=1-\tilde{\tau}_f(u,T). \tag{9}$$

The emissivity of the slab of water vapor is by definition

$$\epsilon_f(u,T)=\frac{1}{B(T)}\int_0^\infty B_\nu(T)\cdot\{1-\tau_f(k_\nu u)\}d\nu \tag{10}$$

where

$$B(T)=\int_0^\infty B_\nu(T)d\nu=\frac{1}{\pi}(\sigma T^4) \tag{11}$$

and σ is the Stefan-Boltzmann constant.

By using $\tilde{\epsilon}_f$ and ϵ_f defined above and neglecting the temperature dependence of k_ν on T, equation (4) could be approximately transformed into the following form:

$$D_z^W\approx\pi B_\infty\cdot\epsilon_f^W(y_\infty,T_\infty)-\int_{B_z}^{B_\infty}\tilde{\epsilon}_f^W(y,T)\pi dB$$

or referring to equations (7), (9), and (10),

$$D_z^W\approx\pi B_c\cdot\epsilon_f^W(y_\infty,T_c)-\int_{B_\infty}^{B_c}\tilde{\epsilon}_f^W(y_\infty,T)\pi dB-\int_{B_z}^{B_\infty}\tilde{\epsilon}_f^W(y,T)\pi dB \tag{12}$$

where

$$y(B(T))=|u(T)-u(T_z)|,\qquad (y_\infty=|u(T_\infty)-u(T_z)|), \tag{13}$$

superfix W corresponds to water vapor, $B_s=B(T_s)$, $B_\infty=B(T_\infty)$, $B_c=B(T_c)$, and T_c is the temperature specially selected for the convenience of integration. Examination of the table of $\tilde{\tau}_f^W(=1-\tilde{\epsilon}_f^W)$ constructed by Yamamoto [68] for the wide range of temperature reveals that $\tilde{\epsilon}_f^W$ is almost independent of temperature for the temperature range of 200°–300°K., i.e., for the range of atmospheric temperature. Below 200°K. it decreases significantly with decreasing temperature. Therefore, if we choose T_c larger than 200°K., we may safely assume that $\tilde{\epsilon}_f^W$ is independent of temperature. For our computation we adopted 220°K. as T_c. Accordingly, ϵ_f^W and $\tilde{\epsilon}_f^W$ were computed for T=220°K. and T=300°K. respectively. For further details of this computation refer to Section 4.

The equation (6) for the upward flux is to be transformed into the following equation:

$$U_z^W=\pi B_s-\int_{B_z}^{B_s}\tilde{\epsilon}_f^W(y,T)\pi dB \tag{14}$$

where $B_s=B(T_s)$. When the sky is clear, it is more convenient to use the following expression for net flux F_z^W.

$$F_z^W=U_z^W-D_z^W=\pi B_s-\pi B_c\cdot\epsilon_f^W(y_\infty,T_c)-\int_{B_\infty}^{B_s}\tilde{\epsilon}_f^W(y,T)\pi dB-\int_{B_c}^{B_\infty}\tilde{\epsilon}_f^W(y_\infty,T)\pi dB. \tag{15}$$

CARBON DIOXIDE AND OZONE

For the 15μ band of carbon dioxide and the 9.6μ band of ozone, the mean slab absorptivity of the band instead of that of the entire spectrum was introduced, i.e.,

$$\mathcal{E}_f(u,T)=\frac{1}{\nu_2-\nu_1}\int_{\nu_1}^{\nu_2}[1-\tau_f(k_\nu u)]d\nu. \tag{16}$$

Because the band width of these bands is narrow enough to neglect the dependence of dB_ν/dT upon the wave number inside the band, equations (4) and (6), which express the downward and upward radiation respectively, could be changed into the following approximate forms:

$$D_z^G\approx\pi b_\infty^G\cdot\mathcal{E}_f^G(y_\infty,\overline{T})-\int_{b_z^G}^{b_\infty^G}\mathcal{E}_f^G(y,\overline{T})\pi db^G \tag{17}$$

$$U_z^G\approx\pi b_s^G-\int_{b_z^G}^{b_s^G}\mathcal{E}_f^G(y,\overline{T})\pi db^G \tag{18}$$

where superscript G stands either for carbon dioxide or for ozone, $\overline{T}$ is the temperature of isothermal layer which has the same mean band absorptivity and the same distribution of gas as the layer with which we are concerned, b^G is defined as:

$$b^G(T)=\int_{\nu_1^G}^{\nu_2^G}B_\nu(T)d\nu \tag{19}$$

and b_∞^G, b_z^G and b_s^G are the abbreviations of $b^G(T_\infty)$, $b^G(T_z)$,

and $b^G(T_s)$ respectively. Subtracting D_z^G from U_z^G, the net flux F_z^G is

$$F_z^G=\pi b_s^G-\pi b_\infty^G\cdot\mathcal{E}_f^G(y_\infty,\overline{T})-\int_{b_\infty^G}^{b_s^G}\mathcal{E}_f^G(y,\overline{T})\pi db^G. \quad (20)$$

PRESSURE AND TEMPERATURE EFFECT

Owing to the pressure broadening of line shape the mean absorptivity is also a function of pressure of the layer with which we are concerned. Therefore, it is necessary to take into consideration this effect. Recently, Howard, Burch, and Williams [27] measured the mean absorptivity due to each absorption band of both water vapor and carbon dioxide for various absorber concentrations and various total pressures. According to their results, the mean absorptivity of the layer with uniform pressure could be obtained from the mean absorptivity curve for standard pressure by replacing the optical thickness of the layer u by the effective optical thickness of the layer u_r expressed by the following equation:

$$u_r=\Big((P+p)/P_0\Big)^\kappa u \quad (21)$$

where κ is the constant which is usually smaller than unity and is different for each absorption band, P is the total pressure, p is the partial pressure of the absorbing gas, and P_0 is the standard pressure. As is well known, the actual absorption band is the mixture of strong lines and weak lines. When the intensity of a line is very weak or an absorbing gas is very thin, the amount of absorption is proportional to the product of line intensity and the amount of gas and is independent of pressure. This is the reason why κ is usually smaller than 1, despite the fact that a half-width of the line is proportional to pressure.

Strictly speaking, κ is not constant and depends upon amount of absorbing gas and pressure. When the amount of gas is small, κ decreases significantly with decreasing amount of the gas. However, since the thickness of each layer adopted for our numerical computation is thick enough, the assumption of constant κ does not cause serious error. It would be desirable, of course, to adopt a better approximation as soon as more accurate experiments for a wider range of pressure are available.

Since pressure decreases with altitude and $P\gg p$ in the actual atmosphere, the following equation was adopted for the computation of the effective optical thickness of the atmospheric layers instead of equation (21).

$$u_r\approx\int_{u(P_1)}^{u(P_2)}(P/P_0)^\kappa du \quad (22)$$

where, for example, $u(P_1)$ is the optical thickness between the level of total pressure P_1 and the earth's surface. As pointed out by Kaplan [31] linear scaling tends to overestimate the pressure effect for the moderately weak lines. In this paper, we shall consistently adopt this κ scaling instead of linear scaling.

Temperature also affects the intensity as well as the half width of the absorption lines. However, as far as we know, no suitable measurement has yet been made below room temperature. According to the theoretical estimation of Plass [50, 51], temperature hardly affects the absorption due to the 9.6μ band of ozone but is rather important for the absorption of the 15μ band of carbon dioxide. Therefore, the temperature dependence on absorptivity of the 15μ band of carbon dioxide was incorporated into our computation of heat balance. For the sake of convenience of description, the detailed method of doing this will be described in section 4.

OVERLAPPING

So far we have treated the contributions of the absorption bands of the various gases interdependently; however, the effect of overlapping among these bands deserves attention. The overlapping between the 9.6μ band of ozone and the absorption band of water vapor is not important except near the equator where water vapor is abundant, because water vapor is almost transparent for the radiation of this wavelength. On the other hand, the effect of overlapping between the 15μ band of carbon dioxide and the rotation band of water vapor is not negligible. The mere addition of the contributions of these two gases could give us a fictitious resultant emissivity which is larger than 100 percent. In our computations we made the approximation that water vapor is completely transparent for this overlapped frequency range. In the lower troposphere this approximation would probably be no better than Elsasser's [11] approximation based upon the assumption of complete blackness of the overlapped frequency range. However, in the upper troposphere and stratosphere, where the mixing ratio of water vapor is small and accordingly the absorption by the overlapped range of the rotation band of water vapor is small, the present approximation should be accurate. In order to obtain good accuracy everywhere it would be desirable to adopt the following approximate equation for the resultant slab absorptivity of the overlapped band, $\mathcal{E}_f^{OV}(u^W,u^C)$ (Yamamoto [68]),

$$\begin{aligned}\mathcal{E}_f^{OV}(u^W,u^C)&\approx 1-(1-\mathcal{E}_f^{WOV}(u^W))\cdot(1-\mathcal{E}_f^C(u^C))\\&=\mathcal{E}_f^C(u^C)+\mathcal{E}_f^{WOV}(u^W)\,(1-\mathcal{E}_f^C(u^C))\end{aligned} \quad (23)$$

where $\mathcal{E}_f^{WOV}$ is the mean slab absorptivity of water vapor for the overlapped frequency range. Our approximations correspond to the neglect of the second term on the right side of equation (23).

3. TEMPERATURE CHANGE DUE TO THE ABSORPTION OF SOLAR RADIATION.

The absorption of solar radiation by water vapor, carbon dioxide, and ozone was included in our computa-

tion. If we neglect the effect of overlapping among the absorptions of different gases, the equation for the rate of temperature change at height z due to these absorptions is

$$\left(\frac{\partial T_z}{\partial t}\right)_{SR}=\left(\frac{\partial T_z}{\partial t}\right)^{W}_{SR}+\left(\frac{\partial T_z}{\partial t}\right)^{C}_{SR}+\left(\frac{\partial T_z}{\partial t}\right)^{O}_{SR} \tag{24}$$

where $(\partial T_z/\partial t)^{W}_{SR}$, $(\partial T_z/\partial t)^{C}_{SR}$, and $(\partial T_z/\partial t)^{O}_{SR}$ are the rates of temperature change due to water vapor, ozone, and carbon dioxide respectively, and subscript SR is the abbreviation of solar radiation. The rate of temperature change at height z due to each gas is

$$\left(\frac{\partial T_z}{\partial t}\right)^{G}_{SR}=-\frac{\cos\zeta}{c_p\cdot\rho}\cdot\frac{\partial}{\partial z}\left[a^G\{(u_\infty-u_z)\sec\zeta\}\right] \tag{25}$$

where a^G is the amount of absorption of solar radiation as the function of optical thickness, and ζ is the zenith distance of the sun. In order to compute the equilibrium temperature of the atmosphere, it is necessary to get the expression for the rate of daily mean temperature change. The daily mean rate of temperature change at height z due to the absorption of solar radiation by gas G is

$$\overline{\left(\frac{\partial T_z}{\partial t}\right)^{G}_{SR}}=\frac{1}{(whole\ day)}\left[-\frac{\cos\zeta}{c_p\rho}\cdot\int^{(daytime)}\frac{\partial}{\partial z}[a^G\{(u_\infty-u_z)\sec\zeta\}]dt\right] \tag{26}$$

which could be approximately expressed as

$$\overline{\left(\frac{\partial T_z}{\partial t}\right)^{G}_{SR}}\approx\frac{(daytime)}{(whole\ day)}\left[-\frac{\cos\bar{\zeta}}{c_p\cdot\rho}\frac{\partial}{\partial z}[a^G\{(u_\infty-u_z)/\cos\bar{\zeta}\}]\right] \tag{27}$$

where $\bar{\zeta}$ is the mean zenith angle defined in the following way:

$$\cos\bar{\zeta}=\left(\int^{(daytime)}\cos\zeta(t)dt\right)\Big/\left(\int^{(daytime)}dt\right) \tag{28}$$

The mean cosine of the zenith angle and the length of daytime given in parts of 24 hours for each season and latitude, which are used in our computation, are tabulated in table 1.

TABLE 1.—*The seasonal and latitudinal distributions of the length of the daytime given in parts of 24 hours and those of the weighted mean values of cos ζ. (See table 6 of [36].*

°Lat.	Fractional length of daytime				Cos$\bar{\zeta}$			
	Apr.	July	Oct.	Jan.	Apr.	July	Oct.	Jan.
5	.508	.517	.500	.496	.625	.587	.614	.591
15	.521	.537	.492	.471	.618	.601	.579	.549
25	.533	.562	.483	.450	.599	.593	.524	.474
35	.546	.596	.471	.421	.558	.567	.458	.393
45	.562	.637	.454	.392	.501	.521	.379	.317
55	.596	.708	.437	.321	.423	.453	.282	.203
65	.629	.837	.404	.208	.345	.369	.176	.106
75	.750	1.000	.329	----	.241	.311	.071	----
85	1.000	1.000	----	----	.168	.318	----	----

The effect of pressure broadening of the absorption lines was taken into consideration in the same way as for the long wave radiation. The values of κ which should be adopted for the absorption of solar radiation by each gas will be discussed later.

There is an overlapping between the 2.7μ band of water vapor and that of carbon dioxide. In the lower troposphere where the water vapor is abundant, the mere addition of these two contributions causes an overestimation of the absorption of solar radiation by this band. However, in the troposphere the relative magnitude of the absorption by carbon dioxide is so small that it does not matter whether we include this effect of overlapping or not. For the sake of simplifying the computation scheme, we add the contributions of two gases neglecting the effect of this overlapping.

4. ABSORPTIVITIES OF LONG WAVE RADIATION

In order to compute the temperature change due to the long wave radiation of the atmosphere, it is necessary to know the emissivity or the absorptivity of diffuse radiation. In the laboratory, however, the absorptivity of the parallel beam is usually measured. Therefore, it is necessary to obtain the relation between the absorptivity of a column and that of a slab. For this purpose Elsasser [11] computed the transmissivities of both a slab and a column for an idealized band of equal and equidistant lines. Based upon these results, he obtained the following approximate relation.[1]

$$\tau^{E}_{f}(l,u)\approx\tau^{E}_{f}(1.66l,u) \tag{29}$$

where τ^{E}_{L} and τ^{E}_{f} are the general transmission function of a column and a slab for this idealized Elsasser band, and l_ν is the general absorption coefficient. This equation means that the effective optical thickness for isotropic diffuse radiation is 1.66 times larger than that for direct radiation. In this section we shall use this approximate relation for the reduction of the absorptivity of a slab from that of a column.

WATER VAPOR

An extensive study of the absorption bands of water vapor contributing to the terrestrial radiation was done by Yamamoto [68]. He obtained the value of the general absorption coefficient for the 6.3μ band, 8–13μ region, 17–24μ, and the far infrared region from the experiments by Fowle [16], Adel and Lampland [1], Weber and Randall [66], and the theoretical computations of Yamamoto and Onishi [67], respectively. According to his paper, the theoretical computation by Yamamoto and Onishi coincides well with the experimental results by Weber and Randall for the rotation band at 17–24μ but does not coincide with the experiments by Fowle for the rotation vibration band at 6.3μ, due probably to the crude approximation adopted in their theoretical computation for this

[1] This kind of approximation was first adopted by Robert [54].

band. Recently, careful and extensive experiments on this band were performed by Howard, Burch, and Williams [27] which coincide very well with the results of Fowle. This coincidence supports Yamamoto's choice of Fowle's experimental data for this band.

By using the general absorption coefficients for 300° K. and 220° K. and the general transmission function compiled by Yamamoto [68], we computed the mean slab absorptivity $\bar{\epsilon}_f(u^W, 300° \text{ K.})$ and slab emissivity $\epsilon_f(u^W, 220° \text{ K.})$, respectively, which are given in figure 1 for the logarithm (base 10) of varying optical thicknesses in the unit of centimeter of precipitable water. The contribution of the frequency range overlapped with the 15μ band of carbon dioxide (550–800/cm.) was not included in this computation.

The value of the pressure factor κ for the absorption bands of water vapor could be obtained from the experiments performed by Howard et al. [27] and Daw [9]. Howard et al. conducted laborious experiments on many infrared absorption bands of water vapor and carbon dioxide and proposed two types of relations which fit the experimental data. When the absorption is weak, the total absorption is given by the following equation of "weak fit":

$$\int_{\nu_1}^{\nu_2} A_\nu d\nu = C\{u\,(P+p)^\kappa\}^{1/2} \text{ (weak fit)}^2. \qquad (30)$$

For the stronger absorption the total absorption is given by the following equation of "strong fit":

$$\int_{\nu_1}^{\nu_2} A_\nu d\nu = C + D \log_{10}\{u\,(P+p)^\kappa\} \text{ (strong fit)}.^2 \qquad (31)$$

In table 2 the values of κ for the 6.3μ band and the rotation band are tabulated both for the strong and for the weak fit. Referring to this table, we assumed the effective mean κ-value for both the rotation band and the 6.3μ band to be 0.6.

In view of the fact that Daw's experiments do not cover the entire rotation band of water vapor and that the theoretical computation of line intensity of the rotation band is possible, it seems desirable to determine the κ-value for the rotation band based upon the theoretical computation. Before this sort of computation is done, we tentatively adopt the κ-value of 0.6.

CARBON DIOXIDE

Careful study of the absorptivity of the 15μ band of carbon dioxide was made by Howard, Burch, and Williams [27] for absorber concentration ranging from 1 to at least 1000 atmo-cm. of carbon dioxide and for various total pressures ranging from 20 mm. to 740 mm. Hg. They expressed their results by the equations of weak and strong fit as they did for the absorptivity of water vapor (refer to equations (30) and (31)). By using these empirical equations it is possible to construct the curve of the mean band absorptivity of a slab for the 15μ band of carbon dioxide.

According to their experiment, the pressure factor κ for a weak fit is 0.855 and that for a strong fit is 0.88. Based upon these values we assumed κ to be 0.86.

The dependence of absorptivity of this band on temperature is not always small. This was pointed out, for example, by Plass [51]. In order to calculate the temperature effect, we used the recent work of Sasamori [55] who theoretically computed the absorptivity of this band

TABLE 2.—*The value of κ for rotation band and 6.3μ band of water vapor**

Band	Band Limits (cm.$^{-1}$)	κ	Reference
Rot H_2O	436–655	0.60 (weak fit)	Daw [9]*.
Rot H_2O	655–896	.50 (weak fit)	Daw [9]*.
6.3μ	1150–2050	.60 (weak fit)	HBW [27].
		.72 (strong fit)	HBW [27].

*The κ-values for the rotation band were taken from p. 16-12 of the *Handbook of Geophysics* [18], where King gave the value of κ and other constants based upon Daw's data.

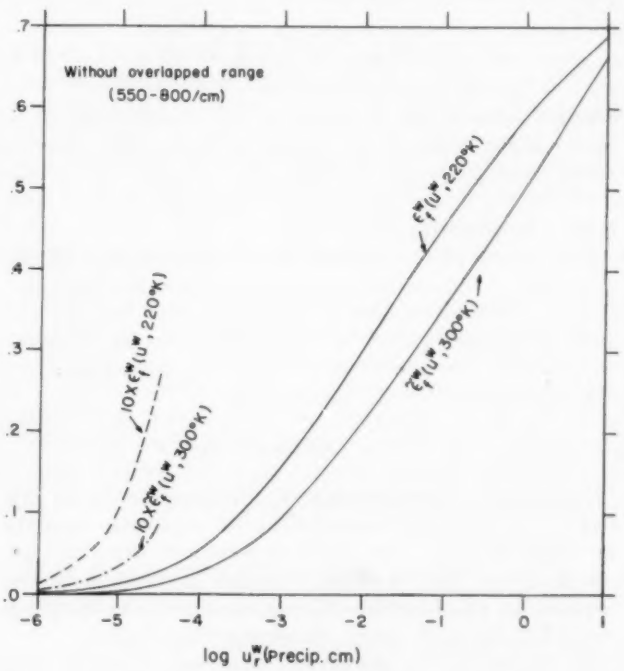

FIGURE 1.—The slab emissivity and the mean slab absorptivity of water vapor. The contribution of the frequency range overlapped with the 15 μ band of carbon dioxide (550–800/cm.) was not included.

[1] According to Benedict [4], the collision cross section of H_2O–N_2 collision is 6-7 times as large as that of N_2–N_2 collision instead of twice implied by equations (30) and (31). If so, reanalysis of the experiment by Howard et al. [27] seems to be desirable. Before this is done, we shall tentatively adopt their present results.

for various temperatures. Though his theoretical curve at normal temperature and 1 atmosphere pressure (NTP) does not exactly coincide with the experimental curve mentioned above [27], his results give us the approximate magnitude of the change of effective optical thickness corresponding to the change of temperature. By shifting horizontally the experimental curve mentioned above by the same distance [3] as the distances between the curve at 300° K. and that at other temperatures shown in figure 2 of Sasamori's paper, the final absorption curves were obtained for various temperatures which are shown in figure 2 and were used for our computation. Interpolation of these curves in this figure gives us the approximate absorptivity curve for any temperature above 218° K. and below 300° K. When the temperature is higher than 300° K. or lower than 218° K. we adopt the absorptivity of 300° K. and 218° K., respectively. In order to use these absorptivities, it is necessary to compute the effective temperature of the atmospheric layers. Although the mixing ratio of carbon dioxide is approximately constant with height, pressure as well as temperature vary with altitude. Therefore, the estimation of effective temperature involves cumbersome computations. (See, for example, Plass [51]). In view of the fact that the absorptivity of carbon dioxide at NTP is itself subject to some uncertainty, we adopted the following simplest possible approximation for the computation of effective temperature T_{eff}.

$$T_{eff}=\left(\int_{P_1}^{P_2} TdP\right)\Big/\left(\int_{P_1}^{P_2} dP\right) \tag{33}$$

where P_1 and P_2 are pressures of upper and lower limits of the layer, respectively. After obtaining this effective temperature, we can compute the absorptivity of the layer for T_{eff} by linearly interpolating absorptivities with respect to temperature.

This effect of temperature on the absorptivity of the 15μ band of carbon dioxide was included in the computation of the heat balance of the atmosphere but, for the sake of simplicity, not in the computation of radiative equilibrium. In the latter computation, we adopted the absorptivity at 218 °K. consistently.

OZONE

Laboratory measurements of the absorptivity of this band were made by Summerfield [60] and more recently by Walshaw [65]. The latter experiments were used for our purpose. In his paper, Walshaw presents empirical expressions which agree well with the observed absorption curve but are at the same time quite complicated.

In this study, for the sake of simplicity, his data were re-analyzed to get the absorptivity suitable for our system of computation. Re-analysis was confined to the runs a–i of Walshaw's experiment which cover the ordinary

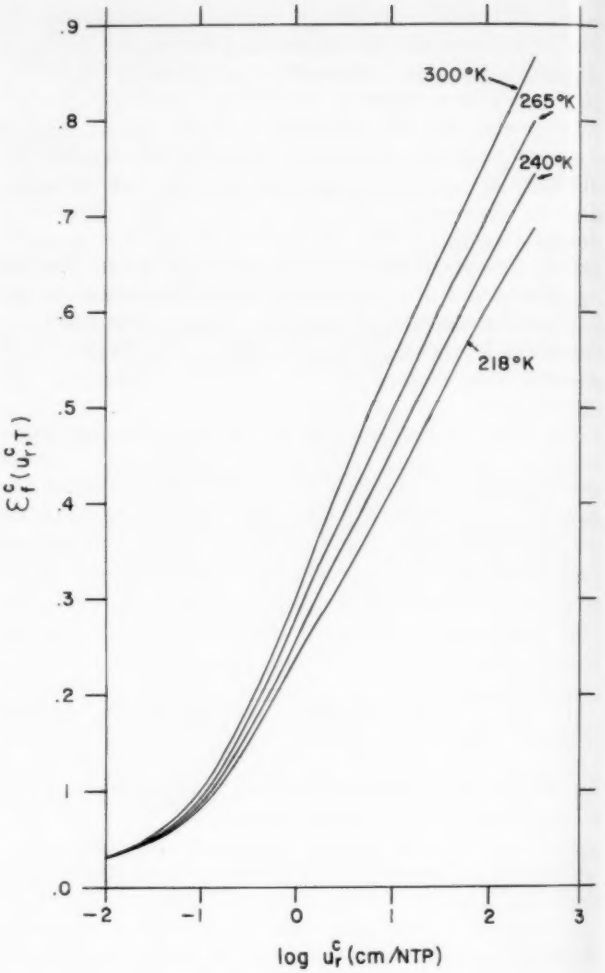

FIGURE 2.—The mean slab absorptivity of the 15 μ band of carbon dioxide for various temperatures. The absorptivity for 300° K. is based on the experiment by Howard et al. [27]. The temperature dependence of the absorptivity was estimated based upon the theoretical computation of Sasamori [55].

range of ozone amounts in the atmosphere. Based upon these runs, the value of κ was determined to be 0.3 by the least squares method.[4]

In figure 3, observed values of mean band absorptivity of a column were plotted versus effective optical thickness u_r which is defined by

$$u_r=[(P+.61p)/P_0]^{\cdot 3}\,u \tag{34}$$

The addition of $0.61p$ to the total pressure P, which appears in the numerator of this equation, was originally suggested by Walshaw [65]. Based upon his results of

[3] Of course, this distance depends upon the amount of CO_2 also.

[4] In order to perform the least squares method, absorptivity was tentatively assumed to be proportional to the square root of the amount of ozone.

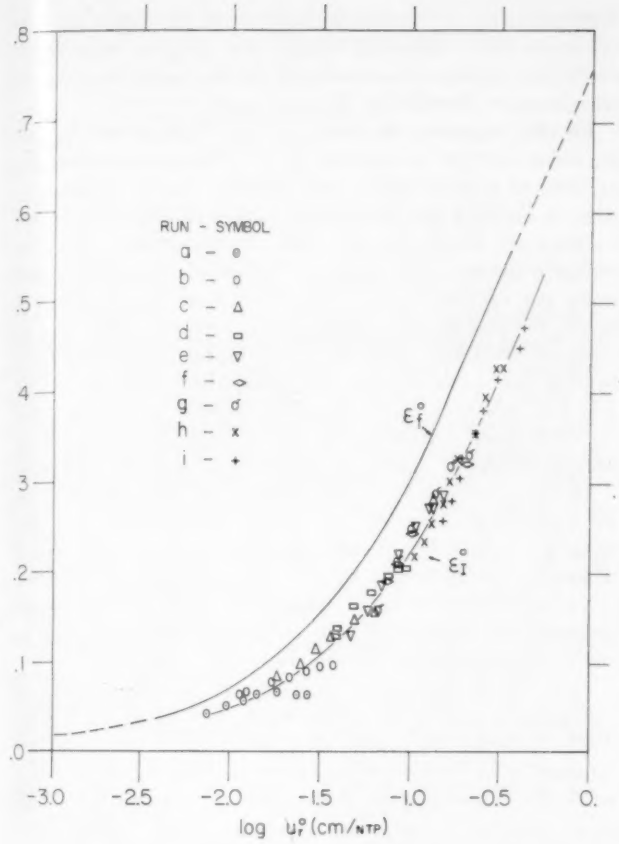

FIGURE 3.—The mean absorptivities of both column and slab of the 9.6 μ band of ozone (i.e., $\mathcal{E}_I^o$ and $\mathcal{E}_f^o$) obtained by processing the results of Walshaw's experiment [65]. The symbols adopted for plotting his measurement of mean absorptivity of column are the same as those adopted by himself for the series of runs of his experiment.

experiments, he concluded that the effective collision cross section of ozone is about 1.61 times as large as that of air. For the atmospheric condition, however, $P \gg p$, so this addition is not necessary.

The curve of best fit to these data gave us the mean band absorptivity of a column which was changed into the mean band absorptivity of a slab in the usual way. The slab absorptivity corresponding to the logarithm (base 10) of the various effective amounts of ozone (Unit: cm./NTP), which was used for our computation, is also shown in figure 3.

Examining the plotted values in figure 3 carefully, we notice that there is a rather large scattering of points for a small amount of effective ozone. (Refer to runs a, b.) Analyzing Walshaw's experiment for a small amount of ozone we notice the following tendency. As the pressure becomes larger, i.e. approaches 1 atmosphere pressure, absorptivity seems to become more or less independent of pressure. This small dependence is the cause of scattering of plotted points and suggests the inadequacy of equation (34) for incorporating the pressure dependence. However, as the pressure in or near the ozone layer, where the effect of this band is important, is much less than 1 atmosphere pressure, this tendency should not cause serious error in our computation.

5. ABSORPTION OF SOLAR RADIATION

WATER VAPOR

Based mainly upon Fowle's work [14], [15], [16], the absorptivity curve of solar radiation by water vapor has been constructed by Kimball [32], Mügge-Möller [42], Yamamoto-Onishi [69], Houghton [25], and McDonald [37]. For this work, in order to cover the small amount of water vapor, we constructed the absorption curve based mainly upon experiments by Howard et al. [27].

According to their paper [27], the water vapor absorption bands at 6.3, 3.2, 2.7, 1.87, 1.38, 1.1, and 0.94μ were studied individually for the absorber concentrations ranging from 0.001 to 3.8 cm. of precipitable water and for the various total pressures with nitrogen up to 740 mm. Hg. Using mainly these results, we obtained the absorption of solar radiation by water vapor. Although Howard et al. did not give the absorption for the amount of precipitable water which is more than 3 cm., they determined the parameter of Goody's random model by use of their experimental results and predicted the magnitude of band absorption for 3, 10, and 50 cm. of precipitable water. Therefore, we can compute the absorption up to 50 cm. of precipitable water. For the absorption by a very small amount of precipitable water which was not covered by their experiments, we simply used the experimental equation for weak fit proposed by Howard et al. [27].

The absorption bands at 0.75 and 0.85μ were not covered by their experiment because of the minor importance of these bands. In view of the fact that the intensity of near infrared solar spectrum increases with decreasing wavelength, the contributions of these two bands are not negligible when the amount of precipitable water is more than 1 cm. Although the absorption band at 0.94μ was covered by their experiment, parameters of

TABLE 3.—*The values of κ for various absorption bands of water vapor which absorb solar radiation (after Howard et al. [27]).*

Characteristic wavelength (μ)	κ Weak fit	κ Strong fit
6.3	0.60	0.72
3.2	.60	----
2.7	.64	.61
1.87	.60	.62
1.38	.60	.43
1.1	.52	----
0.94	.54	----

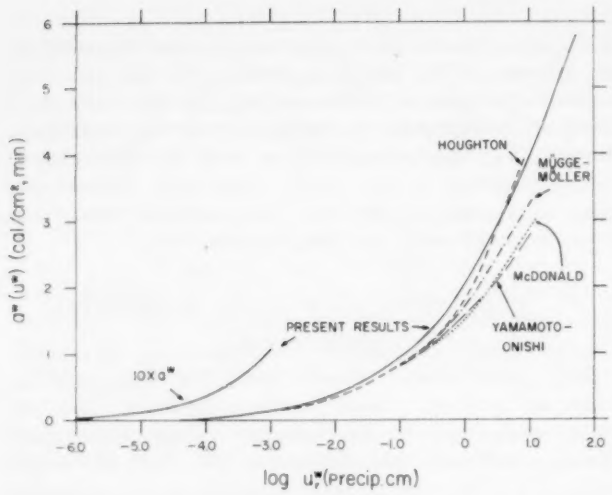

FIGURE 4.—Comparison of the absorption of solar radiation by water vapor by various authors.

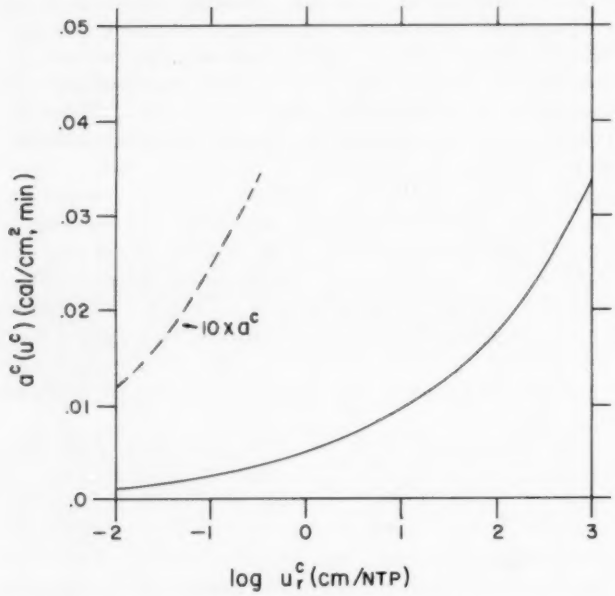

FIGURE 5.—The amount of the absorption of solar radiation by carbon dioxide based upon the results of experiment by Howard et al. [27].

Goody's model were not given, due probably to the poor accuracy of the laboratory experiment for this band. Therefore, their result cannot be extrapolated to the amount of water vapor which is larger than a few cm. of precipitable water.

In order to compute these three weak bands which are of rather minor importance, we used Fowle's data. Extrapolation of his absorption curve to larger optical thickness was done by using the general absorption coefficient of Yamamoto and Onishi [67] [5] and the general transmission function of Elsasser band.

Finally, summing the contributions from these 9 bands, we computed the absorption of solar radiation versus the amount of precipitable water, which is shown in figure 4. Also in figure 4 the absorption curves obtained by other authors are shown for the sake of comparison. On the ordinate the rate of absorption is given in units of cal./cm.^{2} min., and on the abscissa logarithm (base 10) of water is given in units of cm. of precipitable water. In order to compare our result with that of McDonald, it is necessary to add the contributions from the absorption bands at 2.7, 3.2, and 6.3μ to McDonald's curve. If we do that, the difference between our curve and McDonald's or Mügge-Möller's curve is approximately 10 percent.

In spite of the fact that Houghton [25] found some inconsistencies between the Fowle publications and the data published by Smithsonian co-workers, the band absorptivities obtained by Fowle and those by Howard et al. coincide with each other well,[6] and the difference between our curve and Mügge-Möller's does not seem to cause a serious effect, whichever result is correct.

In order to incorporate the pressure effect properly, it is necessary to find the proper value of κ for those bands. Table 3 shows the values of κ which were obtained by Howard et al. [27] experimentally for both the strong and weak fit. Referring to this table, we assume the value of κ common for all those bands to be 0.6. This value is the same as the κ-value adopted for the terrestrial radiation of water vapor.

CARBON DIOXIDE

Extensive experiments by Howard, Burch, and Williams [27] are available for the computation of the amount of absorption of solar radiation by carbon dioxide. They studied the carbon dioxide absorption bands at 5.2, 4.8, 4.3, 2.7, 2.0, 1.6, and 1.4 μ individually for absorber concentration ranging from 1 to at least 1000 atmo-cm., for various total pressures including nitrogen up to 740 mm. Hg.

Based upon their results and the solar irradiant spectrum outside the earth's atmosphere which is given in the Smithsonian Meteorological Tables, the resultant absorption curve can be constructed by summing the contribution of the 7 bands mentioned above. Figure 5 gives this relation between the absorption of solar radiation (cal./cm.^{2} min.) versus the logarithm (base 10) of the amount of carbon dioxide (cm./NTP).

In order to take into consideration the effect of pressure

[5] Though their general absorption coefficients were based upon Fowle's data and rather crude theoretical computations, some adjustment of the coefficients was needed to make the resultant absorption curves coincide with Fowle's.

[6] There is some significant difference in the absorptivities of the 1.38μ band. Howard's absorptivity is larger than Fowle's.

TABLE 4.—*κ-values for various CO_2 bands which absorb solar radiation. $(\overline{A_\nu})$crit. is the upper limit of the mean band-absorptivity for which the equation of weak fit is applicable.*

Characteristic wavelength (μ)	κ Weak fit	κ Strong fit	$(\overline{A_\nu})$crit.
5.2	0.80	----------	0.273
4.8	.74	----------	.333
4.3	----------	.93	.147
2.7	.86	.88	.156
2.0	.78	.83	.178
1.6	.76	----------	.145
1.4	.82	----------	.133

broadening, it is necessary to know the magnitude of κ. Table 4 gives the values of these 7 absorption bands obtained by Howard, Burch, and Williams for both the strong and the weak fit. The value of κ for the weak fit concentrates around 0.8 and that for the strong fit concentrates around 0.9. Therefore, we assume the value to be 0.86 which is the same as the one used for the computation of long wave radiation of the 15μ band of carbon dioxide.

OZONE

In order to compute the amount of solar radiation absorbed by ozone, it is first necessary to know the ultraviolet portion of the solar spectrum irradiance curve outside the earth's atmosphere. Recent work of Johnson [30] is available for this purpose. He constructed the improved version of the solar irradiance curve outside the atmosphere using recent results of the observations obtained by high altitude rocket as well as the Smithsonian observations.

Another bit of information needed for the construction of the absorption curve is the absorptivity of ozone with respect to various wavelengths. The most recent data about which the authors know are the results of experiments by Vigroux [64] and by Inn and Tanaka [28]. In spite of the distinct differences in the experimental methods, the agreement between them is fairly good.

In this paper, following the recommendation by Inn and Tanaka [29], we used Vigroux's experiment for the computation of the absorption due to Huggins band (3000–3700 Å.) and the experiment by Inn and Tanaka for the computation of the absorption due to the Hartley (2000–3000 Å.) and Chappuis bands (4400–7600 Å.). In view of the temperature of the stratosphere where the absorption due to ozone mainly takes place, we adopted the absorption coefficients for the temperature of −40° C. The values could be calculated from the estimate of Vigroux who observed the ozone absorption over the −92° C. to 120° C. temperature range. In figure 6 continuous lines show the total amount of absorption due to ozone (cal./cm.^{2} min.), that due to the Hartley and Huggins bands, and that due to Chappuis band versus the logarithm of the amount of ozone (cm./NTP). For the sake of comparison, the absorption curve which is obtained by integrating the diagram constructed by

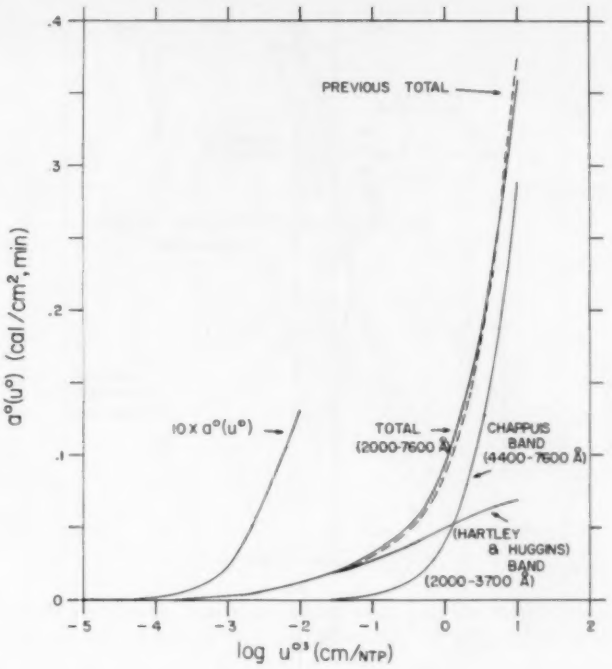

FIGURE 6.—The amount of the absorption of solar radiation by ozone based upon the results of experiments by Vigroux [64], and Inn and Tanaka [28]. The contribution of each band is also shown in the figure.

Craig [8] and extended by Pressman [52] is also shown in figure 6 as a dashed curve. In spite of the fact that the latter curve is based upon the older experiment by Ny and Choong [46, 47], and upon different solar irradiant curves, the coincidence between these two absorption curves is good.

6. DISTRIBUTION OF GASES

WATER VAPOR

The vertical and latitudinal distributions of water vapor in the atmosphere were compiled by Telegadas and London [61] and London [36], based upon surface and radiosonde observations. We adopted their distributions of the relative humidity in the lower half of the troposphere where the temperature is above —30° C. and the measurements of relative humidity by radiosonde are accurate enough. In the upper half of the troposphere where the temperature is below —30° C. we adopted the constant frost point lapse rate of —6.25°C./km. which coincides with the results of many observations from an airplane conducted by the British group [43], [63].

Concerning the moisture distribution at the higher altitude Barclay et al. [2] constructed a convenient figure which shows the results of various authors in compact form and is reproduced in figure 7. Among them, Bar-

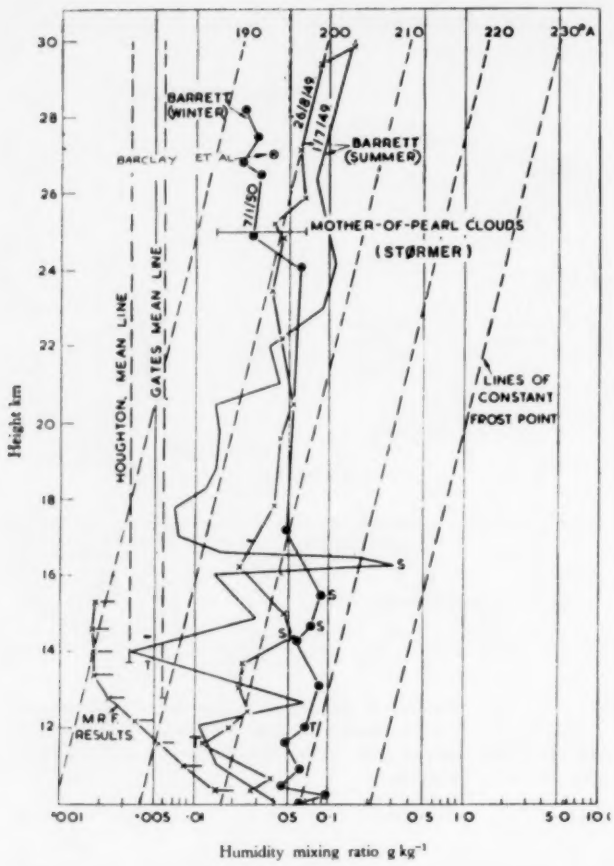

FIGURE 7.—The vertical distributions of water vapor obtained by various authors and compiled by Barclay et al. [2]. The data for mother-of-pearl clouds are from Størmer [59].

rett's [3] results seem to be too large, due probably to the evaporation from the balloon. Therefore, based upon the measurements by Murgatroyd et al. [43] and the infrared measurements by Houghton et al. [26] and Gates et al. [17], we tentatively assumed the constant frost point of 190°K. in the stratosphere up to the height of about 30 km. (9-mb. level) and assumed a constant mixing ratio above this level. This gives the total amount of moisture which is consistent with infrared measurement. The final results of the vertical distribution of moisture which were obtained by the British group, and summarized by Tucker [63], are given in figure 8a. It is very interesting that the frost point decreases with height and approaches the value of about 190°K. irrespective of season. Recently Murgatroyd[7] obtained his results of the measurements of vertical distribution of water vapor at various latitudes which are also reproduced in figure 8b. According to these results the frost point seems to approach almost the same value, i.e. 190°K., irrespective of latitude. In view of these results our assumption that the frost point is constant in the stratosphere irrespective of season and latitude seems to be reasonable.

In figure 9 the latitudinal and vertical distributions of the mixing ratio (gr./kg. of air) of water vapor for all seasons, which we adopted for our computations, are shown.

CARBON DIOXIDE

It is generally considered that the proportion of carbon dioxide is relatively invariant below 90 km. According to the table presented on page 8–1 of [18] the amount of carbon dioxide is approximately 0.03 percent by volume or 0.0456 percent by weight. The reduced thicknesses of carbon dioxide at normal temperature and normal pressure were computed from these data.

OZONE

The seasonal and latitudinal distribution of ozone was first given by Götz [21] in the form of a diagram. Based upon the more recent measurement of higher sensitivity, Normand [45] improved the diagram by removing the Arctic winter gap which exists in the original case. Normand's diagram must be modified further because the amount of ozone in his diagram was computed by use of the absorptivity of Ny and Choong [46], [47], which is about 36 percent larger than that of Vigroux at the wavelength adopted for this computation. The latitudinal distributions of the total amount of ozone for all seasons are shown in figure 10 in the Vigroux scale.

Concerning the vertical distribution of ozone, Tønsberg and Olsen [62] found a good correspondence between the total amount of ozone and vertical distribution. Figure 11 shows this correspondence in the Vigroux scale.

From figure 10 and figure 11 it is possible to obtain the distribution of ozone with respect to latitude, season, and height which we used for our computation.

7. COMPUTATION OF RADIATIVE EQUILIBRIUM

So far we have constructed a scheme for the computation of radiative temperature change, deduced the absorptivities from various theoretical and experimental results, and determined the distribution of various atmospheric gases consistent with the observations obtained by various authors. Now we are in a position to compute the seasonal and latitudinal distributions of the radiative equilibrium temperature as well as that of heat balance.

The basic principle of the method of computation is to approach the state of radiative equilibrium asymptotically from certain initial conditions. If we express temperature as a function of height and time, i.e., $T(z,t)$, equilibrium temperature might be expressed by $T(z,\infty)$. Since it is

[7] Private communication. See reference [44].

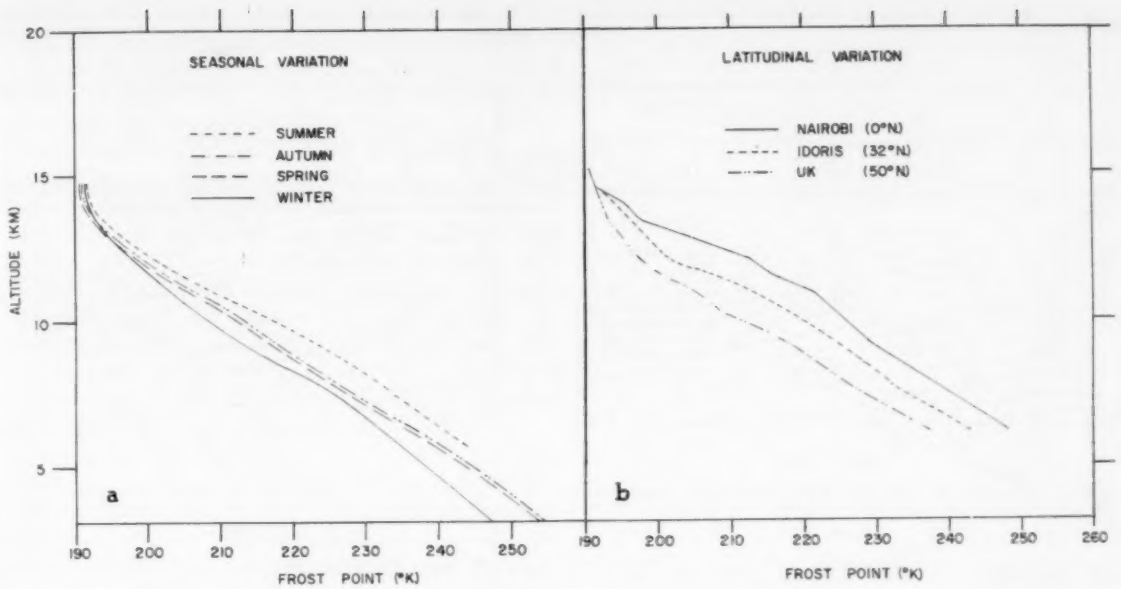

FIGURE 8.—(a) Seasonal variations of the vertical distribution of water vapor which were measured from an airplane by the British group [43] and compiled by Tucker [63]. (b) The vertical distribution of water vapor at various latitudes obtained by Murgatroyd (private communication).

possible to determine the rate of temperature change uniquely from the distributions of temperature and gases, and since the continuous variation of temperature distribution causes continuous variation of the rate of temperature change, there exist such δ and t_c as to satisfy the following condition for any value of $\mathcal{E}$:

$$\mathcal{E} > \text{Max} \mid T(z,\infty) - T(z,t_c) \mid \tag{35}$$

and

$$\delta > \text{Max} \left| \left(\frac{\partial T(z,t_c)}{\partial t} \right)_{\text{RAD}} \right| \tag{36}$$

where

$$T(z,t_c) = T(z,0) + \int_0^{t_c} \left(\frac{\partial T(z,t_c)}{\partial t} \right)_{\text{RAD}} dt \tag{37}$$

and

$$\left(\frac{\partial T(z,t)}{\partial t} \right)_{RAD} = \left(\frac{\partial T(z,t)}{\partial t} \right)_{LR} + \left(\frac{\partial T(z,t)}{\partial t} \right)_{SR}. \tag{38}$$

In other words, we can approach the radiative equilibrium as closely as we want by properly choosing the magnitude of δ.

In order to perform the integration of equation (37) by a finite difference scheme, we adopted the forward time difference, i.e.

$$T(z,t+\Delta t) = T(z,t) + \left(\frac{\partial T(z,t)}{\partial t} \right)_{RAD} \Delta t \tag{39}$$

Brunt [5] shows that the equation of temperature change due to atmospheric radiation could be crudely approximated by an equation of heat diffusion. According to Richtmyer [53], the finite difference time integration of a diffusion equation can be performed stably by adopting forward time differencing and choosing the proper time interval. Based upon this information, we used forward time differencing for our integration. The optimum time interval which satisfies the condition of computational stability was determined by a trial and error method. For our grid system (refer to Appendix I) the integration was stable for time intervals shorter than 12 hours but was unstable if we adopted a 24-hour interval. We adopted an 8-hour interval throughout our computations of radiative equilibrium.

The lower and upper computational boundary conditions are

$$T(0,t) = T_s = \text{const.} \tag{40}$$

at the ground surface, and

$$\partial T / \partial p = 0 \tag{41}$$

at the top of the atmosphere. (Refer to equation A–3 in the Appendix III for exact meaning of latter condition).

The initial condition which we adopted for the computation of radiative equilibrium was an isothermal atmosphere with the observed temperature of the earth's surface. Since we adopted a finite value of δ, the final equilibrium temperature has an uncertainty of the order

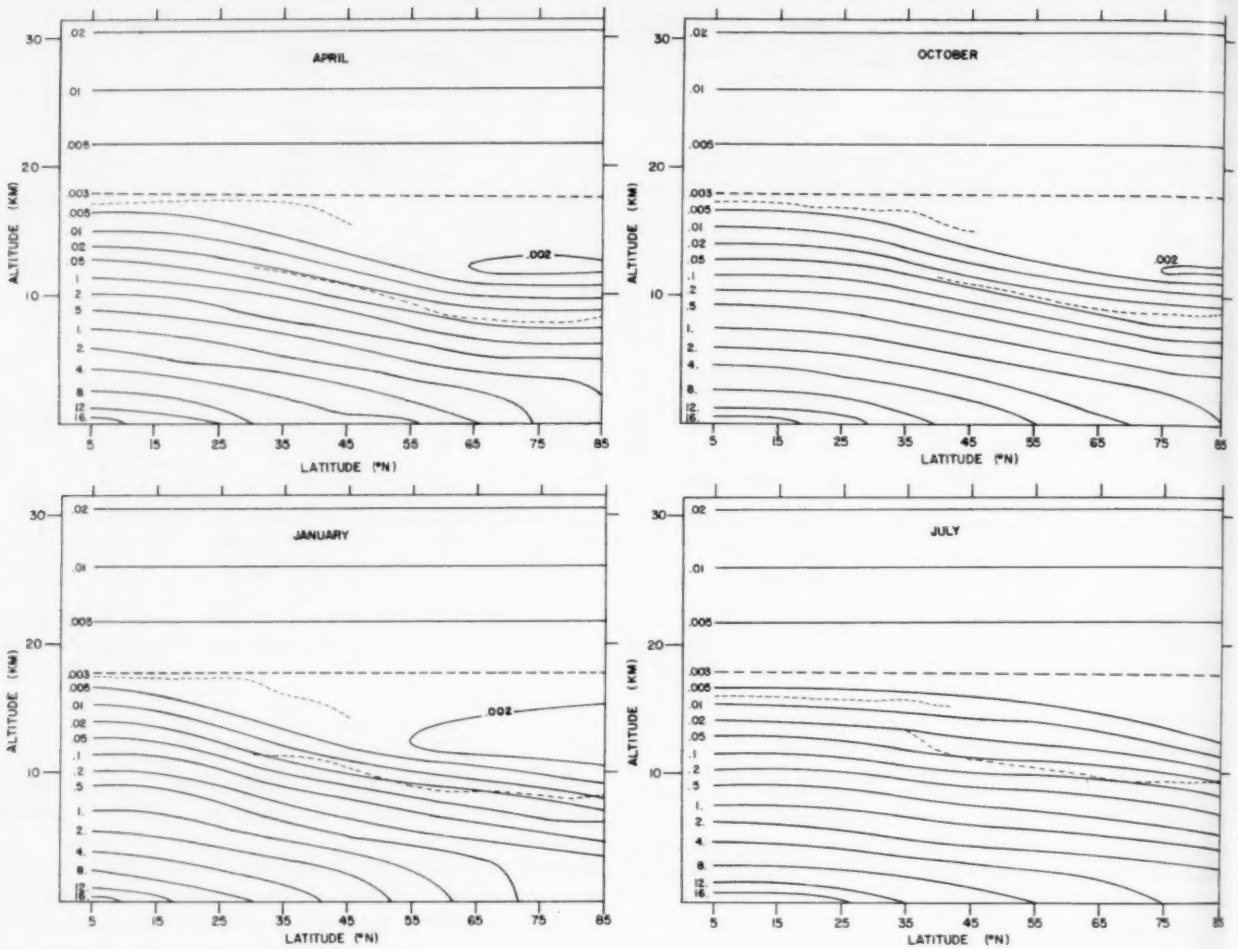

FIGURE 9.—Seasonal and latidudinal distribution of water vapor (g./kg. of air) adopted for our computation. The thin dashed lines show the height of the tropopause determined by Kochanski [34].

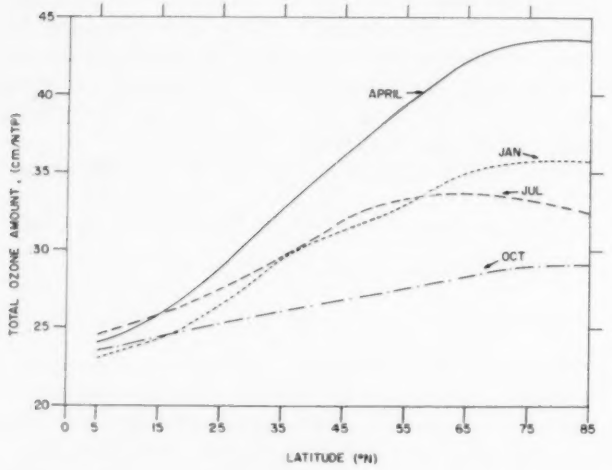

FIGURE 10.—Seasonal and latitudinal distributions of the total amount of ozone compiled originally by Götz [21] and modified later by Normand [45].

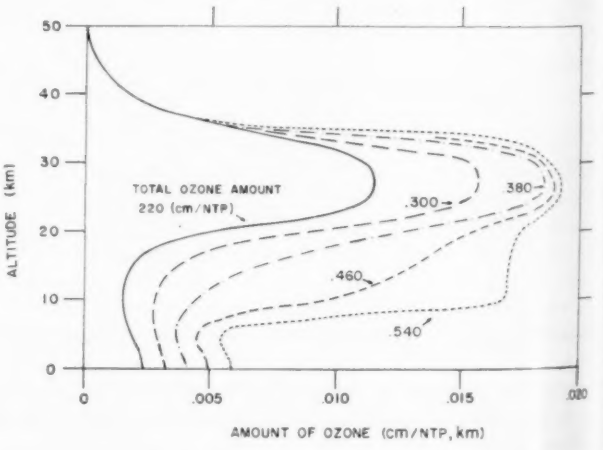

FIGURE 11.—Vertical distributions of ozone corresponding to the various total amounts in the Vigroux scale obtained by Tønsberg and Olsen [62].

of magnitude of $\mathcal{E}$, depending upon the initial conditions chosen. Therefore, in order to compare our results with each other it is desirable to start from the same initial conditions, which we did. For our computations we adopted values of δ ranging from 0.03°C./day to 0.07°C./day. According to our estimate by extrapolation, the maximum difference between the actual and the computed equilibrium temperatures appears around the tropopause when we adopted the isothermal initial condition and varies[8] from 3°C.–7°C. corresponding to the range of δ given above. The time for reaching this quasi-equilibrium state depends upon the amount of sunshine and the magnitude of δ. When we adopt 0.07°C./day for δ, this time ranges from 200 to 500 days, depending upon the amount of sunshine. The weaker the sunshine, the longer it takes to reach this quasi-equilibrium.

Along with the computation of the equilibrium temperature by this initial value method reported in this paper, we also computed it as the solution of a homogeneous set of equations whose unknowns are the temperatures at various levels. The preliminary results obtained by adopting this matrix method are to be published [41]. Using this matrix method, we can get the vertical distribution of equilibrium temperature immediately and are free of the uncertainty, $\mathcal{E}$, that we have in the initial value method. Therefore, the results obtained by this matrix method serve as an independent check of the present initial value method. In order to adopt this linear matrix method, however, it is necessary to linearize the equation of temperature change with respect to temperature. Whereas for the initial value method it does not matter whether the equation is linear or non-linear with respect to temperature. In this respect the present initial value method is much more flexible and more accurate than the matrix method. The initial value method might be regarded as one of the methods for solving the set of non-linear equations by successive approximation.

8. DISCUSSION OF RESULTS

RADIATIVE EQUILIBRIUM

An Example of Radiative Equilibrium.—Figure 12 shows one example of the temperature distribution at radiative equilibrium. The distribution of gases and the solar radiation at 35°N. in April were adopted for this computation. The temperature of the earth's surface was assumed to be 289°K. As a reference, the vertical temperature distribution of the standard atmosphere and that of the dry adiabatic atmosphere are also given in the same figure. According to this figure, the lapse rate of the radiative equilibrium atmosphere is more or less dry-adiabatic up to the 11-km. level except near the ground surface where there is an abrupt decrease of temperature with height. The height of the tropopause is about 11 km. This

[8] The computed equilibrium temperature is warmer than actual.

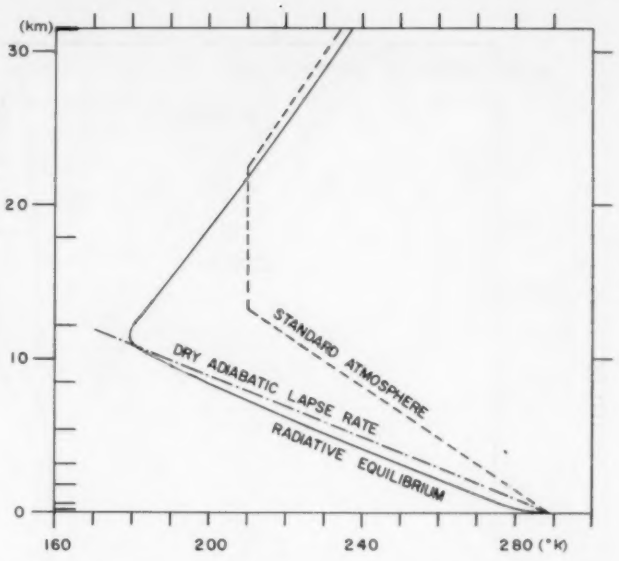

FIGURE 12.—Distribution of radiative equilibrium temperature. The amount of sunshine, the distributions of gases, and surface temperature at 35° N. in April were used (δ=0.03° C./day). The line of standard atmosphere and that of dry adiabatic lapse rate are also shown for the sake of comparison.

approximately coincides with the observed height of the tropopause in middle latitudes but is much lower than that of the equatorial tropopause. We shall discuss this subject in detail later. The computed tropopause temperature is approximately 180°K., which is about 20°–40°K. lower than the observed temperature. Since the frost point of water vapor was assumed to be 190°K in the lower stratosphere, this computed temperature would cause supersaturation around the tropopause It is reasonable that the radiative equilibrium temperature of the upper troposphere and lower stratosphere is much lower than the temperature of the standard atmosphere because of the neglect of the process of condensation and that of upward eddy transport of energy from the earth's surface. Above this level the temperature increases sharply with height and again approaches the temperature of the standard atmosphere.

In figure 13 the vertical distribution of various radiative heat balance components corresponding to the quasi-equilibrium temperature of figure 12 is shown. The rapid increase of heating with height due to the absorption of solar ultraviolet radiation by ozone is the main reason for the tendency of temperature increase with height in the stratosphere. This tendency was also obtained by Gowan [22, 23] by taking into consideration the absorption of solar radiation by ozone. If we compare his results with ours, we notice that his radiative equilibrium temperature is much higher than ours. This might be partly due to the fact that he adopted the black-

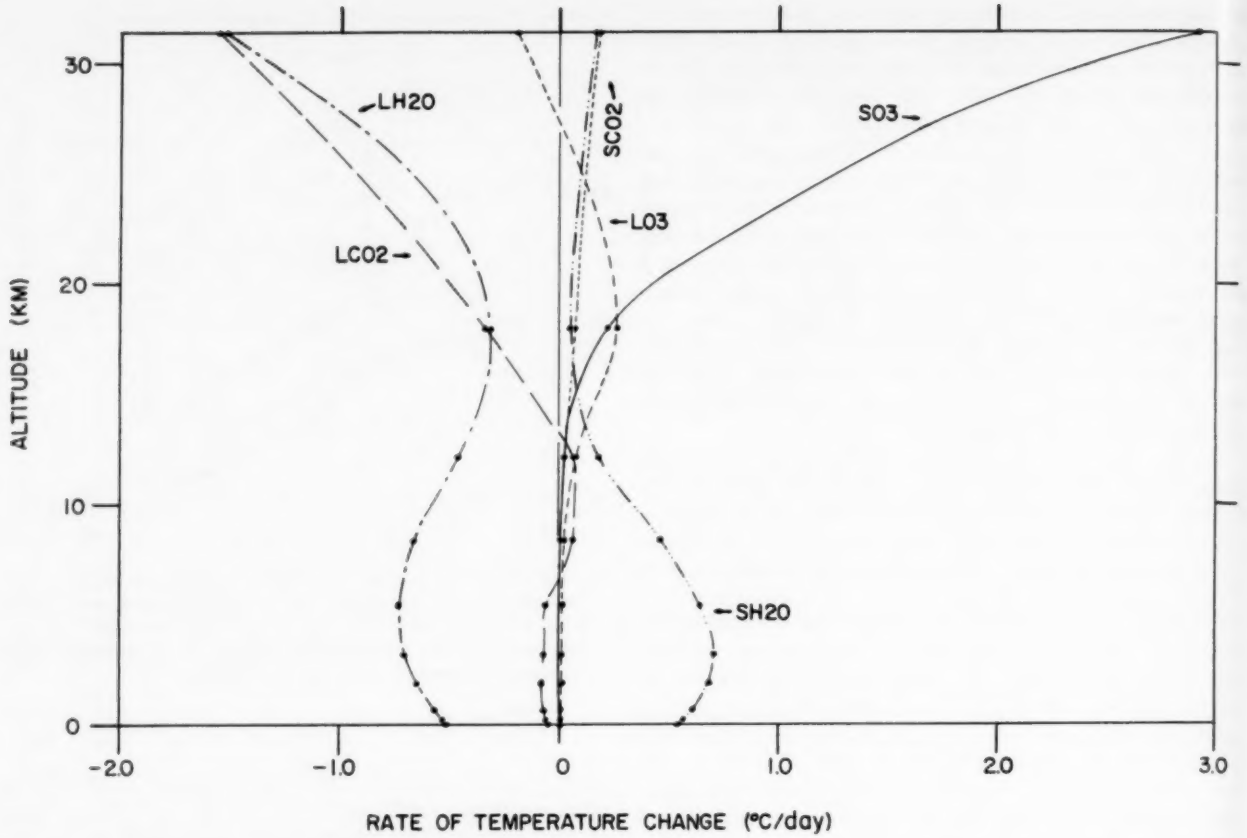

FIGURE 13.—Vertical distribution of the various heat balance components corresponding to the radiative quasi-equilibrium shown in figure 12. SH20, SC02, and S03 are the rates of temperature change due to the absorption of solar radiation by water vapor, carbon dioxide, and ozone, respectively; and LH2O, LCO2, and LO3 are those due to the long wave radiation by water vapor, carbon dioxide, and ozone, respectively.

body radiation at 6000°K. as the solar extraterrestrial radiation. It is now well known that this value of extraterrestrial radiation is much larger than the observed value in the ultraviolet spectrum.

Here we should mention our results obtained by the matrix method, which are to be published in a separate paper [41].[9] In that paper, instead of assuming the temperature of the earth's surface, we computed it from the condition of radiative equilibrium. The computed temperature of the earth's surface is about 313°K. and is much warmer than the observed value. This is because of the neglect of energy transport from the ground to the atmosphere by turbulent eddies. As a result of this warm surface temperature, the lapse rate of the lower troposphere is somewhat steeper than that of the present computation. However, the height of the tropopause is approximately 11 km. and coincides with the present result. By comparison, Emden's tropopause is located much lower, somewhere around the 6–8-km. level. In the

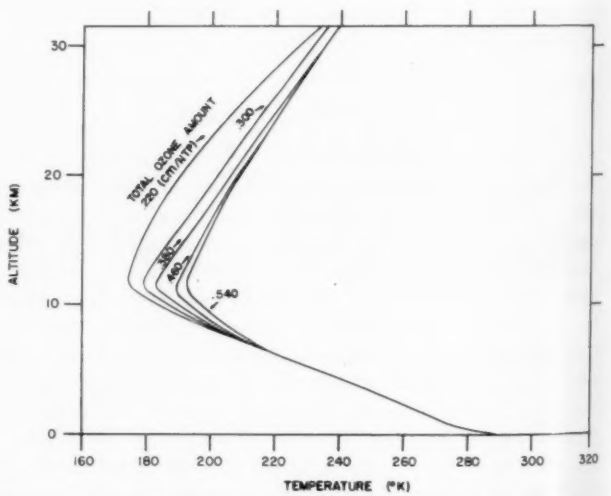

FIGURE 14.—Dependence of equilibrium temperature on the total amount of ozone. The amount of sunshine, distribution of water vapor, and surface temperature at 35° N. in April were used ($\delta = 0.03°$ C./day).

[9] Refer to the end of section 7.

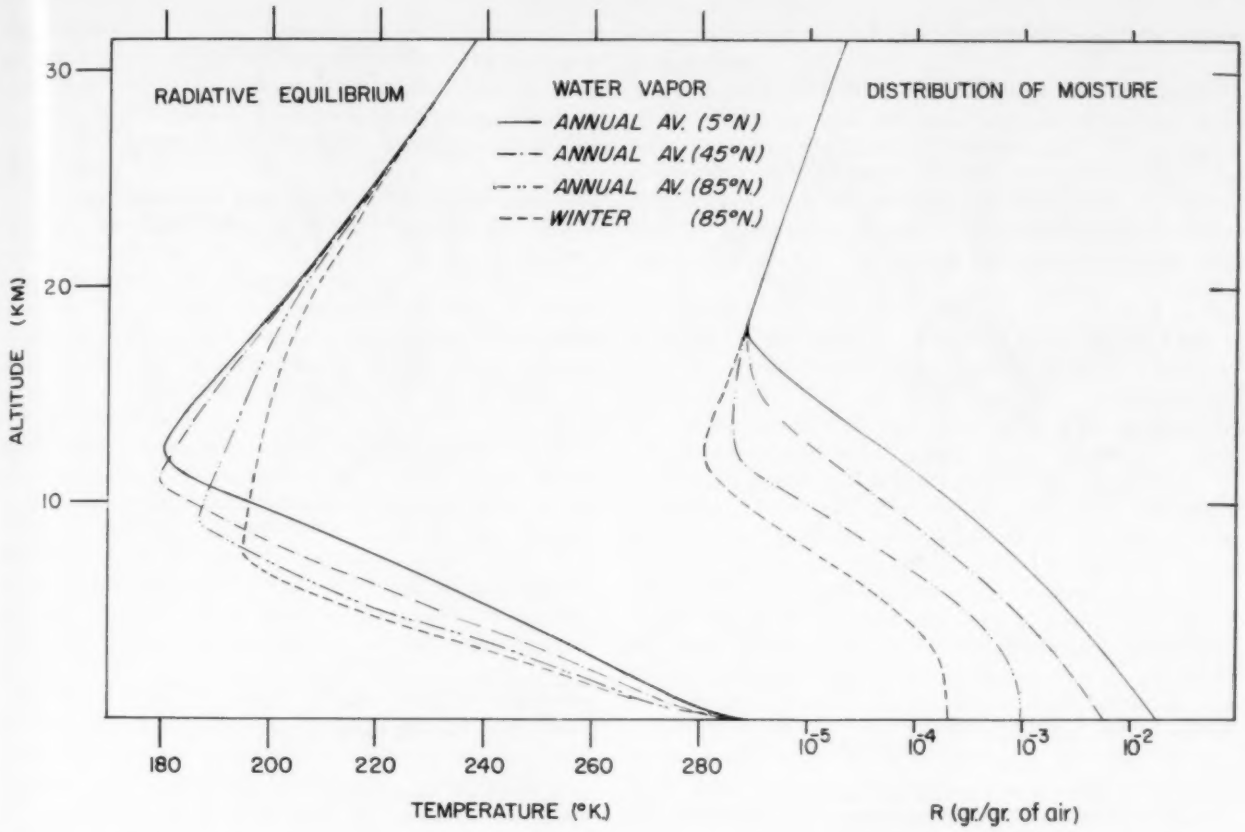

FIGURE 15.—Dependence of equilibrium temperature on the distribution of tropospheric moisture. The distributions of water vapor corresponding to each equilibrium temperature are shown on the right side. The amount of sunshine, distribution of ozone, and surface temperature at 35° N. in April were used ($\delta = 0.03°$ C./day) consistently.

computation by the matrix method, we allowed the possibility of a temperature discontinuity at the earth's surface as was first obtained by Emden [12], whereas in the present computation we did not. The magnitude of temperature discontinuity was very small, about 0.06°C. This is much smaller than the discontinuity of about 20°C. which Emden obtained in his computation of radiative equilibrium based upon the assumption of gray radiation. Accordingly, no large error would be introduced by the neglect of this temperature jump at the earth's surface, which we did in the present computation.

Radiative equilibrium and the distribution of gases.—In order to determine the influence of ozone on the radiative equilibrium, the distributions of radiative equilibrium temperature were computed for various total amounts of ozone, i.e., 0.220, 0.300, 0.380, 0.460, and 0.540 cm./NTP. This range of values includes almost all of the total amounts observed in various latitudes and seasons. The vertical distributions of ozone corresponding to these total amounts are given in figure 11. (Refer to section 6.) The amounts of gases other than ozone and the amount of sunshine are the average values at 35 °N. in April. Figure 14 shows the computed equilibrium temperatures. First of all, we note that the greater the ozone amount, the warmer the radiative equilibrium temperature around the tropopause. The variation of the equilibrium temperature around the tropopause is as much as 20°K. for the range of total ozone amount mentioned above. These results are understandable because, when the total amount of ozone varies, the vertical distribution of ozone varies most markedly around the tropopause (refer to fig. 11). This result suggests that ozone could be one of the important factors causing the increase of stratospheric temperature with latitude. However, as Goody [20] pointed out, the temperature of the earth's surface, which decreases with increasing latitude, is also an important factor in determining the heating due to the 9.6μ band of ozone. This problem will be discussed again by referring to the results of the computation of the heat budget, described in the latter half of this section.

Next, in order to investigate the influence of tropospheric water vapor on the radiative equilibrium tempera-

616949—61——3

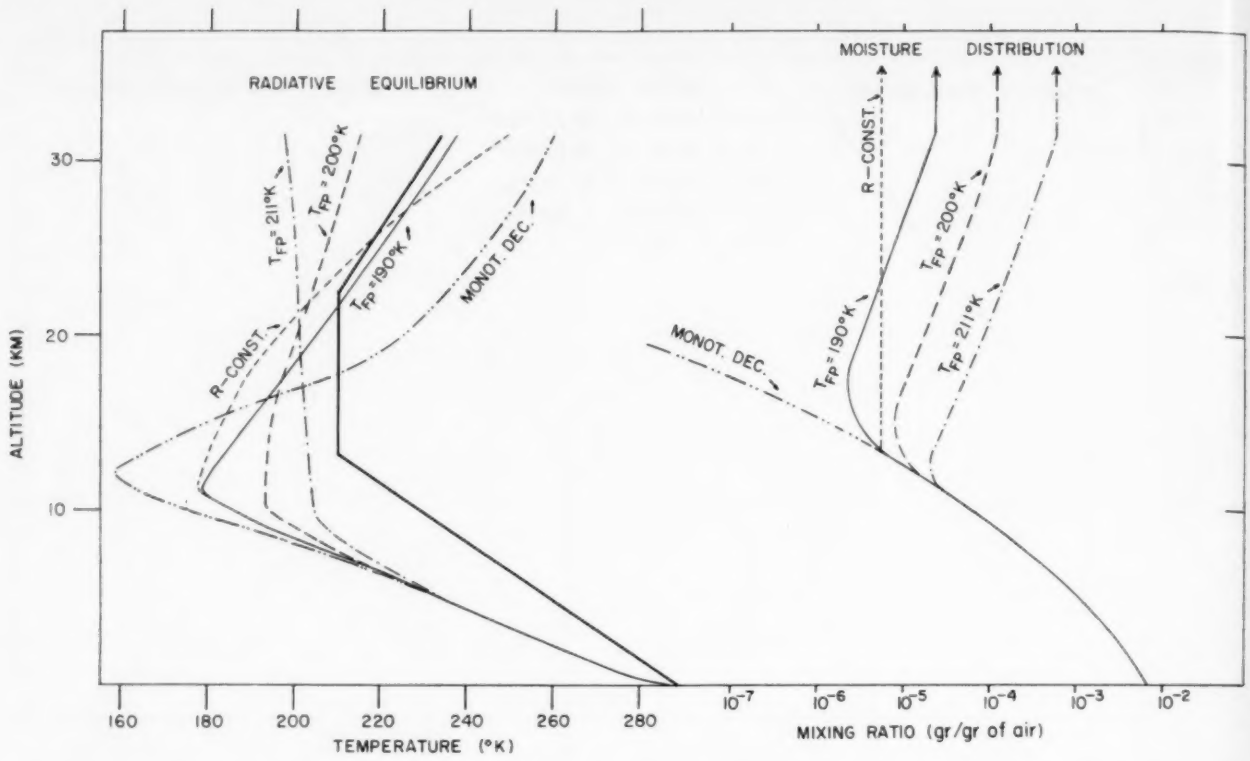

FIGURE 16.—Dependence of equilibrium temperature on the distribution of stratospheric moisture. The distributions of water vapor corresponding to each equilibrium temperature distribution are shown on the right side. The amount of sunshine, distribution of ozone, and surface temperature at 35° N. in April were used ($\delta = 0.03°$ C./day).

ture, equilibrium computations were made for various distributions of tropospheric water vapor. The distributions adopted for these computations are shown on the right hand side of figure 15. They are the annual means of water vapor at 5° N., 45° N., and 85° N., and the distribution at 85° N. in winter. The frost point of water vapor was always assumed to approach the constant value of 190° K. (−83° C.) in the stratosphere. The duration of sunshine, the solar zenith angle, and the distributions of various gases other than water vapor are the mean values at 35° N. in April and are kept the same throughout these computations. The resultant equilibrium temperatures are given on the left hand side of figure 15. The computed height of the tropopause for the low latitude distribution of moisture is higher than that in the high latitudes. The variation of the height of the tropopause over the range of tropospheric water vapor is about 5 km., which is about half of the observed difference in tropopause height between the Pole and the Equator as shown on the left hand side of figure 19. However, these results suggest that the distribution of moisture in the troposphere could be one of the important factors in determining the height of the tropopause. In order to understand these results, it is necessary to examine figure 13. As shown in this figure, the long wave radiation by water vapor is the most important cooling factor near the level of the tropopause. Accordingly, the more water vapor present, the stronger the cooling is. On the other hand, the heating effect due to the absorption of solar radiation by ozone markedly increases with altitude in the stratosphere and that due to the 9.6μ band of ozone also increases with altitude near the tropopause. Since there is usually more water vapor around the tropopause in low latitudes than in high latitudes, the level where the temperature starts increasing with increasing altitude owing to the heating effect of ozone, is higher in low latitudes than in high latitudes.

The importance of the distribution of water vapor as a factor determining the height of tropopause was emphasized by Goody [20] and Yamamoto [70]. Goody explained the latitudinal variation of the height of the tropopause by discussing the balance between the cooling effect of water vapor and the heating effect of the 15μ band of carbon dioxide. We shall discuss this theory in the latter half of this section. Yamamoto computed the temperature distribution of radiative equilibrium for the range of the latitudinal variation of tropospheric moisture

and obtained the correct magnitude of the pole-to-equator difference in the height of the tropopause. His computation, however, is based upon the assumption of gray radiation which gives us much too small absorptivity for the small amount of water vapor existing around the tropopause.

The most uncertain quantity involved in our computations is the distribution of water vapor in the stratosphere, which we discussed in section 6. Therefore, before discussing the computation of latitudinal and seasonal distributions of radiative equilibrium, it seems necessary to know more quantitatively the influence of stratospheric water vapor on the radiative equilibrium temperature profile. On the right hand side of figure 16 the distributions of moisture adopted for this series of computations are given. In order to cover the range of values observed by various authors (refer to fig. 8) we made equilibrium computations for constant frost points of 190 °K.,200 °K., and 211 °K.[10] in the lower stratosphere. Also the radiative equilibrium for a stratosphere with constant mixing ratio [11] and one with a monotonical decrease of frost point (6.25°K./km.) were computed. The distributions of tropospheric water vapor and of other gases are the mean values at 35° N. in April.

On the left side of figure 16 the results of the computations are shown, from which we note that the more water vapor which exists in the upper stratosphere, the lower becomes the temperature of the upper stratosphere and the higher the temperature near the tropopause. This is because abundant moisture in the top layer causes strong emission into outer space, and thus the top layer cools more strongly. On the other hand, this moisture increases the downward long wave radiation by water vapor from the top layer, so that the lower layer can be heated more strongly by this radiation. The large difference in the equilibrium temperature of the upper layer of the atmosphere due to the variation of the stratospheric moisture suggests the importance of the continuous and extensive observations of the amount of water vapor. When the amount of water vapor is small, it is difficult to estimate the absorptivity. However, as far as the present results are concerned, the frost point of 190° K., which we are going to adopt consistently in the following computation, seems to give us reasonable temperatures at the highest altitudes involved in our computation.

The series of computations carried out so far suggests that the factor of primary importance in determining the height of tropopause is the distribution of tropospheric moisture. The distribution of ozone and that of water vapor in the stratosphere, however, seem to have an important effect on the temperature around the tropopause. Therefore, indirectly, they could also affect the height of the tropopause by causing a change in the dynamical behavior of the stratosphere and the upper troposphere.

Seasonal and latitudinal distribution of radiative equilibrium.—Next we shall compute the latitudinal and seasonal variations of equilibrium temperature. The amount of sunshine and the distribution of gases adopted for this computation were described in sections 3 and 6, respectively. Mean observed values for each season and latitude were adopted for the surface temperature, which was assumed to be constant with time. In order to cut the amount of computation, 0.07° C./day was adopted as the convergence criterion δ. This value is slightly larger than the one we have used so far (0.03° C./day). According to our pilot test, the small increase of δ changes the general features of the results very little, if we consistently start from an isothermal atmosphere. (Refer to section 7 for the magnitude of $\mathcal{E}$ corresponding to this δ.)

Figures 17 and 18 give the observed and computed temperature distributions respectively.[12] In spite of the fact that only the effects of radiative processes were taken into consideration, there are various similar features between them. For example, as could be expected from the foregoing study of the effect of tropospheric water vapor, the height of the tropopause is computed to be greater in low latitudes than in high latitudes. In order to compare this computed height with the observed in more detail, we constructed figure 19. On the left hand side of this figure, the seasonal and latitudinal distribution of the tropopause obtained by Kochanski [34] along the 80°W. meridian is given. According to this, the polar tropopause is highest in July, lowest in winter, and higher in October than in spring. In latitudes greater than 60°N., however, the winter tropopause seems to be slightly higher than the spring tropopause. The observed height of the equatorial tropopause in summer is lower than in other seasons, but this tendency does not invariably appear at other longitudes [13]. On the right hand side of this figure the computed heights of the tropopause are shown. The level of minimum temperature, or that of rapid change of lapse rate, was regarded as the tropopause. Since the number of levels where we compute equilibrium temperature is not enough for exact determination of the tropopause, we determined this level by extrapolating the temperature curve from both the tropospheric and stratospheric sides. The difference of the height of the computed tropopause between pole and equator is about 50 percent of that observed. More specifically, the computed height is too low in low latitudes, though it is close to that observed in high latitudes. Qualitatively, the seasonal variation of the height of the tropopause is predicted well, except for the reversal of spring and winter tropopause in high latitude mentioned above. This computed result can be understood by examining the distribution of water vapor around the

[10] $e_{211} \approx 5e_{200} \approx 25e_{190}$ where, for example, e_{200} is the vapor pressure corresponding to the frost point of 200° K. Above the 9-mb. (31.6-km.) level, mixing ratio instead of frost point was assumed to be constant with height.

[11] Total amount is the same as the case of 190° K. frost point.

[12] The equilibrium temperature of fall and winter in high latitudes is not shown because the radiative equilibrium is too low to be treated by the present scheme alone.

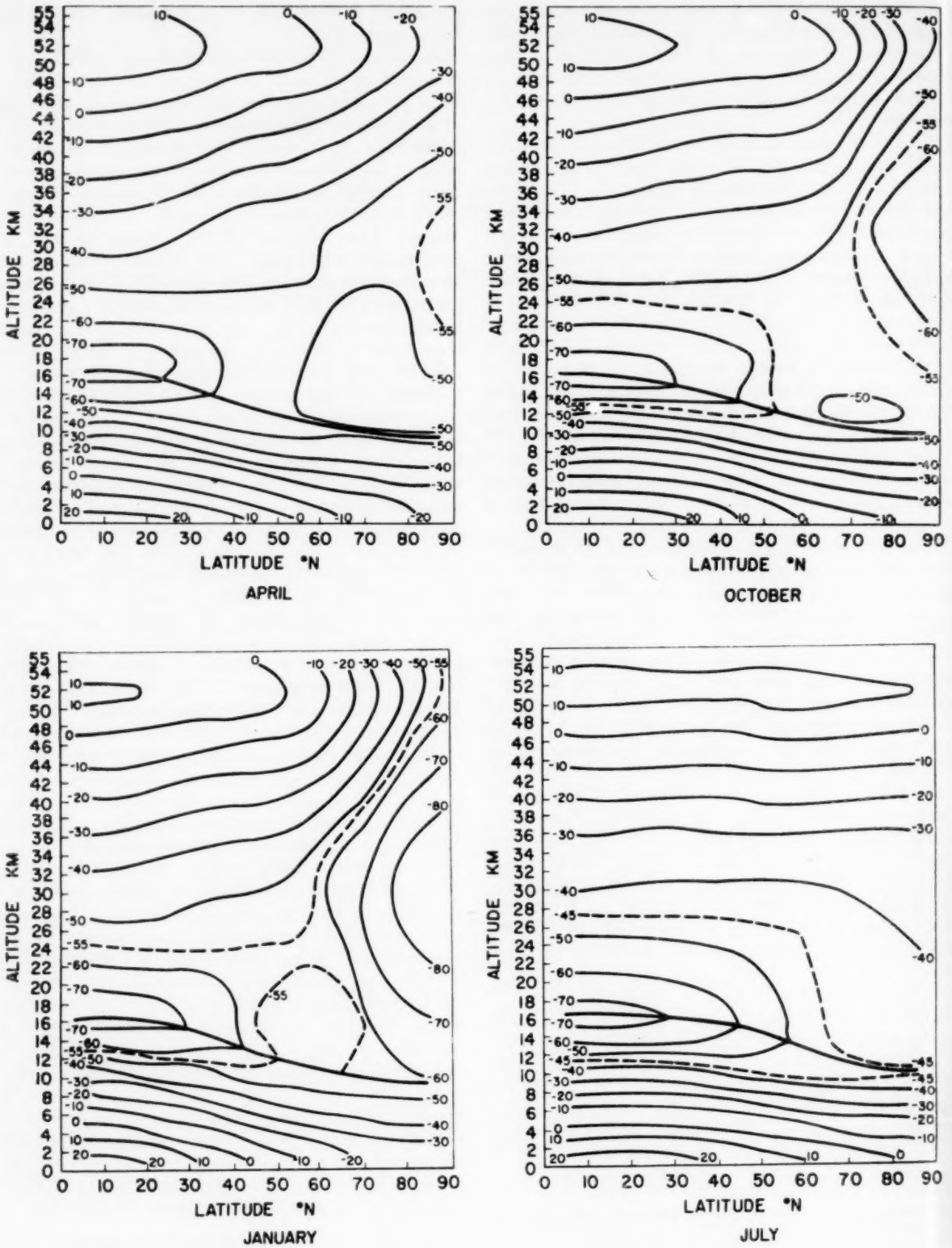

FIGURE 17.—Seasonal and latitudinal distribution of observed temperature compiled by London et al. [35].

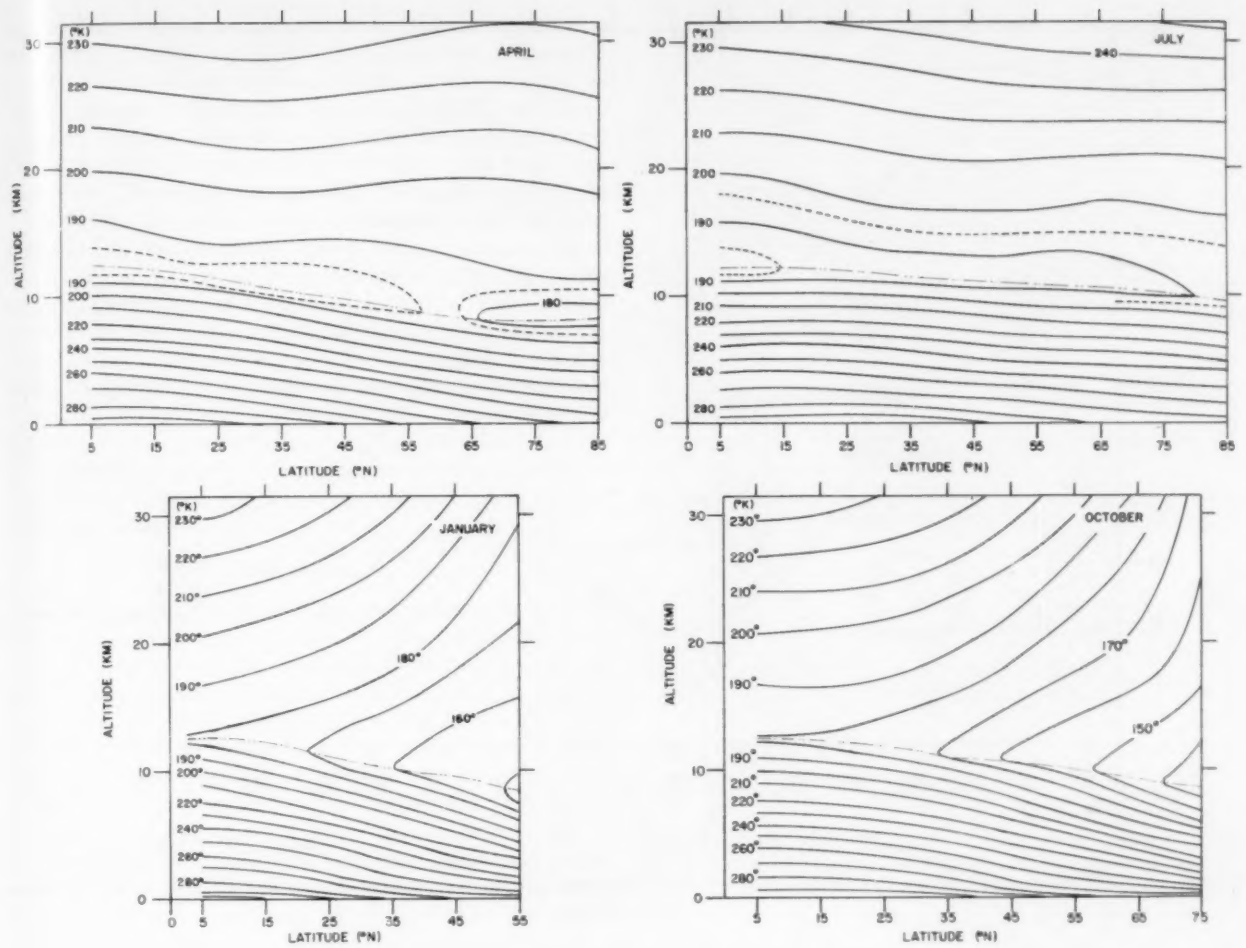

FIGURE 18.—Calculated seasonal and latitudinal distribution of radiative equilibrium. For surface temperature, observed values were adopted ($\delta = 0.07°$ C./day).

tropopause (refer to fig. 9). Tropopause moisture is maximum in summer, minimum in winter, and greater in autumn than in spring. The failure in predicting the height of the tropopause in low latitudes seems to suggest the importance of the dynamical effect which is not considered in the present computation. It is the next interesting task to find out how the height of tropopause is modified by such phenomena as the meridional circulation in the atmosphere, the cyclone waves, and the moist convection in the lower latitudes.

The observed temperature distributions in figure 17 have a very strong minimum around the equatorial tropopause, irrespective of season, and the temperature of this altitude increases with increasing latitude (except in winter when temperature decreases again in high latitudes). The computed temperature has a slight minimum near the equator and increases very slightly (several degrees) with latitude both in spring and summer. However, this tendency is much weaker than the observed one. In fall and winter the computed temperature decreases monotonically with latitude.

In order to clarify this conclusion further, we computed the temperature distributions of regional radiative equilibrium at the 74-mb. (18-km.) level, where the equator to pole temperature increase is maximum. As is shown in the Appendix, we use 10 atmospheric temperature levels in our finite difference scheme, and the 74-mb. level is the second level from the top. For other levels observed temperatures were inserted and assumed to remain constant with time. In other words, we computed the temperature of the second level which would maintain the second layer (34–126 mb. or approximately 15–23 km.) in radiative equilibrium if the observed temperatures are given for all other levels. The purpose of this experiment is to find whether or not this layer is in approximate radiative equilibrium with respect to the remainder of the

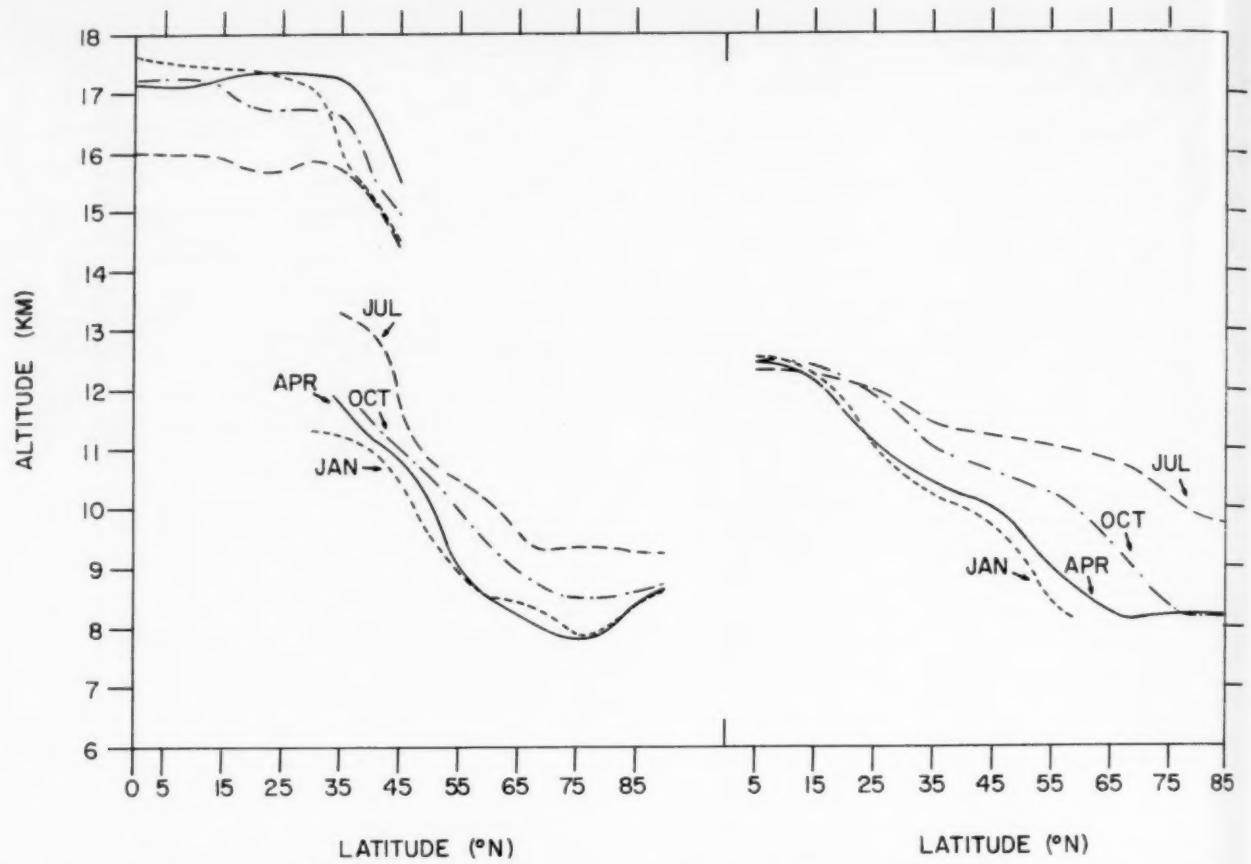

FIGURE 19.—Left side; height of tropopause analyzed by Kochanski [34]. Right side; height of tropopause obtained by equilibrium computation.

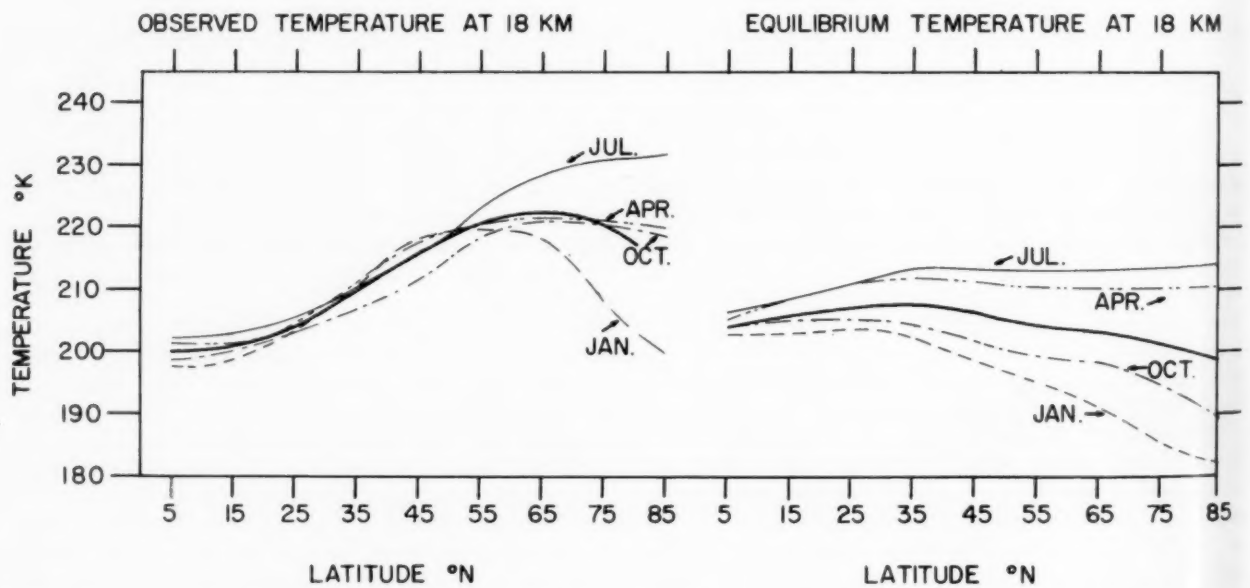

FIGURE 20.—Seasonal and latitudinal distributions of observed (from fig. 17) and computed (right side) temperature of regional radiative equilibrium at the 74-mb. level (18-km. level). As the temperatures of other levels, the observed values were adopted ($\delta = 0.05°$ C./day).

atmosphere, whose temperature we assumed to be that observed. On the left- and right-hand sides of figure 20, observed and computed distributions of temperature at this level are shown. The computed equilibrium temperature reveals some increase with increasing latitude for both summer and spring, but much less than that observed. However the annual averaged equilibrium temperature is more or less isothermal with latitude, whereas the observed mean temperature increases about 17° C. from the equator to the pole. The computed seasonal variations of temperature at this level coincide qualitatively with those observed in higher latitudes, i.e., it is warmest in summer and coldest in winter. In middle latitudes, however, the observed temperature is relatively warm in winter, whereas the computed temperature is coldest. In view of the fact that the degree of baroclinicity is maximum in winter, it would probably be necessary to consider dynamical effects to explain this phenomenon. We shall discuss this problem later.

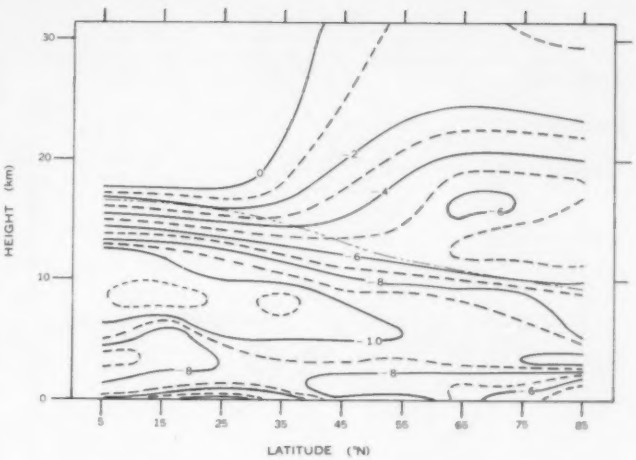

FIGURE 21.—Computed distribution of annual mean rate of temperature change (°C./day).

HEAT BUDGET

The annual mean rate of radiative temperature change.—So far, we have concentrated on a discussion of the computation of radiative equilibrium and have found that the distribution of the radiative equilibrium temperature reveals some of the interesting characteristics observed in the atmosphere. In order to understand these results, however, it is necessary to compute the radiative heat budget of the atmosphere. The distribution of radiative imbalance in the atmosphere would also suggest the effects we should expect on physical processes other than radiative processes. We shall devote the remaining portion of this section to the results of our computation of the radiative heat budget.

The observed distribution of temperature, which was compiled by London et al. [35, 36] and shown in figure 17, was adopted for this computation. The distributions of various atmospheric absorbers were described in section 6. The scheme of computation is similar to that for radiative equilibrium except for the inclusion of the temperature effect on the absorptivity in the calculation of radiative transfer due to the 15μ band of carbon dioxide.

The computed mean annual distribution of the rate of temperature change obtained by taking the average of the heat budget of the four seasons is shown in figure 21. In the stratosphere there is an area of very slight heating in low latitudes and one of cooling in high latitudes. In the troposphere, as is expected, cooling predominates and the area of strong cooling is located in the upper troposphere.

Mean vertical distributions of radiative heat balance components.—In order to determine the relative importance of various radiative processes at each level, hemispheric area mean vertical distributions of temperature changes due to the absorption of solar radiation by water vapor, carbon dioxide, and ozone, and those due to the atmospheric radiation of these gases are shown in figure 22. In the

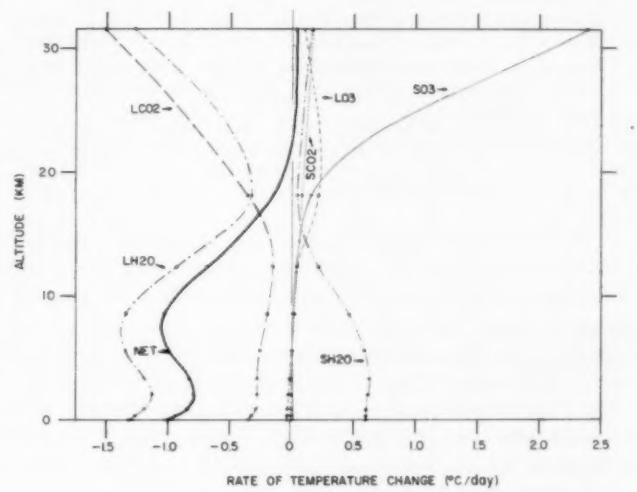

FIGURE 22.—Mean vertical distributions of various heat balance components (°C./day). "Net" means the vertical distribution of the net rate of temperature change. For further explanation refer to legend of figure 13.

stratosphere the strong increase of heating with height, due to the absorption of solar radiation by ozone, mainly compensates for that of cooling due to the long wave radiation by both carbon dioxide and water vapor. Owing mainly to the absorption of the radiation coming from the warm ground surface, the radiative transfer of the 9.6μ band of ozone also has a heating effect around the height of 18 km. Relatively speaking, ozone has very important heating effects around this height, where the magnitudes of other radiative processes are rather small.

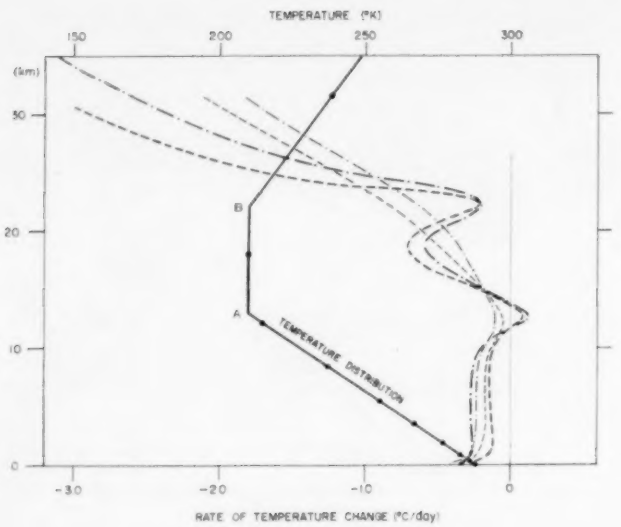

FIGURE 23.—Vertical distribution of temperature change due to the 15μ band of carbon dioxide (°C./day). Heavy continuous line is vertical temperature distribution. Plass' [51] results: Heavy dashed line—without temperature effect; heavy dash-dotted line—with temperature effect. Our results: Thin dashed line—without temperature effect; thin dash-dotted line—with temperature effect.

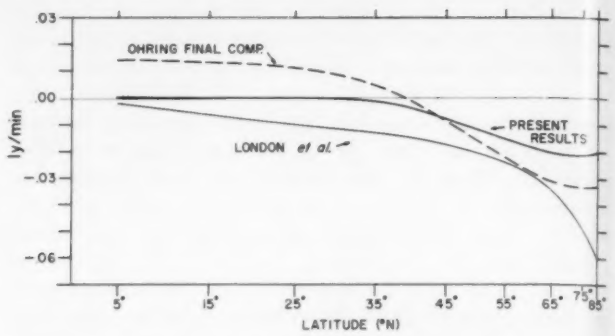

FIGURE 24.—Latitudinal distribution of heat budget in the stratosphere (ly./min.). Heavy solid line—our results. Dashed line—Ohring's [48] final results. Thin solid line—results of London et al. [35].

The latitudinal mean effect of the 15μ band of carbon dioxide turned out to be cooling. Because of the weak emission and the absorption of radiation from the warmer regions above and below, this cooling is at a minimum around the tropopause. Above this level it increases with height due to the radiation escaping to outer space. The importance of the 15μ band of carbon dioxide as a cooling effect in the stratosphere has already been emphasized by London et al. [35] and Ohring [48]. However, according to Goody [20], the 15μ band of carbon dioxide has a rather strong heating effect at the tropopause. The reason for this strong heating could be found from a careful examination of Plass' [51] results of the temperature change due to this band. In figure 23 the dash-dotted and dashed heavy lines show the vertical distribution of the rate of temperature change respectively, with and without the temperature effect mentioned before. If we compare these distributions with the vertical distribution of temperature adopted by Plass, we notice that he obtained a sharp maximum heating or minimum cooling at levels A and B where the lapse rate of temperature suddenly changes; i.e., the second derivative of temperature with height has an infinitely large positive value. Therefore, the heating he obtained is a peculiar phenomenon of the tropopause and is not always a characteristic feature of the lower stratosphere. It depends on the magnitude of the discontinuity of lapse rate he assumes for his calculation. This result suggests the necessity for the computation of the latitudinal distribution of heat sources and sinks in the lower stratosphere as well as at the tropopause which Goody [20] computed. For comparison, the results which are obtained from our scheme are also included in the same figure. Since our computations were made for fewer levels than those of Plass [51], his results include many more detailed features. The overall features of stratospheric cooling do not, however, differ from each other. The cooling obtained by including the temperature effect on CO_2 is smaller in the stratosphere and is larger in the troposphere than that obtained by neglecting it. The heating due to the absorption of solar radiation by carbon dioxide is very small compared with the effects of other processes. However around the tropopause, where the contributions of various radiative processes are at a minimum, it is not always negligible.

The cooling due to the long wave radiation by water vapor is maximum in the upper troposphere owing to the sharp decrease of water vapor with height. This constitutes the emission layer mentioned before. The heating due to the absorption of solar radiation by water vapor is mainly important in the troposphere and is very small in the stratosphere as compared with the magnitude of other effects.

Summing all these contributions, the net rate of temperature change due to all of these radiative processes is also shown in figure 22. Owing to the sharp increase of heating by ozone with increasing altitude, this net rate has the effect of intensifying the existing stratospheric inversion. This result is consistent with the typical inversion which appeared in the stratosphere of our radiative equilibrium. The degree of radiative imbalance is largest in the upper troposphere and becomes smaller as we go higher into the stratosphere. This result seems to be reasonable because one may expect more transfer of tropospheric energy into the lower stratosphere than to the upper stratosphere. However it must also be kept in mind

that the higher the altitude, the less accurate is our scheme of computation and the assumed distributions of the absorbing gases. Therefore in order to verify these results it is necessary to make more careful observations of the distributions of gases and to have more exhaustive laboratory experiments to determine the absorptivity of these gases.

Latitudinal distributions of radiative heat balance components.—Next, we shall discuss the latitudinal distribution of heat sources and sinks in the stratosphere. In figure 24 the results of our computation of the stratospheric heat budget are shown together with that of London et al. [35] and the revised result by Ohring [48]. The heights of the tropopause used for this computation are the same as those compiled by London [36]. The difference among these results might be considered to be a manifestation of the degree of ambiguity involved in this type of computation. The one common feature is, however, the increase of the tendency of cooling with increasing latitude.

In order to find out how the various radiative processes combine to make up this latitudinal distribution of stratospheric heat budget, we examined the contribution of each process at the 74-mb. (18-km.) level,[13] where the temperature increases most sharply with increasing latitude. In figure 25 are shown the latitudinal variations of the annual average of the rate of temperature changes due to the radiative processes. At this level the heating factors are the long wave radiation of ozone and the absorption of the solar radiation by ozone, carbon dioxide, and water vapor; the cooling factors are the long wave radiation by carbon dioxide and water vapor.

As we could expect, the heating due to the absorption of solar radiation by water vapor and carbon dioxide decreases with increasing latitude; that by ozone, however, hardly decreases at all owing to the sharp lat increase of ozone at this level and the increase of the zenith angle of the sun.

The cooling due to the long wave radiation of water vapor is more or less constant with latitude in spite of the fact that the troposphere is cooler with increasing latitude. This is partly due to the slight latitudinal decrease of water vapor contained in this layer (34–126 mb. or approximately 23–15 km; refer to Appendix I). Another important reason is the lowering with increasing latitude of the height of the effective source of tropospheric emission which reaches the lower stratosphere. As was pointed out by Simpson [56] the more water vapor that exists in the atmosphere, the lower is the temperature of the effective source of long wave radiation leaving the atmosphere, because when water vapor is abundant, the radiation which is emitted from the lower atmosphere is absorbed again by the water vapor existing in higher altitudes.

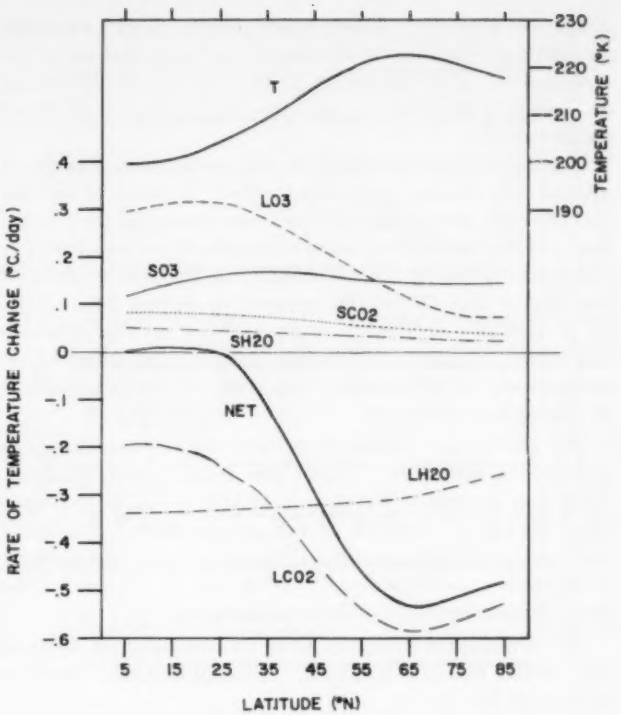

FIGURE 25.—Latitudinal distribution of annual mean rate of temperature change due to various radiative processes at 74-mb. level (18-km. level). T denotes the annual mean temperature in degrees Kelvin. For further explanation refer to legend of figure 13.

The heating due to the 9.6μ band of ozone increases with latitude up to about 30° N. due to the latitudinal increase of ozone, but it decreases again in higher latitudes because of the decrease of the temperature of the earth's surface with latitude. This result coincides with Goody's [20] conclusion that the latitudinal variation of heating due to the 9.6μ band of ozone could hardly be a factor to explain the latitudinal increase of temperature in the lower stratosphere because the effect of the sharp increase of the ozone amount with increasing latitude at this 18-km. level is countered by that of the decrease of the earth's surface temperature with increasing latitude.

The cooling due to the 15μ band of carbon dioxide sharply increases with increasing latitude because of both the latitudinal increase of temperature at this level and the latitudinal decrease of the temperature of the troposphere. A recent computation by Brooks [7] shows the same tendency, although the magnitude of the rate of the cooling he obtained is slightly larger than ours [14] (by

[13] Since the rates of the temperature change at this level were obtained by subtracting the net flux at the 126-mb. (15-km.) level from that at the 34-mb. (23-km.) level, it might be more reasonable to regard them as the average rates of this whole layer.

[14] This discrepancy might be due partly to his neglect of the temperature effect on absorption of carbon dioxide. In order to compare his results with ours, we integrated his results to obtain the average rate of temperature change between the 34-mb. and 126-mb. levels

616949—61——4

about 0.2° C./day). This tendency explains why we could not simulate sufficiently the increase of temperature in the stratosphere with increasing latitude by our computation of radiative equilibrium despite the favorable effect of water vapor.

The latitudinal increase of the cooling of the layer around the 18-km. level due to the 15μ band of carbon dioxide and the cooling in the lower stratosphere of high latitude due to the long wave radiation of water vapor are the main causes of the net cooling in the stratosphere of the higher latitude which appears in figures 21 and 24. It is possible to speculate on various processes which have been suggested by various authors and which could compensate for this cooling tendency of the stratosphere in higher latitudes, e.g.:

(1) Northward transport of heat by large-scale eddies at the 100-mb. level against the temperature gradient. This was suggested by Starr and White [58] based upon their statistical analysis of radiosonde data. The moist convection at low latitudes, which penetrates into the high troposphere, could supply heat in compensation for the heat sink caused by northward transport.

(2) A meridional circulation in the stratosphere directed downward in high latitudes. This possibility was suggested by Brewer [6].

(3) Upward transfer of heat energy by large-scale disturbances of higher latitude accompanied by the release of potential energy into kinetic energy.

In order to determine the process or processes of major importance, it would be desirable to perform a careful investigation of the distributions of radioactive debris introduced into the high atmosphere by atomic explosions and those of rare gases as well as to conduct numerical experiments by use of advanced general circulation models which include both the hydrodynamical behavior of the atmosphere and radiative transfer.

9. CONCLUSIONS

(1) The vertical distribution of radiative equilibrium temperature was obtained as the balance among various radiative processes, i.e., the absorption of solar radiation by water vapor, carbon dioxide, and ozone, and the long wave radiation by these three gases. For the surface temperature, the observed value was adopted. Below the level of 11 km., we get a nearly dry adiabatic lapse rate except near the ground where there is a superadiabatic layer. Above 11 km. there appears a radiative equilibrium stratosphere, where temperature increases slowly with altitude, mainly because of the increase of the absorption of solar radiation by ozone. The computed temperature near the tropopause is much cooler than observed (by 20°–40° C.) as a result of the neglect of other processes such as dry and moist convection and vertical transfer of heat by the large-scale eddies.

(2) The latitudinal and seasonal distributions of the computed tropopause heights compare fairly well with those of the observed polar tropopause. They are highest in low latitude and lowest in high latitude; they are highest in summer, lowest in winter, and higher in fall than in spring. However, the tropopause in low latitudes is considerably lower than the observed equatorial tropopause. The pole to equator difference of height of the computed tropopause is about 50 percent smaller than that observed.

(3) The distribution of the computed height of the tropopause has a close correspondence with that of water vapor in the upper troposphere. Generally speaking, when more water vapor exists around the tropopause, the computed height of the tropopause is higher and its temperature is lower.

(4) The computed temperature of radiative equilibrium at the 18-km. level increases slightly (about 7° C.) from equator to pole both in summer and spring, but decreases monotonically in winter and fall. The actually observed annual mean temperature increases about 20° C. from equator to pole at this level. This tendency is maximum in summer.

(5) The large range of computational results of the radiative equilibrium temperature for the observed range of stratospheric moisture suggests a strong necessity for further accurate water vapor measurements in the stratosphere.

(6) According to our computation of radiative heat budget, in the stratosphere, net heating effects include the absorption of solar radiation by water vapor, carbon dioxide (not negligible around the tropopause), and ozone and the atmospheric radiation due to the 9.6μ band of ozone; net cooling effects include the long wave radiation by water vapor and carbon dioxide. Summing all these contributions we obtain a very weak heating in low latitudes and a rather strong cooling in the lower stratosphere at high latitudes. This cooling is too large to be considered as the product of uncertainties involved in the computation and must be compensated for by heat transfer processes other than radiation.

(7) In order to verify conclusion (4), the study of various processes contributing to the heat budget of the layer around the 18-km. level, where the observed temperature most sharply increases with latitude, was performed. The long wave radiation by water vapor has a tendency to maintain the existing latitudinal gradient. The effects of ozone have the same tendency in low latitudes but not in high latitudes. The long wave radiation by carbon dioxide has a strong tendency to destroy the existing latitudinal increase of temperature. The net effect of these radiative processes could barely maintain the stratospheric temperature approximately constant with latitude and hardly explains the sharp latitudinal temperature increase observed in the stratosphere.

10. CRITICAL COMMENTS AND FUTURE WORK

In order to obtain simply the radiative equilibrium of the atmosphere, we have made various assumptions. They should, however, be removed for the more detailed discussion of the phenomenon. One of the most important assumptions is the neglect of the effect of clouds. Therefore, a method of incorporating the effect of clouds has been worked out and is being programmed for the high speed computer. The influence of clouds on the radiative equilibrium and the earth's climate is one of the major items which we should investigate before we incorporate the radiative processes into the general circulation models.

Since we completed the writing of this paper, new studies on the absorptivities and distributions of atmospheric gases have been published. These new data will be considered in a forthcoming study.

ACKNOWLEDGMENTS

The authors wish to express their hearty thanks to Dr. J. Smagorinsky who originally suggested that this work be done and has given us very helpful suggestions and constant encouragement throughout this work; and to Drs. D. K. Lilly, G. Yamamoto, D. Q. Wark, and S. Fritz who have always given us many valuable suggestions. They are also indebted to Mr. R. Strickler who carefully checked the computation scheme and improved the coding, to Mr. E. Riesenberg who did the programming throughout our study, and to Mr. E. Rayfield and Mrs. J. Snyder who assisted with the preparation of the figures and manuscript, respectively.

APPENDIX I

VERTICAL COORDINATE SYSTEM

In order to perform the numerical computation of the radiative change of temperature, it is first of all necessary to specify the levels where we carry the values of temperature. Needless to say, the more levels we have the smaller the truncation errors due to differencing. However, it is wise to adopt the minimum number of levels consistent with the small truncation error required, because an increase in the number of levels is accompanied by a large increase in the amount of computation.

The coordinate system used in our computation is the one proposed by Smagorinsky for an advanced model to study the general circulation of the atmosphere. This system is designed in such a way as to give us a higher resolution in the surface boundary layer and in the stratosphere where temperature varies remarkably with respect to pressure. Therefore, this coordinate system is very convenient in minimizing the number of layers which are necessary to express the vertical structure of the atmosphere. According to the proposal of Smagorinsky, his σ-coordinate system is connected with the p-coordinate system by the following equation.

$$p/p_* = \sigma^{\frac{1}{2}}(3-2\sigma) \qquad \text{(A-1)}$$

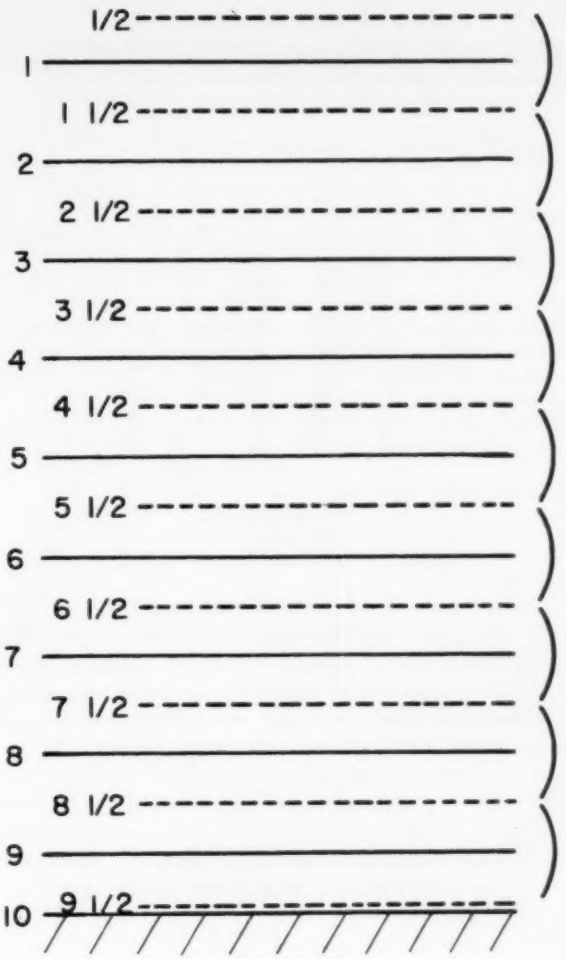

FIGURE 26.—Indexing of layers. I=½ : top of atmosphere, I=9½ : bottom of atmosphere. I=10 : earth's surface (same height with level 9½).

where p_* is the pressure at the earth's surface. Throughout our computation this p_* is assumed to be 1000 mb. Using this system, we divided the atmosphere into nine layers; i.e., into nine equal σ-intervals, which are shown in figure 26. Also, in table 5 the height and pressure of each level and the pressure thickness of each layer are shown. The boundaries between two neighboring layers are described by half integers. Temperature is specified at each integer level. Near the ground surface, the height of the level changes approximately logarithmically so that temperature could vary approximately linearly from one level to another. In the formulation of finite difference equations (Appendix III) it is assumed that temperature could be linearly interpolated with respect to this σ-coordinate system.

TABLE 5.—*Illustration of σ-coordinate system and the list of input specified for each σ-level. Δp is pressure thickness of each layer, H is height of each level. (ICAO standard atmosphere; adjustment was made such that the height of 1000 mb. is zero)*

I	σ	p (mb.)	Δp (mb.)	H (km.)
½	0.0000	0		∞
1	0.0555	9	34	31.6
1½	.1111	34		23.0
2	.1666	74	92	18.0
2½	.2222	126		14.7
3	.2777	189	133	12.0
3½	.3333	259		10.1
4	.3888	336	158	8.3
4½	.4444	417		6.8
5	.4999	500	166	5.5
5½	.5555	583		4.3
6	.6110	664	158	3.3
6½	.6667	741		2.5
7	.7221	811	133	1.7
7½	.7778	874		1.1
8	.8332	926	92	.64
8½	.8889	966		.3
9	.9443	991	34	.07
9½	1.0000	1000		.00
10	1.0000	1000		.00

APPENDIX II

EMISSIVITIES AND ABSORPTIVITIES

The values of ϵ_f^W, $\bar{\epsilon}_f^W$, $\mathcal{E}_f^G(G=C \text{ or } O)$, and $a^G(G=W, C, \text{ or } O)$ are tabulated for every increment of 0.5 of the logarithm of effective optical thickness. Using this table, the values of absorptivities were determined for any value of optical thickness by linear interpolation with respect to the logarithm of effective optical thickness.

In the upper troposphere the mixing ratio of water vapor changes approximately exponentially with height. Therefore, when we computed the optical thickness of water vapor, the exponential variation of water vapor was assumed between the neighboring integer levels where the mixing ratio was specified.

APPENDIX III

FORMULATION OF THE FINITE DIFFERENCE EQUATION

In order to show how we changed the equations for the temperature change due to atmospheric radiation into the finite difference equation, we shall transform the second term of equation (17) into finite difference form as an example. If we consider the case when the index of the height z is $I+\frac{1}{2}$ the second term should be written as

$$\int_{b_{I+\frac{1}{2}}^G}^{b_{\frac{1}{2}}^G} \mathcal{E}_f(y)\pi db^G = \int_{b_I^G}^{b_{\frac{1}{2}}^G} \mathcal{E}_f^G(y)\pi db^G + \sum_{K=1}^{I-1} (b_K^G - b_{K+1}^G)\cdot \mathcal{E}_f^G(K+\tfrac{1}{2}, I+\tfrac{1}{2}) + \int_{b_{I+\frac{1}{2}}^G}^{b_I^G} \mathcal{E}_f^G(y)\pi db^G \qquad \text{(A-2)}$$

where, for example, $\mathcal{E}_f^G(K+\frac{1}{2}, I+\frac{1}{2})$ is the band absorptivity of the layer of optical thickness $u_r(K+\frac{1}{2}, I+\frac{1}{2})$ $(\equiv|(u_r)_{K+1/2}-(u_r)_{I+1/2}|)$, and b_K^G is the abbreviation of b^G for temperature T_K.

Since we do not know the temperature at the top of the atmosphere ($T_{\frac{1}{2}}$) we made the following assumption for the sake of simplicity (refer to equation (41)),

$$T_{\frac{1}{2}} = T_1 \qquad \text{(A-3)}$$

and adopted the following approximation:

$$\int_{b_{I+\frac{1}{2}}^G}^{b_I^G} \mathcal{E}_f^G(y)\pi db^G \approx (b_I^G - b_{I+\frac{1}{2}}^G)\cdot \left\{ (1/u_r(I, I+\tfrac{1}{2})) \int_0^{u_r(I,I+\frac{1}{2})} \mathcal{E}_f^G(u_r)du_r \right\}. \qquad \text{(A-4)}$$

The integral (A-2) is to be approximated as follows:

$$\int_{b_{I+\frac{1}{2}}^G}^{b_{\frac{1}{2}}^G} \mathcal{E}_f^G(y)\pi db^G \approx \sum_{K=1}^{I-1} (b_K^G - b_{K+1}^G)\cdot \mathcal{E}_f^G(K+\tfrac{1}{2}, I+\tfrac{1}{2}) + (b_I^G - b_{I+\frac{1}{2}}^G)\left\{ (1/u_r(I, I+\tfrac{1}{2})) \int_0^{u_r(I,I+\frac{1}{2})} \mathcal{E}_f^G(u_r)du_r \right\} \qquad \text{(A-5)}$$

The quantity in the second bracket of the third term was computed by interpolating the table. The reason we adopted this special treatment is the highly non-linear change of $\mathcal{E}_f^G$ with respect to u_r when u_r tends to zero. Based upon equation (1), the temperature change at integer levels due to the long wave radiation of water vapor is to be expressed by the following finite difference form:

$$\left(\frac{\partial T_K}{\partial t}\right)_{LR}^W = \frac{g}{c_p} \frac{1}{p_{K+\frac{1}{2}} - p_{K-\frac{1}{2}}} [F_{K+\frac{1}{2}}^W - F_{K-\frac{1}{2}}^W] \qquad \text{(A-6)}$$

$$(K=1, 2, \ldots, 9)$$

The finite difference equation for the rate of temperature change due to the absorption of solar radiation will not be described here, because it can be derived from equation (27) without difficulty.

REFERENCES

1. A. Adel and C. O. Lampland, "Atmospheric Absorption of Infrared Solar Radiation at the Lowell Observatory; 5.5 ~14μ," *Astrophysical Journal*, vol. 91, 1940, pp. 481–487.
2. F. R. Barclay, M. J. W. Elliott, P. Goldsmith, and J. V. Jellay, "A Direct Measurement of the Humidity in the Stratosphere Using a Cooled-Vapor Trap," *Quarterly Journal of the Royal Meteorological Society*, vol. 86, No. 368, Apr. 1960, pp. 259–264.
3. E. W. Barrett, L. R. Herndon, Jr., and H. J. Carter, "Some Measurements of the Distribution of Water Vapor in the Stratosphere," *Tellus*, vol. 2, No. 4, Nov. 1950, pp. 302–311.
4. W. S. Benedict, "Theoretical Studies of Infrared Spectra of Atmospheric Gases," *Final Report* on Contract AF19(604)-1001, Laboratory of Astrophysics and Physical Meteorology, Johns Hopkins University, June 1956, 66 pp.
5. D. Brunt, *Physical and Dynamical Meteorology*, 2d Ed., Cambridge University Press, Cambridge, 1941, (pp. 129–134).
6. A. W. Brewer, "Evidence for a World Circulation Provided by the Measurements of Helium and Water Vapour Distribution in the Stratosphere," *Quarterly Journal of the Royal Meteorological Society*, vol. 75, No. 326, Oct. 1949, pp. 351–363.
7. D. L. Brooks, "The Distribution of Carbon Dioxide Cooling in the Lower Stratosphere," *Journal of Meteorology*, vol. 15, No. 2, Apr. 1958, pp. 210–219.

8. R. A. Craig, "The Observations and Photochemistry of Atmospheric Ozone and Their Meteorological Significance," *Meteorological Monographs*, American Meteorological Society, vol. 1, No. 2, 1950, 50 pp.
9. H. A. Daw, "Transmission of Radiation Through Water Vapor Subject to Pressure Broadening in the Region 4.2 microns to 23 microns," *Technical Report No. 10*, Contract AF19(122)–392, University of Utah, 1956.
10. G. M. B. Dobson, A. W. Brewer, and B. M. Cwilong, "Meteorology of the Lower Stratosphere," *Proceedings of the Royal Society of London*, Ser. A, vol. 185, No. 1001, Feb. 12, 1946, pp. 144–175.
11. W. M. Elsasser, "Heat Transfer by Infrared Radiation in the Atmosphere," *Harvard Meteorological Studies* No. 6, 1942, 107 pp.
12. R. Emden, "Über Strahlungsgleichgewicht und Atmosphärische Strahlung: Ein Beitrag zur Theorie der Oberen Inversion," *Sitzungsberichte*, Akademie der Wissenschaften, München, No. 1, 1913, pp. 55–142.
13. H. Flohn, "Kontinentalität und Ozeanität in der Freien Atmosphäre," *Meteorologische Zeitschrift*, vol. 60, 1943, pp. 325–331.
14. F. E. Fowle, "The Spectroscopic Determination of Aqueous Vapor," *Astrophysical Journal*, vol. 35, 1912, pp. 149–162.
15. F. E. Fowle, "The Transparency of Aqueous Vapor," *Astrophysical Journal*, vol. 42, 1915, pp. 394–411.
16. F. E. Fowle, "Water Vapor Transparency to Low Temperature Radiation," *Smithsonian Miscellaneous Collections*, vol. 68, No. 8, 1917.
17. D. M. Gates, D. G. Murcray, C. C. Shaw, and R. J. Herbold, "Near Infrared Solar Radiation Measurements by Balloon to an Altitude of 100,000 Feet," *Journal of the Optical Society of America*, vol. 48, 1959, pp. 1010–1016.
18. Geophysical Research Directorate, U. S. Air Force, *Handbook of Geophysics*, Rev. Ed., Macmillan and Co., New York, 1960.
19. E. Gold, "The Isothermal Layer of the Atmosphere and Atmospheric Radiation," *Proceedings of the Royal Society of London*, Ser. A., vol. 82, No. 551, Feb. 16, 1909, pp. 43–70.
20. R. M. Goody, "The Thermal Equilibrium at the Tropopause and the Temperature of the Lower Stratosphere," *Proceedings of the Royal Society of London*, Ser. A, vol. 197, 1949, pp. 487–505.
21. F. W. P. Götz, "Ozone in the Atmosphere," *Compendium of Meteorology*, American Meteorological Society, Boston, 1951, pp. 275–291.
22. E. H. Gowan, "The Effect of Ozone on the Temperature of the Upper Atmosphere," *Proceedings of the Royal Society of London*, Ser. A, vol. 120, 1928, pp. 655–669.
23. E. H. Gowan, "Ozonosphere Temperatures Under Radiative Equilibrium," *Proceedings of the Royal Society of London*, Ser. A, vol. 190, No. 1021, July 1947, pp. 219–226.
24. W. J. Humphreys, "Vertical Temperature-Gradients of the Atmosphere, Especially in the Region of the Upper Inversion—A Suggested Explanation of the Isothermal Layer," *Astrophysical Journal*, vol. 29, No. 1, Jan. 1909, pp. 14–32.
25. H. G. Houghton, "On the Annual Heat Balance of Northern Hemisphere," *Journal of Meteorology*, vol. 11, No. 1, Feb. 1954, pp. 1–9.
26. J. T. Houghton and J. S. Seeley, "Spectroscopic Observations of the Water Vapour Content of the Stratosphere," *Quarterly Journal of the Royal Meteorological Society*, vol. 86, No. 369, July 1960, pp. 358–370.
27. J. N. Howard, D. L. Burch, and D. Williams, "Near-Infrared Transmission Through Synthetic Atmospheres," *Geophysical Research Papers*, No. 40, Air Force Cambridge Research Center, AFCRC–TR–55–213, 1955, 244 pp.
28. F. C. Y. Inn and Y. Tanaka, "Absorption Coefficient of Ozone in the Ultraviolet and Visible Regions," *Journal of the Optical Society of America*, vol. 43, No. 10, Oct. 1953, pp. 870–873.
29. E. C. Y. Inn and Y. Tanaka, "Comparison of Recently Recorded Ozone Absorption Coefficients in the Visible and Ultraviolet Regions," *Conference on Ozone*, Armour Research Foundation, 1956, pp. 263–268.
30. F. S. Johnson, "The Solar Constant," *Journal of Meteorology*, vol. 11, No. 6, Dec. 1954, pp. 431–439.
31. L. D. Kaplan, "The Infrared Spectrum of Lower Stratosphere and Its Importance in the Heat Balance," *Scientific Proceedings of the International Union of Geodesy and Geophysics, Association of Meteorology, 10th General Assembly, Rome, Sept. 1954*, London, 1956, pp. 583–592.
32. H. H. Kimball, "Measurements of Solar Radiation Intensity and Determinations of Its Depletion by the Atmosphere," *Monthly Weather Review*, vol. 58, No. 2, Feb. 1930, pp. 43–52.
33. J. I. King, "Line Absorption and Radiative Equilibrium," *Journal of Meteorology*, vol. 9, No. 5, Oct. 1952, pp. 311–321.
34. A. Kochanski, "Cross Sections of the Mean Zonal Flow and Temperature Along 80° W.," *Journal of Meteorology*, vol. 12, No. 2, Apr. 1955, pp. 95–106.
35. J. London, G. Ohring, and I. Ruff, "Radiative Properties of the Stratosphere," *Final Report*, Contract AF19(604)–1285, Research Div. College of Engineering, New York University, 1956, 48 pp.
36. J. London, "A Study of the Atmospheric Heat Balance," *Final Report*, Contract AF19(122)–165, Research Div. College of Engineering, New York University, 1957, 99 pp.
37. J. McDonald, "Direct Absorption of Solar Radiation by Atmospheric Water Vapor," *Journal of Meteorology*, vol. 17, No. 3, June 1960, pp. 317–328.
38. L. Machta, "Meteorology and Radioactive Fallout," World Meteorological Organization, *Bulletin*, vol. 9, No. 2, Apr. 1960, pp. 64–70.
39. F. Möller, "Die Wärmestrahlung des Wasserdampfes in der Atmosphäre," *Beiträge zur Geophysik*, vol. 58, No. 1/2, 1941, pp. 11–61.
40. F. Möller, "Zur Erklärung der Stratosphärentemperatur," *Naturwissenschaften*, vol. 31, 1943, p. 148.
41. F. Möller and S. Manabe, "Über das Strahlungsgleichgewicht in der Atmosphäre," *Zeitschrift für Meteorologie*, (in press).
42. R. Mügge and F. Möller, "Zur Berechnung von Strahlungsströmen und Temperaturänderungen in Atmosphären von Beliebigen Aufbau," *Zeitschrift für Geophysik*, vol. 8, 1932, pp. 53–64.
43. R. J. Murgatroyd, P. Goldsmith, and W. E. H. Hollings, "Some Recent Measurements of Humidity from Aircraft Up to Heights of about 50,000 Ft. over Southern England," *Quarterly Journal of the Royal Meteorological Society*, vol. 81, No. 350, Oct. 1955, pp. 533–537.
44. R. J. Murgatroyd, "Some Recent Measurements by Aircraft of Humidity up to 50,000 Ft. in the Tropics and Their Relationship to the Meridional Circulation," *Proceedings of the Symposium on Atmospheric Ozone. Oxford, 20–25 July 1959*, I.U.G.G. Monograph No. 3, Paris, 1960, p. 30.
45. C. Normand, "Atmospheric Ozone and the Upper-Air Conditions," *Quarterly Journal of the Royal Meteorological Society*, vol. 79, No. 339, Jan. 1953, pp. 39–50.
46. Ny Tsi-Ze et Choong Shin-Piaw, "L'Absorption de la Lumière par l'Ozone entre 3050 et 3400 Å (Région des bandes de Huggins)," *Comptes Rendus, Académie des Sciences, Paris*, vol. 195, 1932, pp. 309–311.
47. Ny Tsi-Ze et Choong Shin-Piaw, "L'Absorption de la Lumière par l'Ozone entre 3050 et 2150 Å," *Comptes Rendus, Académie des Sciences, Paris*, vol. 196, 1933, pp. 916–918.
48. G. Ohring, "The Radiation Budget of the Stratosphere," *Scientific Report No. 1*, Contract AF19(604)–1738, Dept. of Meteorology and Oceanography, New York University, June 1957, 42 pp.

49. N. A. Phillips, "The General Circulation of the Atmosphere: A Numerical Experiment," *Quarterly Journal of the Royal Meteorological Society*, vol. 82, No. 352, Apr. 1956, pp. 123–164.

50. G. N. Plass, "The Influence of the 9.6 μ Ozone Band on the Atmospheric Infra-Red Cooling Rate," *Quarterly Journal of the Royal Meteorological Society*, vol. 82, No. 351, Jan. 1956, pp. 30–44.

51. G. N. Plass, "The Influence of the 15 μ Carbon Dioxide Band on the Atmospheric Infra-Red Cooling Rate," *Quarterly Journal of the Royal Meteorological Society*, vol. 82, No. 353, July 1956, pp. 310–324.

52. J. Pressman, "The Latitudinal and Seasonal Variations of the Absorption of Solar Radiation by Ozone," *Journal of Geophysical Research*, vol. 59, No. 4, Dec. 1954, pp. 485–498.

53. R. D. Richtmyer, *Difference Method for Initial Value Problems*, Interscience Publishers, Ltd., New York, 1957, (see p. 93).

54. O. E. T. Robert, "On Radiative Diffusion in the Atmosphere," *Proceedings of the Royal Society of Edinburgh*, vol. 50, 1929–30, pp. 225–242.

55. T. Sasamori, "The Temperature Effect on the Absorption of 15 microns Carbon Dioxide Band," *Science Reports of the Tohoku University, Ser. 5, Geophysics*, vol. 11, No. 3, Dec. 1959, pp. 149–161.

56. G. Simpson, "Some Studies in Terrestrial Radiation," *Memoirs of the Royal Meteorological Society*, vol. 2, No. 16, 1928, pp. 69–95.

57. J. Smagorinsky, General Circulation Experiments with the Primitive Equations: The Basic Experiment, 1961 (in preparation).

58. V. P. Starr and R. M. White, "Balance Requirements of the General Circulation," *Geophysical Research Papers* No. 35, Geophysical Research Directorate, Air Force Cambridge Research Center, 1954.

59. C. Størmer, "Height of Mother of Pearl Clouds Observed in Southern Norway During 1926–1934," *Nature*, vol. 145, 1940, pp. 221–222.

60. M. Summerfield, "Pressure Dependence of the Absorption in the 9.6 micron Band of Ozone," Doctoral Thesis, California Institute of Technology, 1941.

61. K. Telegadas and J. London, "A Physical Model of the Northern Hemisphere Troposphere for Winter and Summer," *Scientific Report No. 1*, Contract AF19(122)–165, Research Div., College of Engineering, New York University, Feb. 1954, 55 pp.

62. E. Tønsberg and E. L. Olsen, "Investigations on Atmospheric Ozone at Nordlysobservatoriet, Tromsø," *Geofysiske Publikasjoner*, vol. 13, No. 12, 1943.

63. G. B. Tucker, "An Analysis of Humidity Measurements in the Upper Troposphere and Lower Stratosphere Over Southern England," *M.R.P. 1052*, S.C. III/235, Meteorological Research Committee, Air Ministry, England, 1957.

64. E. Vigroux, "Contributions a l'Etude Experimentale de l'Absorption de l'Ozone," *Annales de Physique*, vol. 8, 1953, pp. 709–762.

65. C. D. Walshaw, "Integrated Absorption by 9.6μ Band of Ozone." *Quarterly Journal of the Royal Meteorological Society*, vol. 83, No. 357, July 1957, pp. 315–321.

66. L. R. Weber and H. M. Randall, "The Absorption Spectrum of Water Vapor Beyond 10μ," *Physical Review*, vol. 40, 1932, pp. 835–847.

67. G. Yamamoto and G. Onishi, "Absorption Coefficient of Water Vapour in the Far Infrared Region," *Science Reports of the Tohoku University, Ser. 5, Geophysics*, vol. 1, No. 2, Nov. 1949, pp. 71–75.

68. G. Yamamoto, "On a Radiation Chart," *Science Reports of the Tohoku University, Ser. 5, Geophysics*, vol. 4, No. 1, June 1952, pp. 9–23.

69. G. Yamamoto and G. Onishi, "Absorption of Solar Radiation by Water Vapor in the Atmosphere," *Journal of Meteorology*, vol. 9, No. 6, Dec. 1952, pp. 415–421.

70. G. Yamamoto, "Radiative Equilibrium of Earth's Atmosphere. I. The Grey Case," *Scientific Reports of the Tohoku University, Ser. 5, Geophysics*, vol. 5, No. 2, Oct. 1953, pp. 45–57.

71. G. Yamamoto, "Radiative Equilibrium of the Earth's Atmosphere. II. The Use of Rosseland's and Chandrasekhar's Means in the Line Absorbing Case," *Scientific Reports of the Tohoku University, Ser. 5, Geophysics*, vol. 6, No. 3, June 1955, pp. 127–136.

THREE-DIMENSIONAL PRESSURE PATTERN OF THE DALLAS TORNADO AND SOME RESULTANT IMPLICATIONS

WALTER H. HOECKER, JR.

U.S. Weather Bureau, Washington, D.C.

[Manuscript received August 18, 1961]

ABSTRACT

The three-dimensional pressure field of the Dallas tornado, April 2, 1957, is integrated from a distribution of observed tangential wind speeds. A total pressure drop of 60 mb. is computed at ground level at the axis. Variations in tornado funnel geometry are explained by changes in moisture content of the involved air and system-wide pressure changes. The effects of the moving pressure field on hypothetical vented and unvented buildings are computed. The results indicate that a dwelling, which could lose in 5 seconds about 75 percent of an imposed pressure difference, would most likely not yield due to internal pressure alone, if the imposed pressure difference were like that of the Dallas tornado.

1. INTRODUCTION

In an earlier study [1] the tangential wind speed distribution of the Dallas tornado of April 2, 1957 was derived by tracking pieces of debris, cloud tags, and dust parcels that were photographed in movies of that tornado. Principles of photogrammetry [2] were used in scaling the movies from which these data were taken. In order to get the greatest possible coverage of data points in the space occupied by the tornado it was necessary to take speed measurements over 19 minutes of the tornado's lifetime. The data distribution extended to a height of 1700 feet and a radius of 1500 feet except below 1000 feet in elevation where traceable particles extended only to between 400 and 900 feet in radius. Using the tangential speed (v) distribution as analyzed in figure 2 of [1] and making use of the cyclostrophic wind equation,

$$\partial p/\partial r = \rho v^2/r \qquad (1)$$

(where p is pressure, r radial distance, and ρ density) a distribution of values of horizontal pressure gradient in terms of millibars per meter was obtained for every 100-foot level for the region occupied by the tornado described above. Of course, it is realized that some limitations are imposed by the assumption of cyclostrophic balance and steady state, especially in the inflow region near the ground; however, at present no reasonable allowance for resistance and accelerational forces has been developed for this situation. Other writers (e.g., Long [3], Glaser [4]) have justified the use of the cyclostrophic equation in their studies of vortex motion.

In that part of the material following which deals with vented and unvented structures, it is not implied that the pressure distribution arrived at and its implications are more important than the aspects of tornado wind force on structures. Rather, one side of the problem is presented, that is, the effects of variable rates of static pressure drop on structures.

2. THE DERIVED PRESSURE FIELD

The pressure field was derived by integrating equation (1) horizontally from the 1,500-foot radius, step-wise, to near the axis for each 100-foot level. For the boundary condition at the 1,500-foot radius, a vertical lapse rate of pressure computed from the pressure and temperature conditions at Dallas for the time of the tornado, was used. The resulting pressure distribution, delineated by isobars at every 5 mb., is shown as figure 1. In general the isobaric surfaces dip away from the horizontal going toward the axis.

One more assumption must be mentioned: in the region below the 400-foot level, any computed distribution of pressure values that tended to inflect the tornado's isobaric surfaces toward the axis was shifted outward enough to keep the sign of curvature yet conserve the horizontal rate of change of pressure. The earlier-derived distribution of tangential speeds would have caused a bending toward the axis of the pressure surfaces below 400 feet but because the observed speeds must have been retarded by frictional drag of the ground, it was reasoned that the region of steep pressure gradient continued down to the ground without inflection. Of course, at very small radii, the isobaric surfaces must have curved toward the axis because of the reduced tangential speed there.

The total pressure drop at the ground estimated by this method was almost 60 mb., or just under 6 percent of an atmosphere. One might add 2 or 3 mb. if the pressure reference were taken entirely away from the influence of the tornado, for example, two or three miles. Since most of the wind speed values from which the pressure change computations were made were derived during an immature

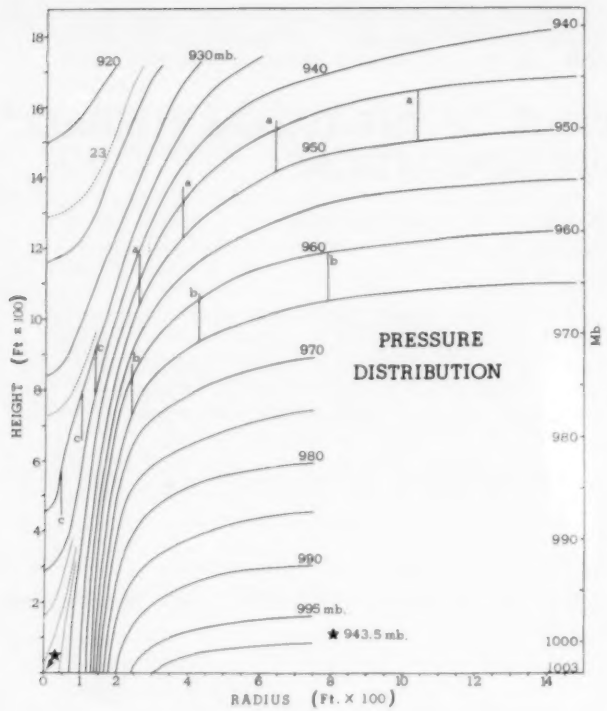

FIGURE 1.—The derived pressure field of the Dallas tornado in the vertical plane. Symmetry in the horizontal plane is assumed, giving pressure distribution in three dimensions. The derived central pressure at the ground is 943.5 mb., or 59.5 mb. below the undisturbed pressure of 1003.0 mb.

stage of the tornado, that is, when the tip was suspended aloft, it is suspected that the total pressure drop computed here was exceeded at a later stage of the tornado's development.

3. IMPLICATIONS OF THE PRESSURE FIELD

As can be seen in figure 1, the pressure surfaces slope downward gently at the larger radii, then curve more steeply at smaller radii. A particularly interesting feature of the pressure field is that the vertical spacing of the pressure surfaces decreases with decreasing radius to a certain limiting radius. The vertical bars a and b show this feature rather clearly since each set has the same length. If one can safely assume that the vertical spacing at the 1,500-foot radius represents hydrostatic equilibrium, then the closer vertical spacing at smaller radii indicates the presence of a net upward force. This interpretation is valid as long as increased density does not overcome the upward force indicated by the closer spacing, but considering the 60-mb. pressure drop at the axis, it is unlikely that the density is higher there. This closer vertical spacing is to be expected in the tornado where upward current speeds are greatest nearer the center and where upward accelerations are occurring. At the smaller radii, such as at the inward-most position of the vertical bar a, the vertical pressure gradient is twice that at the 1,500-foot radius, indicating an excess upward force equal to gravity.

In the core region, closer yet to the axis, the trend is the opposite; that is, the vertical spacing between the pressure surfaces increases with decreasing radius indicating a lessening of the upward pressure force. This trend is illustrated by the vertical bars labeled c, all of which are the same length. This result corresponds with earlier findings [1] where upward current speed in the core region decreased with increasing altitudes above a certain level and there was an envelope of zero upward speed in near coincidence with the visible funnel cloud. And, as figure 1 indicates, the vertical pressure difference between the ground and 1,450 feet at the 1,500-foot radius is 51 mb. compared with only 23.5 mb. at the axis, a ratio of greater than 2 to 1. Using the assumption of vertical equilibrium at the 1,500-foot radius, the average upward force on the air at the axis between the ground and the 1,450-foot level is less than half that at the 1,500-foot radius, resulting in a net downward force there. Just the geometry of the situation indicates that if some of the isobaric surfaces intersect the ground while at some higher elevation they are level again, the vertical spacing between them over the region where they intersect the gound must be greater on the average than at some undisturbed region. The net downward force on the air in the core region of the tornado could mean a downdraft in some extent of the core, somewhat as shown by Ward's [5] model air vortex, or, more specifically, a downdraft inside of an updraft.

Figure 2 shows two alternative schemes of vertical air flow suggested by the isobaric analysis of figure 1 and by analyzing debris and cloud element movements in tornado movies and debris distributions in still pictures. It is suggested here that the core air acted on by a net downward force is at times frictionally supported above the ground by the upward jet as in figure 2a, or, occasionally not quite supported as in figure 2b; the latter would account for the wide trunk-type funnel sometimes seen touching the ground. Movies and still photographs of tornadoes have shown a clear region extending all the way to the ground from the bottom of the wide but suspended and chopped-off funnel, even though debris was being stirred up in the shape of a ring whose diameter is a little larger than the diameter of the chopped-off funnel. This could only happen when no air was flowing into the axis near the ground and would most likely happen with a downward flow diverging at the ground and keeping debris away from the axis.

The idea of a central downdraft is, of course, not new; Rossmann [6], Gutman [7], and Kuo [8] have all shown various theoretical systems of downdraft inside vortices. What is new here is the observation via movies of the lack of updraft along portions of the tornado trunk and in-

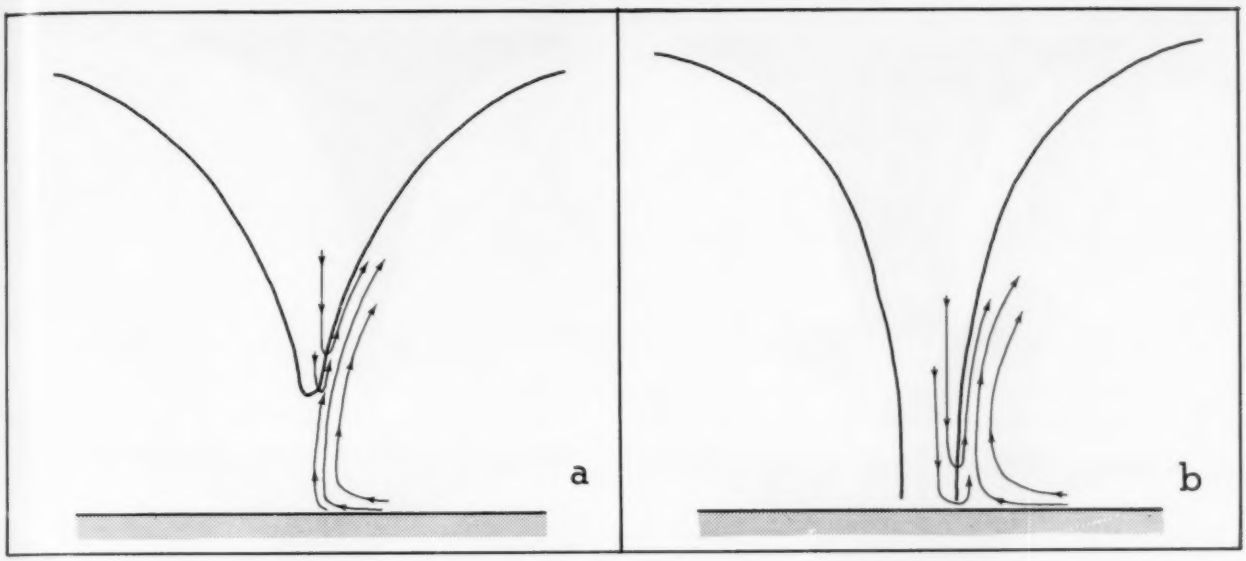

FIGURE 2.—Schematic air flow of the tornado in the radius-height plane as suggested by the results of figure 1 and the study of movies and still photographs taken of tornadoes. (a) Funnel aloft; (b) funnel reaching ground.

direct evidence of a downdraft from tornado still photographs.

4. POSSIBLE REASONS FOR TORNADO GEOMETRY BEHAVIOR

Almost everyone is familiar with the various shapes that a tornado takes on, such as the suspended funnel, the rope-type, and the elephant-trunk-type funnel. Some of these differences in the shape and size of the tornado could be explained from the pressure profiles of figure 1 by assuming that the visible tornado surface lies along an isobar, and by varying the moisture content of the air involved in the tornado system. If the condensation pressure is specified to be 930 mb., the shape of the funnel would be that of the shaded portion of figure 3a, which is very much like some funnels aloft. If the condensation pressure is increased to 940 mb. the profile becomes like the shaded portion of figure 3b, which is still a suspended funnel but with the tip considerably lower. In figure 3c the condensation pressure is increased by only 5 mb. to 945 mb. and the tornado becomes a mature-appearing elephant-trunk type. For these small condensation pressure changes, the greatest dimensional change is in the tip height. For example, for the 10-mb. change from 930 to 940 mb. the tip drops 550 feet while the funnel cloud height at the 1,500-foot radius drops only about 125 feet. For situations with more steeply sloped and more tightly packed isobaric systems the tip movement would be even greater for the same change in condensation pressure. Between pressures of 945 and 975 mb. the trunk diameter for this tornado would become quite insensitive to condensation pressure changes because of the tight horizontal packing of the pressure surfaces. However, relatively large changes would result in the diameter near the top of the funnel and in the height of the funnel at large radii for a given condensation pressure change.

At the time of the tornado, the condensation pressure at the Dallas Weather Bureau station was about 950 mb. This would require, with the pressure system of figure 1, a trunk diameter of 200 feet at the ground, yet the maximum diameter photographed was about 110 feet.

It is easily seen how the profile of the tornado can be changed rather drastically with only a little change in the water content of the air involved in the vortex. A similar type of profile change would result if the entire system-wide pressure of the tornado changed but the spacing and shape of the isobars and water content were conserved. Again it must be assumed that the visible tornado surface lies along an isobaric surface. It would seem that in the weaker stage of the tornado only slight changes in system-wide pressure or moisture would cause the tip height to change rapidly, while in the elephant-trunk stage, taken to be a mature or powerful stage, large changes in system pressure or moisture content would make little change in funnel diameter and no change in tip height, but would make moderate changes in the height of the visible funnel surface at the larger radii and higher elevations. In the latter stage the tornado trunk is in a relatively stable condition. Observations by means of movies confirm that in the immature stage the tip does rise and dip rapidly and trunk diameter fluctuates; but once the trunk touches the ground and assumes the elephant-trunk

616949—61——5

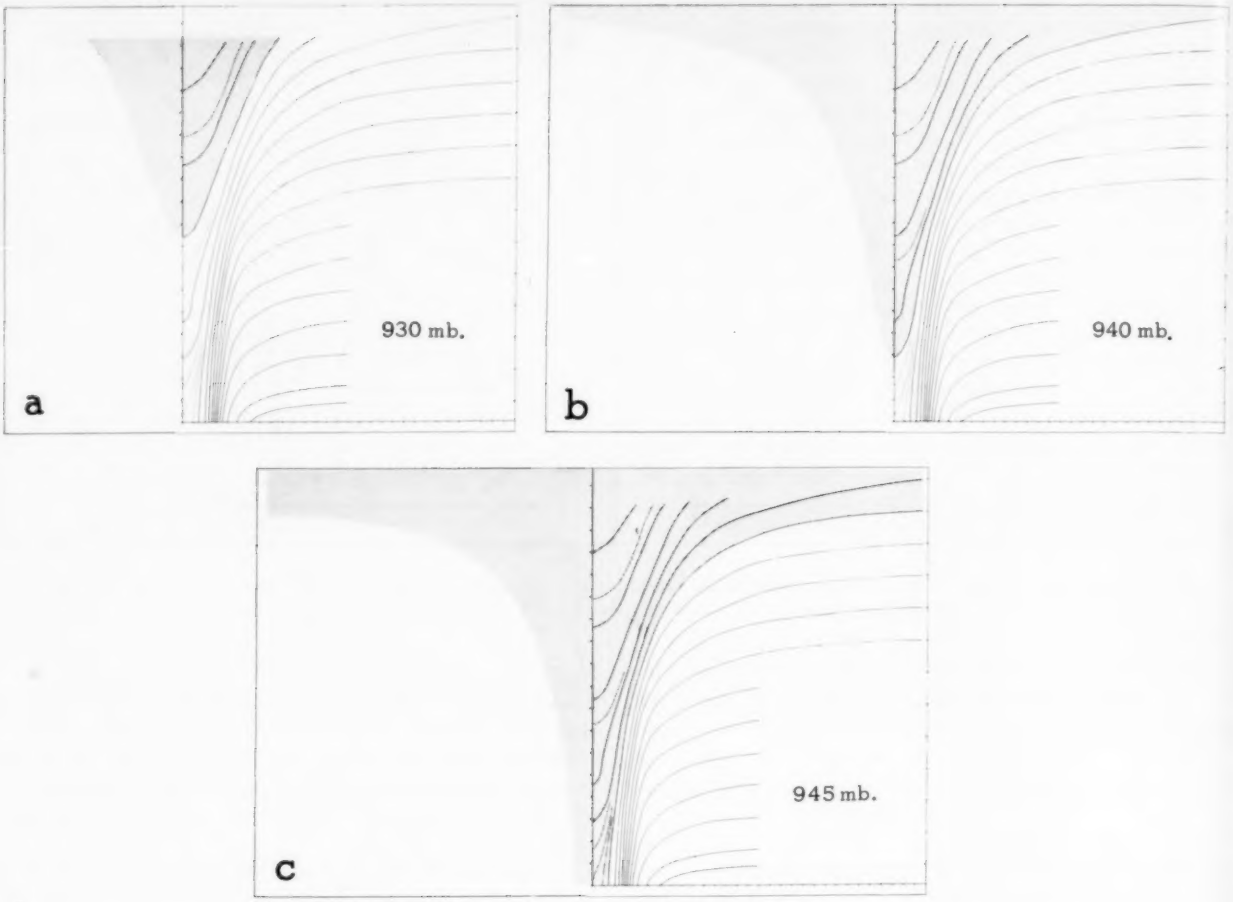

FIGURE 3.—Tornado funnel shapes for condensation pressures of (a) 930 mb., (b) 940 mb., and (c) 945 mb. for the Dallas tornado. Dimensional changes of the funnel are sensitive to condensation pressure change in the range from about 930 to 940 mb. and insensitive from about 945 mb. higher.

shape, rapid changes in trunk diameter no longer take place.

Additionally, shape changes could be effected if the system of isobars moved outward as a body. This would involve little additional central pressure drop since the radial rate of change of pressure near the axis at the ground is small, at least for this tornado. The result would be the wide, ominous-appearing tornado sometimes photographed and regarded as being particularly destructive. Likewise, if the system of isobars retaining the initial geometrical shape was crowded toward the center, with the water content conserved, the tornado would become tall and narrow, a rather frequent type of tornado that is photographed. In figure 4 are shown narrowed and widened tornadoes using the pressure surfaces from figure 1. In figure 4a and b the 940-mb. surface was used to provide suspended narrow and wide funnels respectively, and in figure 4c and d the 945-mb. surface was used to provide narrow and wide ground-based funnels. Just what mechanism could effect such changes is not known but if the core of air excluded from the sink (observed in movies of the Dallas tornado and of the Scottsbluff tornado of June 27, 1955) were expanded or contracted in volume, it could cause the effects shown in figure 4. As an example figure 5 shows a series of photographs of the Wichita Falls, Tex. tornado of April 2, 1958, in the process of expanding. Note that the debris pattern in figure 5e is more dense along the outer edges but that it is clearer in the center beneath the truncated funnel. This arrangement can only indicate a shell-like dust pattern with a clear or clearer core. It is suggested that air converging toward the tornado, near the ground, turns upward in a shell whose diameter is nearly equal to that of the bottom of the funnel. This current carries the light debris upward around the edges and descending air (possibly descending slowly) from the tornado core assists in pushing aside the

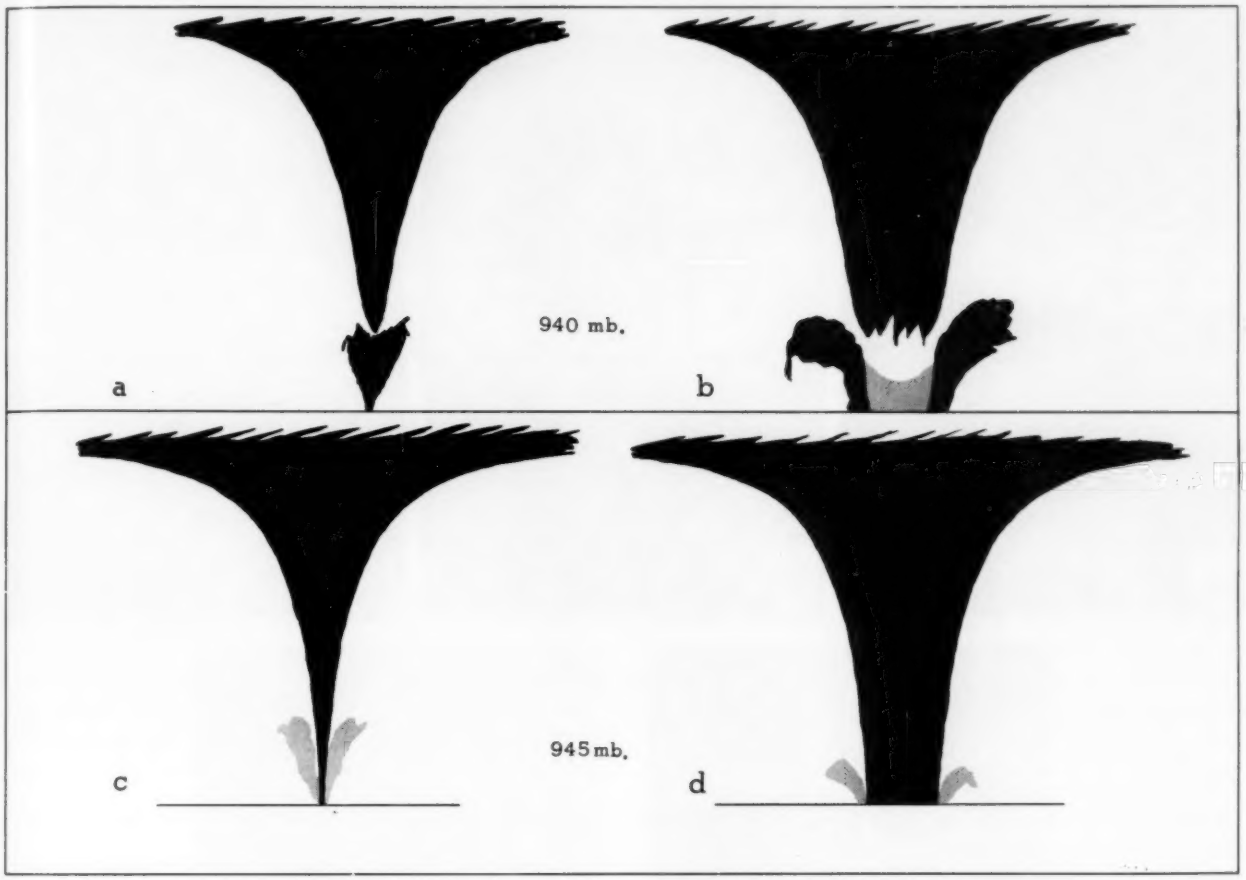

FIGURE 4.—The effect on funnel size of widening or narrowing the pressure field of the Dallas tornado using the pressure pattern of figure 1 and conserving the condensation pressure. (a) Narrow funnel and (b) wide funnel at 940-mb. condensation pressure. (c) Narrow funnel and (d) wide funnel at 945-mb. condensation pressure. The four profile types shown here are often photographed.

debris-carrying upward current. Ward's model [5] air vortex shows downdrafts under certain conditions.

5. THE MOVING PRESSURE FIELD

Some interesting local pressure change variations result from translating the surface pressure field at 27 m.p.h., the average speed of the Dallas tornado. Figure 6 shows the rate of change of pressure at a point directly on the tornado path. In the computation finite differences were used, then center points were connected by a smooth curve. The starting point, zero seconds, is at the 1,500-foot radius, a distance from the tornado center at which little time-rate of pressure drop is encountered. For the first 19 seconds the rate of pressure drop averages about 0.1 mb. per second. Between 19 and 30 seconds it averages about 0.3 mb. per second. After the 30th second the pressure falls rapidly and by the middle of the 33d second reaches a peak rate of 26 mb. per second. The rate of pressure fall decreases rapidly after the 33d second and returns to zero at the center of the tornado. As the tornado moves onward the sequence occurs in reverse order, assuming that the pressure field is symmetrical.

Much of the tornado damage described in the literature is attributed to the external pressure drop caused by the pressure field of the tornado. This assumes, of course, that the structures withstood the excessive wind speed experienced up to the time of the yield caused by excess pressure trapped in the structure. The rapid rate of change of surface pressure described above has applications to structures relative to the possible explosive force caused by the sudden external pressure drop. Now for the first time the effect on a structure can be quantitatively estimated since the pressure field presented here is in the nature of an observation, although an indirect one. An airtight structure is assumed in the following discussion.

Referring to figure 6 it is seen that the maximum rate of pressure increase (inside of a structure) of 26 mb. per second occurs over a period of 0.5 second. This computes

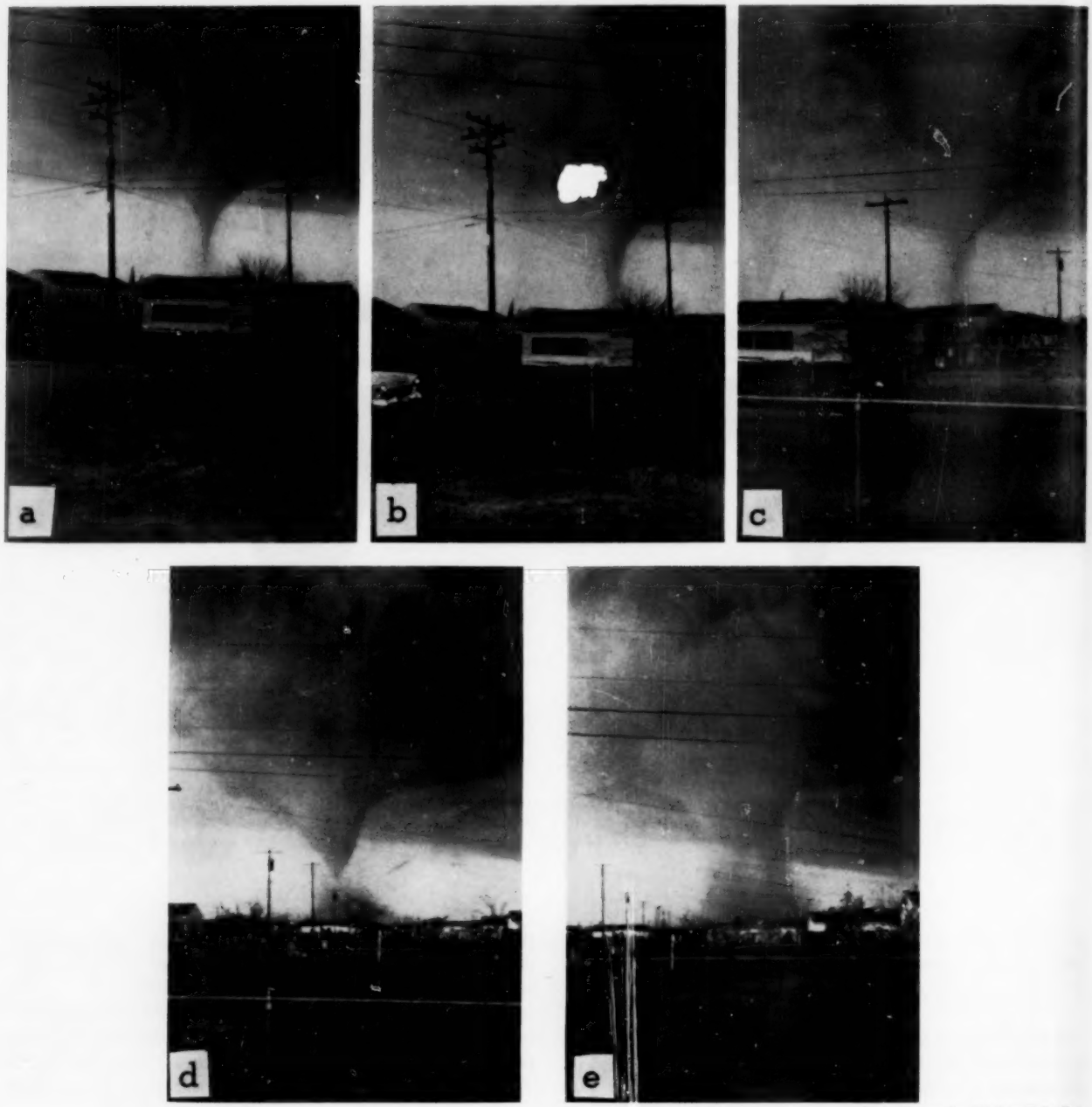

Blake Allison, Jr., Wichita Falls, Tex.

FIGURE 5.—Photographic time sequence, (a) through (e), of the Wichita Falls, Tex., tornado of April 2, 1958, in the process of expanding radially. Note that the debris cloud near the ground expands from (d) to (e) at the same time and that the debris density in (e) is greatest along the outer edges.

to 26 pounds force per square foot increase in 0.5 second, and for a hypothetical 8 x 15-foot wall, 3,100 pounds increase in force in 0.5 second. And this is at the end of a period of additional rapid force increase.

To illustrate the total static pressure fluctuation at the ground along the tornado's path and adjacent to it (and total force on the hypothetical 8 x 15-foot wall), figure 7 was constructed. At the bottom is the time scale for 27 m.p.h., at the top is the equivalent distance scale along the tornado path, at the left is the percent of total pressure drop and at the right are scales of total pressure force on the wall and force per foot of perimeter. The left curve is the pressure variation along the path, the middle curve is that 100 feet from the path, and the right curve is the pressure variation for a location 150 feet from the path. The curves represent the pressure difference between an undisturbed region and any point within the tornado pressure field. Due to the crowding of the isobars between 100- and 150-foot radius, there is only 13 percent less final static pressure drop at a point 100 feet away from the center than is found directly on the path. However, the final pressure drop 150 feet away is 50 percent of the final on-path pressure drop.

Two analytical expressions were used to approximate the pressure-time profile of this tornado at the surface; one was for the 1500 to 300-foot radial distances (37.9 to 7.6 sec.) and the other for the remainder of the distance to the minimum pressure axis. These were:

$$p=1-\exp\ (-0.755/\ |t|),\ 7.6\ \text{sec.} \leq |t| \leq 37.9\ \text{sec.} \quad (2)$$

$$p=1-\exp\ (-48.3/\ |t^3|),\ |t| < 7.6\ \text{sec.} \quad (3)$$

in which the reverse time equivalent of distance was used, that is, time decreased to zero at the axis in making the computations. In both cases the curves were forced to pass through the observed point at 300-foot radial distance (7.6 sec.).

The fit of these analytical expressions is shown in figure 7 and is possibly better for the one covering the range of larger radii. The break in curvature at about the 300-foot radius reflects the sudden change in shear of the tangential wind speed found in an earlier work [1] and, of course is reflected in the balanced pressure field distribution. In the figure the x's are points computed from equation (2) and the +'s are points from equation (3).

Returning to the idea of the effect of the tornado pressure drop on a structure such as a dwelling, the author has been impressed by photographs of dwellings[1] with one wall popped off allegedly as a result of tornado proximity, and photos showing the common wall of a series of row houses or apartments removed intact leaving the rooms open to view and otherwise relatively undisturbed. Accordingly the scales at the right-hand side of figure 7

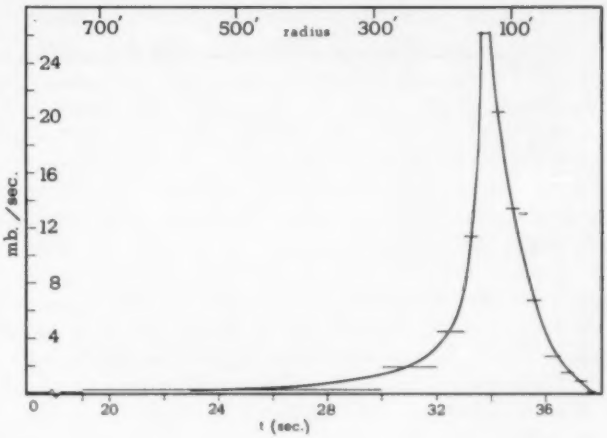

FIGURE 6.—The rate of change of surface pressure in mb. per sec. along the path of the Dallas tornado. The tornado axis is at the right.

have been computed to indicate the force on an 8 x 15-foot wall of a dwelling in the direct path, 100 feet away, or 150 feet away from the tornado. The force in pounds for any distance from the tornado center or position of nearest approach is given directly for all these paths. Another scale at the right shows the force per linear foot of the perimeter of the stated hypothetical wall. Note the tremendous force on the wall at the point of total pressure drop; it amounts to 7.5 tons and 85 percent of this force was applied in 5 seconds (in the Dallas tornado). For the house 150 feet away from the tornado path 7,500 lb. are applied at the point of nearest proximity of the tornado, or only about 50 percent of that for the structure directly on the path.

Now, suppose that the wall in question were nailed around its perimeter with two 20-penny nails per foot of perimeter. The pulling strength of a 20-penny nail was quoted as 70 lb. [10]. So for this hypothetical wall a force of 140 lb. per foot of perimeter would cause it to yield, theoretically. The yield point of this wall is shown at the solid black triangle opposite the last scale on the right of figure 7. The force on the wall for structures directly on the path as well as those 100 feet away greatly exceeds the yield point of this hypothetical wall. However, the wall for the dwelling 150 feet away at closest approach has nearly enough strength to resist the force of pressure drop; moreover, there the force is applied at a slower rate. A dwelling 175 feet from this tornado would encounter only 33 percent of the total pressure drop (100 lb./ft.) and so would not encounter the yield force.

Of course, no dwelling is airtight by the nature of the usual construction practices, and many dwellings are required by building codes to have attic vents at least. Such designed and inadvertent vents could prevent the

[1] Some examples are shown by Reynolds [9].

616949—61——6

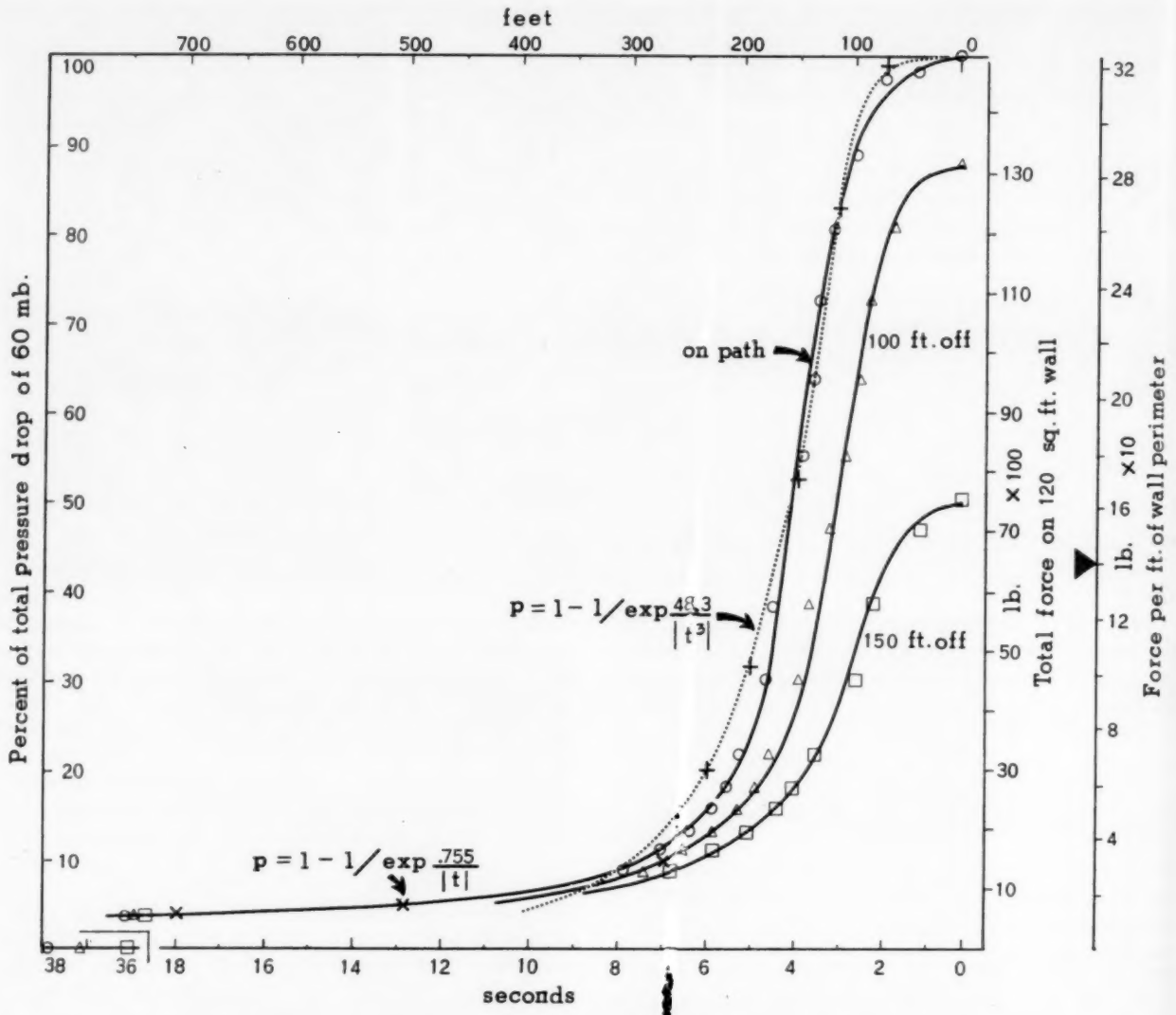

FIGURE 7.—Time (distance) variation of the Dallas tornado surface pressure drop "on" and "off" the tornado path in terms of percent of total pressure drop and force on hypothetical wall. An estimated yield point for the wall is indicated by the solid triangle on the right-hand scale.

build-up of certain amounts of excess pressure in dwellings, but just how much has always been the critical question. The answer depends upon the rate of drop of the environmental pressure at the building and the rate at which excess internal pressure could escape. Reynolds [9] has long been a strong advocate for installation of vents in dwellings for the purpose of releasing excess internal pressure that could result from the near approach of the tornado.

Having the time-rate of pressure change of the Dallas tornado, the effect of the pressure change on a hypothetical dwelling with a vent was examined. Pressure was to bleed off exponentially at a rate that would remove nearly 75 percent of any imposed excess pressure in 5 seconds. The expression for the bleed or decay function was:

$$R = R_0 \exp(-at) \tag{4}$$

where R = residual pressure difference and R_0 = initial imposed pressure difference. The computation was handled stepwise, as explained in the appendix, and was made only for the on-path case since it was found that the maximum accumulated pressure did not exceed the yield point of the hypothetical wall discussed earlier. The

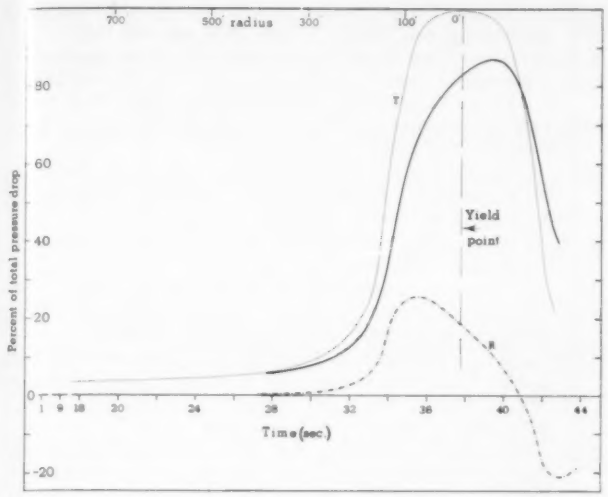

FIGURE 8.—Time variation of residual pressure difference between environment and interior of vented hypothetical dwelling (the dot-dash curve, R). The environmental pressure (tornado pressure) is shown by the dotted curve (T) and the solid curve represents the internal pressure of the vented dwelling relative to an undisturbed atmosphere.

results are shown in figure 8 where part of the pressure effects for the retreating side of the tornado are also shown. Here the dotted line labeled "T" is the on-path pressure-time (distance) curve of figure 7 or the pressure drop in the tornado compared to the undisturbed region, the solid line is the pressure in the dwelling compared to the undisturbed region, and the dot-dash curve marked "R" is the residual pressure, relative to the tornado, in the dwelling. The arrow marks the yield point of the hypothetical wall and it is noted that the maximum of the residual pressure curve falls below the yield point. The residual pressure relative to the tornado is virtually zero up to 30 seconds elapsed time, or 8 sec. before the axis of the tornado arrives. It rises sharply from 33.5 to 34.5 sec. then falls from 36 to 42 sec. These results appear to show a definite value in adequate venting. Of interest is the fact that the maximum residual pressure in the house is reached 2⅓ sec. before the axis of the tornado reaches the dwelling. The rate of external pressure drop decreases at that time so the bleed is able to prevent the yield pressure from being reached. Also of interest is the fact that the internal pressure in the dwelling is equalized relative to the tornado 3 sec. after the axis of the tornado passes, then actually becomes less than that of the tornado so that there is an inward force on the dwelling. Then 5 sec. after the tornado passes the internal pressure again starts to equalize as shown by the minimum point of the R curve. The solid curve also represents the time-lag of pressure drop, relative to an undisturbed environment, incurred by the interior of the house.

6. CONCLUDING REMARKS

For the first time tornado pressure data in the nature of an observation, although indirectly derived, have been used as a possible explanation for the changing shapes and sizes of tornado funnel clouds, for non-typical conceptions of tornado air flow, and for effects on airtight and vented hypothetical dwellings. It is realized that many factors have not been considered, such as the dynamic effects of the strong winds of the tornado that are felt about the same time as the pressure drop, and which might even neutralize some of the static pressure drop effects. The situation is not a simple one, but the first approach is better understood with a simple application. It is hoped that more usable data of this nature will become available so that they may be compared with the material presented here.

APPENDIX

METHOD OF COMPUTATION OF RESIDUAL PRESSURE VARIATION IN VENTED ENCLOSURES

The stepwise method of treating the pressure variations in vented enclosures was used here as an easy means of obtaining a reasonable estimation of the result wanted. Of course, such problems can be treated analytically when the imposed pressure variation is sinusoidal, a ramp or a step function, but the pressure-time variation imposed by the Dallas tornado was none of these. Accordingly, the stepwise method was used as described below.

The exponential decay function given by equation (4) was employed in the form:

$$R_1 = R_0 \exp(-a\,\Delta\,t)$$

where R_1 is the residual pressure difference after a time interval Δt, R_0 is the total pressure difference at the initial time for each step, a is the coefficient that controls the

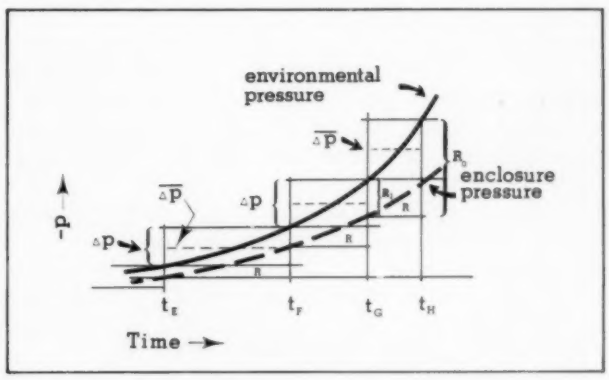

FIGURE 9.—Schematic illustration of stepwise method of computing pressure variation in a vented enclosure. The residual pressure difference, R, is added to the average of the externally-imposed pressure difference (Δp) used for the next time interval.

rate at which the imposed pressure difference is to be bled off, and Δt is the time difference in seconds. About 75 percent of any imposed stepwise pressure difference would be bled off in 5 sec. for $a=0.25$, which was used in the computations described previously.

Although pressure differences were treated as step functions in the above equation, the approximate average of the pressure difference was used for R_0 since the pressure actually changed over a finite time period. The residual pressure difference, R_1, was added to the average pressure step used for the next succeeding interval. The method is illustrated graphically in figure 9.

ACKNOWLEDGMENT

Permission was kindly granted by Blake Allison, Jr. of Wichita Falls, Texas, to use his photographs of the Wichita Falls, Texas, tornado of April 2, 1958, in this paper.

REFERENCES

1. W. H. Hoecker, "Wind Speed and Air Flow Patterns in the Dallas Tornado of April 2, 1957," *Monthly Weather Review*, vol. 88, No. 5, May 1960, pp. 167–180.
2. *Handbook of Photogrammetry*, American Society of Photogrammetry, 1952.
3. R. R. Long, "Vortex Motion in a Viscous Fluid," *Journal of Meteorology*, vol. 15, No. 1, Feb. 1958, pp. 108–112.
4. A. H. Glaser, "An Observational Deduction of the Structure of a Tornado Vortex," in *Cumulus Dynamics* (Proceedings of the First Conference on Cumulus Convection, May 19–22, 1959), C. E. Anderson (Ed.), Pergamon Press, New York, 1960, pp. 157–166.
5. N. B. Ward, "Temperature Inversion as a Factor in Formation of Tornadoes," *Bulletin of the American Meteorological Society*, vol. 37, No. 4, Apr. 1956, pp. 145–151.
6. F. O. Rossmann, "On the Physics of Tornado Processes," Alamogordo, N. Mex., Dec. 1958.
7. L. N. Gutman, "Theoretical Model of a Waterspout," [Teoreticheskaĭa Model Smercha] *Izvestiĭa*, Akademiĭa Nauk, SSSR, Seriĭa Geofizicheska, No. 1, 1957, pp. 79–93.
8. H. L. Kuo, "Dynamics of Convective Vortices and Eye Formation," pp. 413–424 of *The Atmosphere and the Sea in Motion*, Rossby Memorial Volume (B. Bolin, Ed.), Rockefeller Institute Press, New York, 1959.
9. G. W. Reynolds, "Venting and Other Building Practices as Practical Means of Reducing Damage from Tornado Low Pressures," *Bulletin of the American Meteorological Society*, vol. 39, No. 1, Jan. 1958, pp. 14–20.
10. E. P. Segner, Jr., "Calculations of Minimum Wind Velocity Causing Structural Damage in the Dallas Tornado," *The Dallas Tornado of 2 April 1957*, Tornado Damage Surveys, *Raw Data Report No. 2*, The A. and M. College of Texas, Department of Oceanography and Meteorology, College Station, Tex., August 1957.

SUNSHINE-CLOUDINESS RELATIONSHIPS IN THE UNITED STATES

ROY L. FOX

Weather Bureau Regional Administrative Office, Kansas City, Mo.

Manuscript received June 15, 1960; revised September 27, 1961]

ABSTRACT

The statistical treatment of areal and seasonal groupings of mean annual and mean monthly percentage sunshine and percentage cloudiness data for United States stations based on relative amounts of stratiform cloudiness yields interesting and useful results. These results are readily apparent in charts which have been developed to depict the regression lines, errors of estimate, and coefficients of correlation, and which are included in this article. For example, the charts reveal that the regression line for the relatively low percentage sunshine months for the areas of the country with high amounts of stratiform cloudiness is well displaced from that for the relatively low percentage sunshine months for areas with comparatively low amounts of stratiform cloudiness.

1. INTRODUCTION

The amount and nature of the cloudiness prevailing at a location within any interval or the whole of the period of the day between sunrise and sunset are primary factors in determining the percentage of possible sunshine received. Since records of the observed amounts and nature of cloudiness and their monthly and annual mean values are available for many more localities than are records of percentage of possible sunshine, reliable formulae for expressing the latter in terms of the amount and nature of cloudiness are useful in climatological work. However, few results of studies to relate both the amount and nature of the cloudiness prevailing over large areas to the percentage of possible sunshine received appear to be available.

The maps for average annual number of days with dense fog, percentage of possible sunshine winter and summer, and average number of cloudy days per year appearing in [1] depict information which, when compared, reveal the interrelation of sunshine and the amount and the nature of cloudiness in a general fashion. These show that the regions in the contiguous United States having low percentages of possible sunshine (namely, the narrow band along the North Pacific coast, the Great Lakes region, and the large area to the east and northeast of the Gulf of Mexico) have a high incidence of cloudy days and days with fog. They also reveal, conversely, that the regions with high percentages of possible sunshine (the area from the Coastal Ranges of the west eastward into western and northern Texas, Arkansas, and the middle and upper Mississippi Valley) in general experience a lower incidence of cloudy days and days with fog.

Byers [2] has pointed out that, except for points at higher mountain elevations, fog is really a stratus cloud cover at or close to the ground. It does not necessarily follow that each weather station away from mountaintops having a high incidence of foggy days also reports more stratiform cloudiness than does every station having a low number of foggy days in the year. However, most weather stations in the more foggy regions of the contiguous United States report more stratiform cloudiness than do those in the less foggy ones. Thus, it may be broadly stated that the narrow strip of land between the Pacific Ocean and the western Coastal Ranges, the Great Lakes region, and the area to the east and northeast of the Gulf of Mexico are characterized by more stratiform cloudiness than are the other areas in this part of the globe.

Landsberg [3] points out that the percentage of sunshine plus the percentage of cloudiness equals 100 as a first approximation. Some studies, both for points in the United States and elsewhere, have been made to determine this relationship more precisely. However, except for the reports by Sternes [4] [5], there is no record of a comprehensive study of this relationship for the United States using recent data.

The table of normals, means, and extremes for some United States localities [6] provides recent "period of record" data for mean monthly and annual percentages of possible sunshine and mean monthly and annual sky cover sunrise to sunset. These cloudiness values may be expressed in percentages and readily compared with percentage of possible sunshine values to determine their interrelation. Though most of the localities for which these data are prepared do provide mean sky cover values, many do not maintain records of percentage of possible sunshine or have these records only for extremely short periods. Only 132 weather stations reported "period of record" values for both percentage of possible sunshine and mean sky cover sunrise to sunset for at least 12 years in their 1958 annual issue [6]. These were selected for this study. The percentage cloudiness data

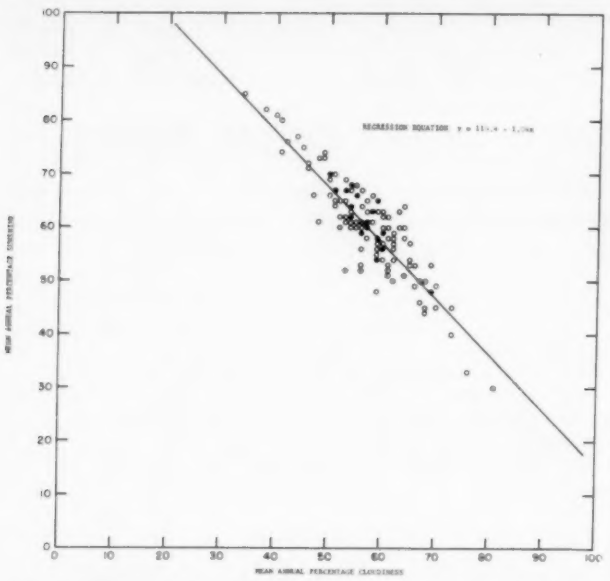

FIGURE 1.—Mean annual percentage cloudiness vs. mean annual percentage sunshine for 132 stations in the contiguous United States and Alaska. See figure 2 for locations. Filled circles represent data for more than one station.

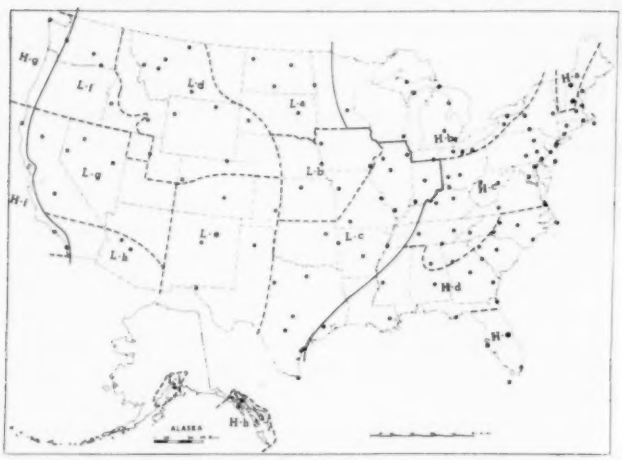

FIGURE 2.—Areas of the country with relatively high (H) and relatively low (L) amounts of stratiform cloudiness and sub-areas within which stations tend to have the same months of the year with relatively high, relatively low, and near average mean monthly percentage sunshine with respect to mean monthly percentage cloudiness. See table 1 for grouping of months for the sub-areas.

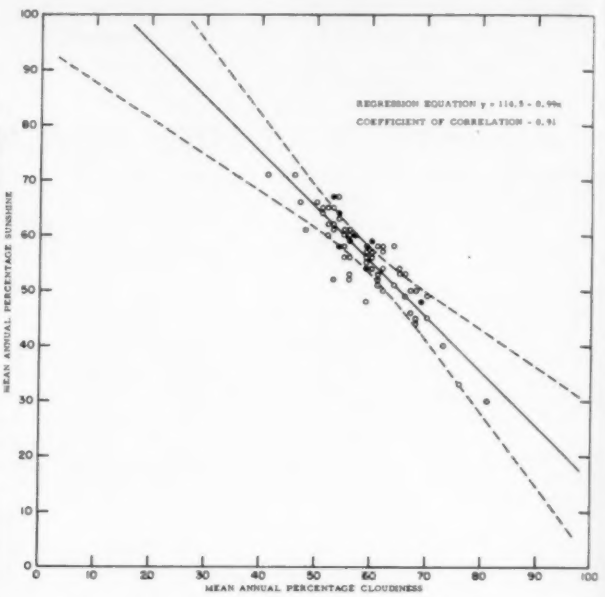
REGRESSION EQUATION y = 114.5 - 0.99x
COEFFICIENT OF CORRELATION = 0.91
MEAN ANNUAL PERCENTAGE SUNSHINE
MEAN ANNUAL PERCENTAGE CLOUDINESS

FIGURE 3.—Mean annual percentage cloudiness vs. mean annual percentage sunshine for 75 stations with relatively high amounts of stratiform cloudiness. Filled circles represent data for more than one station. Dashed lines delineate area within which the true regression line lies, for odds of 95 to 5.

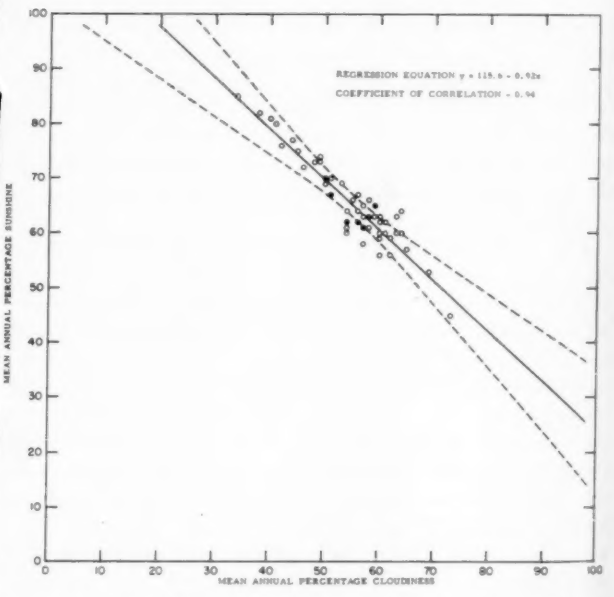
REGRESSION EQUATION y = 115.6 - 0.92x
COEFFICIENT OF CORRELATION = 0.94
MEAN ANNUAL PERCENTAGE SUNSHINE
MEAN ANNUAL PERCENTAGE CLOUDINESS

FIGURE 4.—Mean annual percentage cloudiness vs. mean annual percentage sunshine for 57 stations with relatively low amounts of stratiform cloudiness. See legend to figure 3.

were converted from their values for mean sky cover reported to tenths.

Examination of the annual values for these 132 stations indicated that Sternes' regression line for the annual data underestimated most of the values for the stations in the portions of the country with generally less cloudiness and/or lesser amounts of dense cloudiness, and that his regression line tended to overestimate values for stations in the more humid, cloudier portions of the country. This suggested not only developing regression equations by geographic areas for the mean annual data based

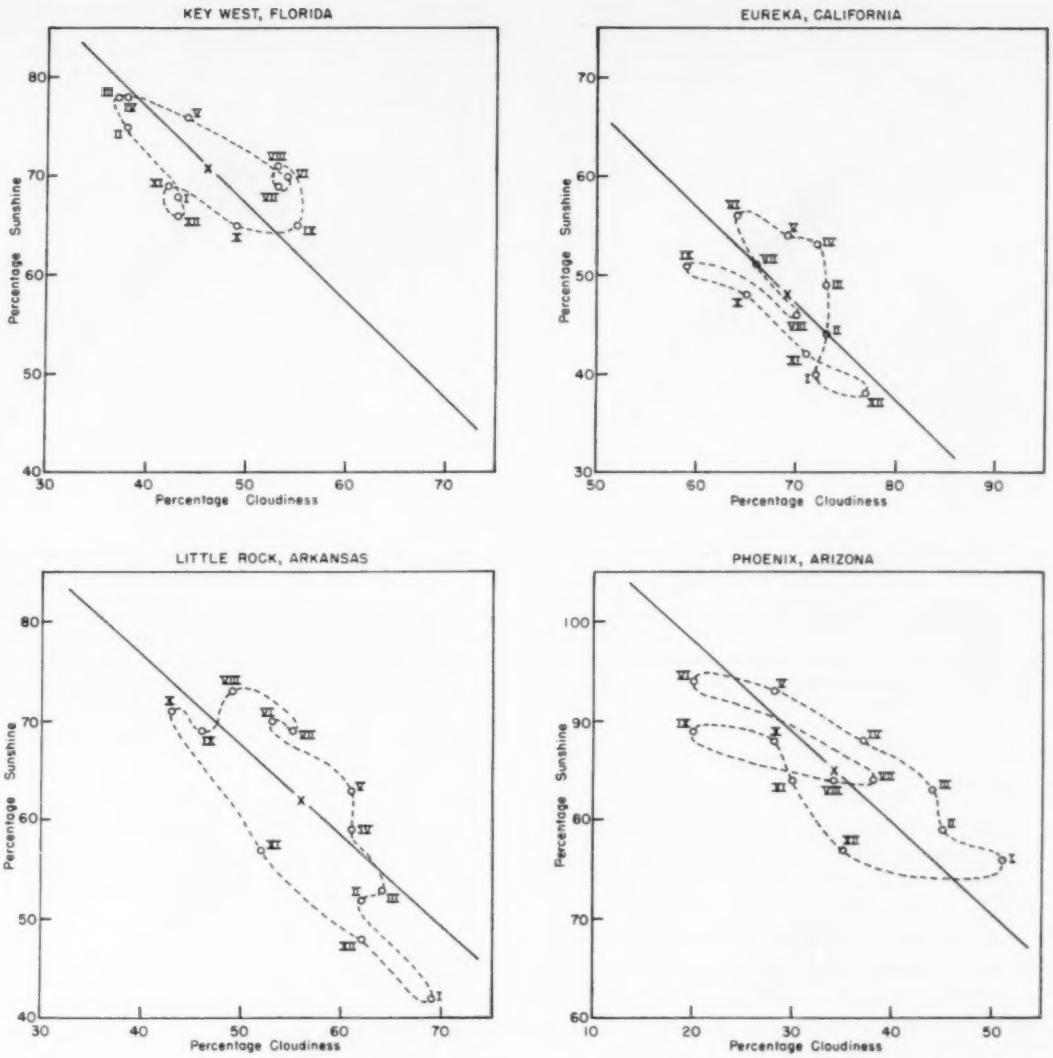

FIGURE 5.—Climographs for mean monthly percentage cloudiness vs. mean monthly percentage sunshine for 2 stations (top) in areas with relatively high amounts of stratiform cloudiness and 2 stations (bottom) in areas with relatively low amounts of stratiform cloudiness. Point indicated by x shows mean annual value and solid line is parallel to the regression line for all stations in that particular type of area. See figures 3 and 4.

on general density of cloudiness considerations, but also grouping the months of the year on the basis of cloudiness and/or density of cloudiness for determining shorter-period relationships. This is the course taken in this study.

2. ANNUAL DATA RELATIONSHIPS

The mean annual percentage sunshine and the mean annual percentage cloudiness for the 132 United States stations were studied to determine their relationship. The plot of these values appearing in figure 1 shows that the equation, percentage sunshine plus percentage cloudiness equals 119, gives a fairly close approximation. However, there is considerable scatter about the regression line determined from these data.

Grouping on a basis of amounts of dense cloudiness with the country divided as shown by the solid lines in figure 2, resulted in data for 57 stations being available for studying the sunshine-cloudiness relationship for the portion of the country with relatively low amounts of stratiform (dense) clouds. Data for the remaining 75 stations were then used for studying this relationship for the parts of the country characterized, in general, by having more stratiform (dense) cloudiness.

Figures 3 and 4 show this relationship for the two sets

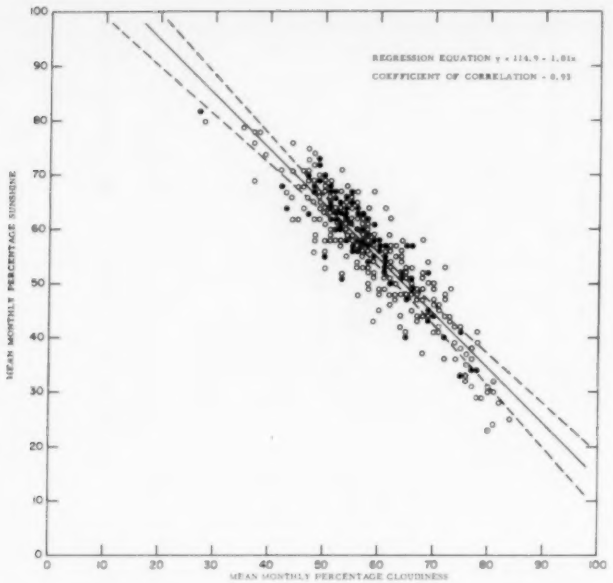
REGRESSION EQUATION y = 114.9 - 1.01x
COEFFICIENT OF CORRELATION = 0.93
MEAN MONTHLY PERCENTAGE SUNSHINE
MEAN MONTHLY PERCENTAGE CLOUDINESS

FIGURE 6.—Mean monthly percentage cloudiness vs. mean monthly percentage sunshine for the cases for the areas with relatively high amounts of stratiform cloudiness in which the sunshine is near average with respect to the cloudiness. See legend to figure 3.

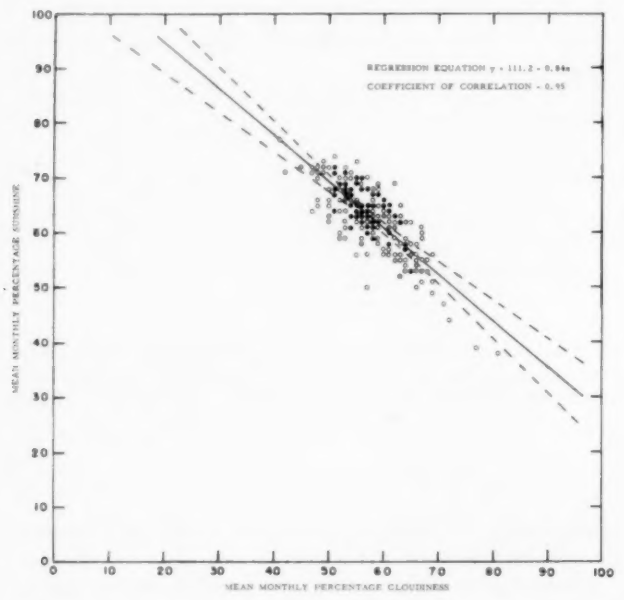
REGRESSION EQUATION y = 111.2 - 0.84x
COEFFICIENT OF CORRELATION = 0.95
MEAN MONTHLY PERCENTAGE SUNSHINE
MEAN MONTHLY PERCENTAGE CLOUDINESS

FIGURE 7.—Mean monthly percentage cloudiness vs. mean monthly percentage sunshine for the cases for the areas with relatively high amounts of stratiform cloudiness in which the sunshine is relatively high with respect to cloudiness. See legend to figure 3.

of data and reveal much less scattering of points than for the data for the 132 stations combined. Also depicted is the higher values of percentage sunshine for given

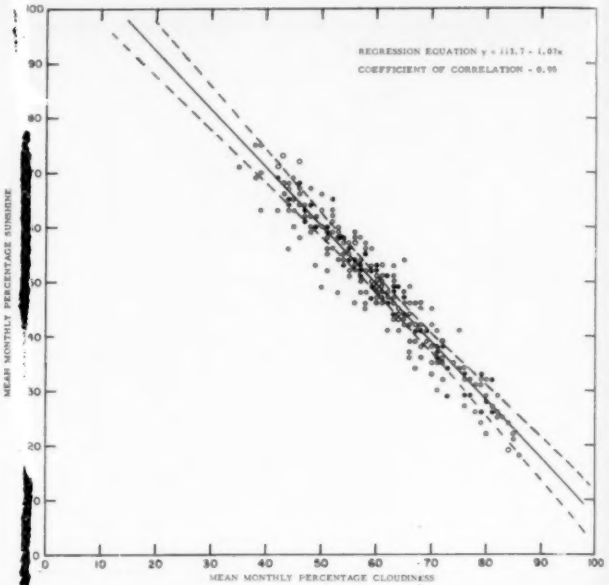
REGRESSION EQUATION y = 113.7 - 1.07x
COEFFICIENT OF CORRELATION = 0.95
MEAN MONTHLY PERCENTAGE SUNSHINE
MEAN MONTHLY PERCENTAGE CLOUDINESS

FIGURE 8.—Mean monthly percentage cloudiness vs. mean monthly percentage sunshine for the cases for the areas with relatively high amounts of stratiform cloudiness in which the sunshine is relatively low with respect to the cloudiness. See legend to figure 3.

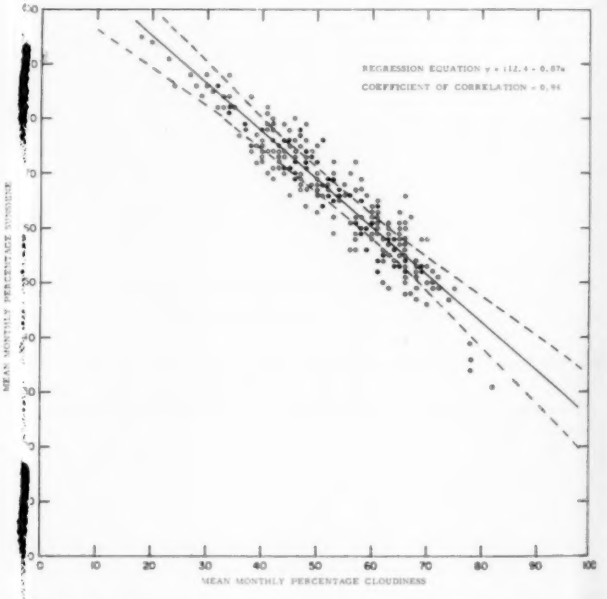
REGRESSION EQUATION y = 112.4 - 0.87x
COEFFICIENT OF CORRELATION = 0.94
MEAN MONTHLY PERCENTAGE SUNSHINE
MEAN MONTHLY PERCENTAGE CLOUDINESS

FIGURE 9.—Mean monthly percentage cloudiness vs. mean monthly percentage sunshine for the cases for the areas with relatively low amounts of stratiform cloudiness in which the sunshine is near average with respect to the cloudiness. See legend to figure 3.

values of percentage cloudiness for the stations in the areas having less stratiform cloudiness and also the lower rate of increase of percentage sunshine with decrease in percentage cloudiness for these stations and vice versa.

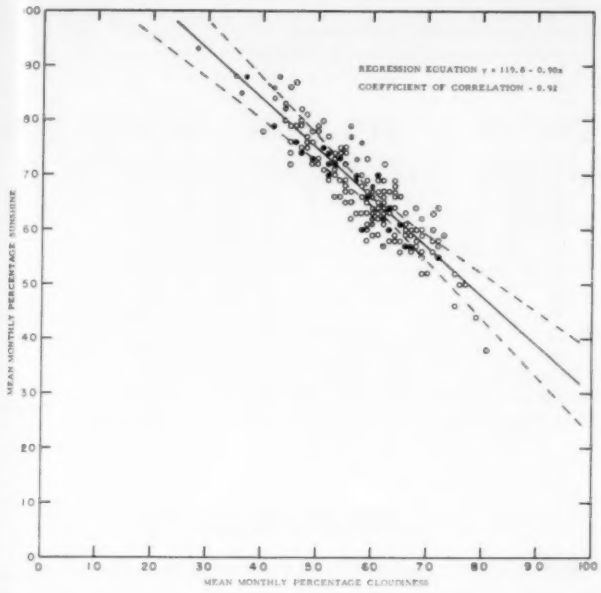

FIGURE 10.—Mean monthly percentage cloudiness vs. mean monthly percentage sunshine for the cases for the area with relatively low amounts of stratiform cloudiness in which the sunshine is relatively high with respect to cloudiness. See legend to figure 3.

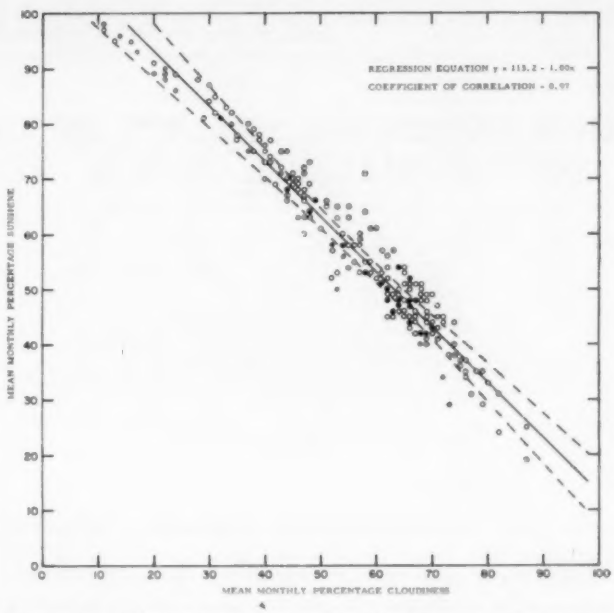

FIGURE 11.—Mean monthly percentage cloudiness vs. mean monthly percentage sunshine for the cases for the areas with relatively low amounts of stratiform cloudiness in which the sunshine is relatively low with respect to the cloudiness. See legend to figure 3.

3. MONTHLY DATA RELATIONSHIPS

Reference to climographs for two widely separated stations having relatively high amounts of stratiform cloudiness, Key West, Fla. and Eureka, Calif., and for two widely separated stations having relatively low amounts of stratiform cloudiness, Little Rock, Ark. and Phoenix, Ariz. (see fig. 5) provides a hint as to the dispersion which would result if all the monthly values for all the relatively high stratiform cloudiness stations were treated together and, correspondingly, all the monthly values for all the relatively low stratiform cloudiness stations were treated together. It also is evident from these climographs that it would be unwise to consider studies of January data separately, February data separately, and so on, since not all the areas with relatively high amounts of stratiform cloudiness have their periods of high percentage cloudiness-low percentage sunshine (and vice versa) concurrently. The same is true for portions of the relatively low stratiform cloudiness areas.

Accordingly, it was decided to consider the monthly values within the two area groupings with respect to whether the percentage of sunshine was low, about average, or high in relation to percentage cloudiness. This was done with each month's data separately for each station in each of the two categories. The procedure was to ascertain whether each monthly value for the station fell within, was outside and above, or outside and below the area determined by the standard error of estimate value reported in figures 3 and 4 when considered with respect to a line parallel to the originally determined regression curve for the sample of stations and passing through the plot of the annual percentage sunshine and percentage cloudiness values for that station (see fig. 5). This placed a reasonable size sample in each of the three sets of data for each of the two types of areas.

This treatment of the data for the stations within various distinct geographical sections of the country revealed that usually about the same set of months had about average, above average, and below average monthly percentage sunshine, respectively, in relation to percentage cloudiness. The monthly data were then arrayed with respect to this qualitative relationship as shown in table 1 and treated to obtain the regression lines, coefficients of correlation, and errors of estimate depicted in figures 6–11. The regression equations are collected in table 2.

Most of the error of estimate values obtained by this procedure are relatively low as revealed in these figures. The regression line for the relatively low percentage sunshine months for the areas of the country with relatively high amounts of stratiform cloudiness is well displaced from that for the relatively low percentage sunshine months for the areas with comparatively low amounts of stratiform cloudiness and far removed from the regression line for the relatively high sunshine months for the latter areas.

TABLE 1.—*Months with relatively high (+), relatively moderate (○), and relatively low (−) values of mean percentage sunshine with respect to values of mean percentage cloudiness for different regions of the United States.*

	J	F	M	A	M	J	J	A	S	O	N	D
H. Areas with Relatively High Amounts of Stratiform Cloudiness												
a. Higher regions of Maine, New Hampshire and Vermont*	○	○	○	○	○	○	○	○	○	○	○	○
b. Great Lakes region including all of Wisconsin and eastern Minnesota	−	○	○	+	+	+	+	○	○	−	−	−
c. Middle eastern and northeastern regions excluding the higher elevation of the far Northeast	−	○	○	○	+	+	+	○	○	−	−	−
d. Southeastern region excluding Florida Peninsula	−	○	○	○	+	+	+	+	○	−	−	−
e. Florida Peninsula*	○	−	○	○	○	+	+	+	○	○	○	○
f. California coastal area*	○	○	○	○	○	○	○	○	○	○	○	○
g. Washington and Oregon coastal area*	○	○	○	+	+	○	○	○	○	○	−	−
h. Southeastern Alaska*	○	○	+	+	○	○	○	○	○	−	−	−
L. Areas with Relatively Low Amounts of Stratiform Cloudiness												
a. North Central region	○	○	+	+	+	○	○	○	○	○	−	−
b. West Central region	−	○	○	○	+	+	+	○	○	−	−	−
c. South Central and East Central regions	−	−	○	○	+	+	+	+	○	−	−	−
d. Northern Rocky Mountain and High Plains regions	○	+	+	+	+	+	○	○	○	−	−	−
e. Southern Rocky Mountain and High Plains regions	○	○	○	+	○	+	○	○	○	−	○	○
f. Cascade Range and northern Plateau regions	○	○	+	+	+	+	○	○	○	○	○	○
g. Sierra Range, San Joaquin Valley, and central Plateau regions	○	○	+	+	+	○	−	−	−	−	○	○
h. Interior Southern California* and southern Plateau regions	○	+	+	+	+	○	○	○	−	−	−	−
i. Cook Inlet Area-Alaska*	−	○	+	+	+	+	+	○	○	−	−	−

*Includes data for fewer than five stations.

4. CONCLUDING REMARKS

This study presents the procedures used and some of the results obtained in determining the relationship between percentage sunshine and percentage cloudiness for United States stations through areal and seasonal groupings of the mean annual and mean monthly data based on relative amounts of stratiform cloudiness. The groupings are by areas for the mean annual and mean monthly data and, further, by portions of the year for the latter.

These treatments of the mean annual and mean monthly percentage sunshine and percentage cloudiness for recent years for United States stations provide realistic and usable measures of the interrelation of these data. Table 2 summarizes these relations.

TABLE 2.—*Equations for interrelation of percentage cloudiness and percentage sunshine. Refer to table 1 for key to the portions of the year covered by each category for the various parts of the country. y is mean percentage sunshine; x is mean percentage cloudiness, sunrise to sunset; and $\overline{S}$ is standard error of estimate.*

H. In Areas with Relatively High Amounts of Stratiform Cloudiness	
a. For mean annual values. (fig. 3)	$y=114.5-0.99x$, $\overline{S}=3.36$
b. For mean monthly values for portion(s) of year with highest amounts of stratiform cloudiness. (fig. 8)	$y=113.7-1.07x$, $\overline{S}=3.51$
c. For mean monthly values for portion(s) of year with lowest amounts of stratiform cloudiness. (fig. 7)	$y=111.2-0.84x$, $\overline{S}=3.87$
d. For mean monthly values for portion(s) of year not included in (b) or (c). (fig. 6)	$y=114.9-1.01x$, $\overline{S}=4.58$
L. In Areas with Relatively Lower Amounts of Stratiform Cloudiness	
a. For mean annual values. (fig. 4)	$y=115.6-0.92x$, $\overline{S}=2.70$
b. For mean monthly values for portion(s) of year with highest amounts of stratiform cloudiness. (fig. 11)	$y=113.2-1.00x$, $\overline{S}=3.53$
c. For mean monthly values for portion(s) of year with lowest amounts of stratiform cloudiness. (fig. 10)	$y=119.8-0.90x$, $\overline{S}=3.74$
d. For mean monthly values for portion(s) of year not included in (b) and (c). (fig. 9)	$y=112.4-0.87x$, $\overline{S}=3.77$

ACKNOWLEDGMENTS

National Weather Records Center personnel assisted in this study. The author is especially indebted to Alan H. Harris and Dick M. Whiting, and to Raymond D. Crane and Eva Holcombe. He is also indebted to Mrs. Rose M. Fries of the Regional Administrative Office, U.S. Weather Bureau, Kansas City, Mo. Without the encouragement of Dr. Helmut E. Landsberg, Director of Climatology, Office of Climatology of the U.S. Weather Bureau, this study would not have been initiated or carried to completion.

REFERENCES

1. U.S. Weather Bureau, "Climates of the States," in "Climate and Man", *Yearbook of Agriculture*, U.S. Department of Agriculture, Washington, D.C., 1941, 1248 pp. (pp. 737–743).
2. H. R. Byers, *General Meteorology*, McGraw-Hill Book Co., Inc., New York and London, 1944, (p. 508).
3. H. Landsberg, *Physical Climatology*, Gray Printing, Inc., Du Bois, Pa., 1958, 446 pp. (pp. 134–135).
4. G. Sternes, "Sunshine and Agriculture," *Weekly Weather and Crop Bulletin, National Summary*, vol. XLV, No. 45, November 10, 1958, pp. 6–8.
5. G. Sternes, "Oregon Sunshine," *Weekly Weather and Crop Bulletin, National Summary*, vol. XLVI, No. 25, June 22, 1959, pp. 6–8.
6. U.S. Weather Bureau, *Local Climatological Data with Comparative Data*, Annual issue, Washington, 1958.

THE ZONAL WIND FIELD ALONG 80° W. FOR THE IGY PERIOD AND NORTHERN HEMISPHERE ANOMALIES OF WIND AND TEMPERATURE

WILLIAM M. McMURRAY

National Weather Records Center, U.S. Weather Bureau, Asheville, N.C.
[Manuscript received June 21, 1961; revised September 8, 1961]

ABSTRACT

A descriptive rather than conclusive discussion of the zonal wind field along the 80° W. meridian for the International Geophysical Year period is presented. Anomaly charts of mid-seasonal months for the Northern Hemisphere and their relationship to general weather features during the IGY are discussed.

1. INTRODUCTION

The expansion of the upper air network in North America throughout the 1940's afforded opportunity for the publication of many significant studies of the vertical aspects of the atmosphere through cross-sectional analyses. Because of the proximity of a large number of stations to the 80° W. longtitude (fig. 1) this meridian became a natural favorite for detailed studies of the westerly current in the Northern Hemisphere. In one of the early studies, Hess [10] utilizing four years of data (1942–1945), included a wider range of latitude (2° S. to 73° N.) and used data more closely arrayed to 80° W. (6° range in longitude) than that of previous works [24]. Although investigations toward specific goals continued [8, 17], Kochanski [13] contributed directly to the 80° W. seasonal mean information by using winds scaled from mean maps [1] and extending the analysis to 30 km. [2]. More recently Landsberg and Ratner [14] have compiled January and July means of zonal wind and temperature along 80° W. using nearly 10 years of data, and Crutcher [4], using six years of data (1948–1953), has completed an extensive statistical study of the wind field with cross-sections for many longitudes and parameters including 80° W. and the zonal component. These last two references were used in preparing the anomaly charts presented here.

Limitations of data have necessarily restricted atmospheric investigations on a cross-sectional basis in the Southern Hemisphere. While some individual cases have been studied [12, 15] and means established for other meridians [7, 21, 23], no "mean" values as such have been established for a longitude near enough to 80° W. to permit construction of anomaly charts for a specific period of record.

Through the impetus of the International Geophysical Year (IGY) the addition of several cooperative stations in South America completed the observational chain between Panama and the Antarctic (fig. 1). Using this network, the U.S. Weather Bureau has prepared daily aerological cross-sections for the IGY period [25], along 80° W. in the Northern Hemisphere and within about 10° longitude of 70° W. in the Southern Hemisphere. As a natural by-product of these analyses on a daily basis, monthly mean cross-sections have also been prepared for the 18 months of the IGY [16] and these form the basis for this presentation.

2. HEIGHT-LATITUDE VARIATION OF MAXIMUM ZONAL WIND

Figure 2 shows the mean monthly positions of the maximum westerly wind component plotted against latitude and height for both hemispheres for the 18 months, July 1957 through December 1958. The cross-hatched areas show the range of the variation with height and latitude. The asterisks in the Northern Hemisphere portion indicate the mean mid-season positions according to Crutcher [4].

The heavy dashed line in the Southern Hemisphere traces the position of a secondary maximum of the zonal wind when this could be positively identified from the data available. As can be seen this secondary maximum was at a much higher latitude, but a lower height, and, for the five months it was in evidence, nearly paralleled the position of the primary maximum of the west wind component.

The graphic determination of the center of the rectangular cross-hatched areas immediately yields the mean of the 18 individual monthly positions of this west wind core at this longitude: 38° N. and 220 mb. (11.5 km.) in the Northern Hemisphere and 31° S. and 195 mb. (12 km.) in the Southern Hemisphere. It was necessary to identify these maximum westerly wind components as "near the tropopause" since there is conclusive evidence on the mean monthly cross-sections [16] that much stronger maxima existed at higher altitudes and latitudes during the winter months. This increase of zonal wind with height between 50° and 70° S. is well recognized and has

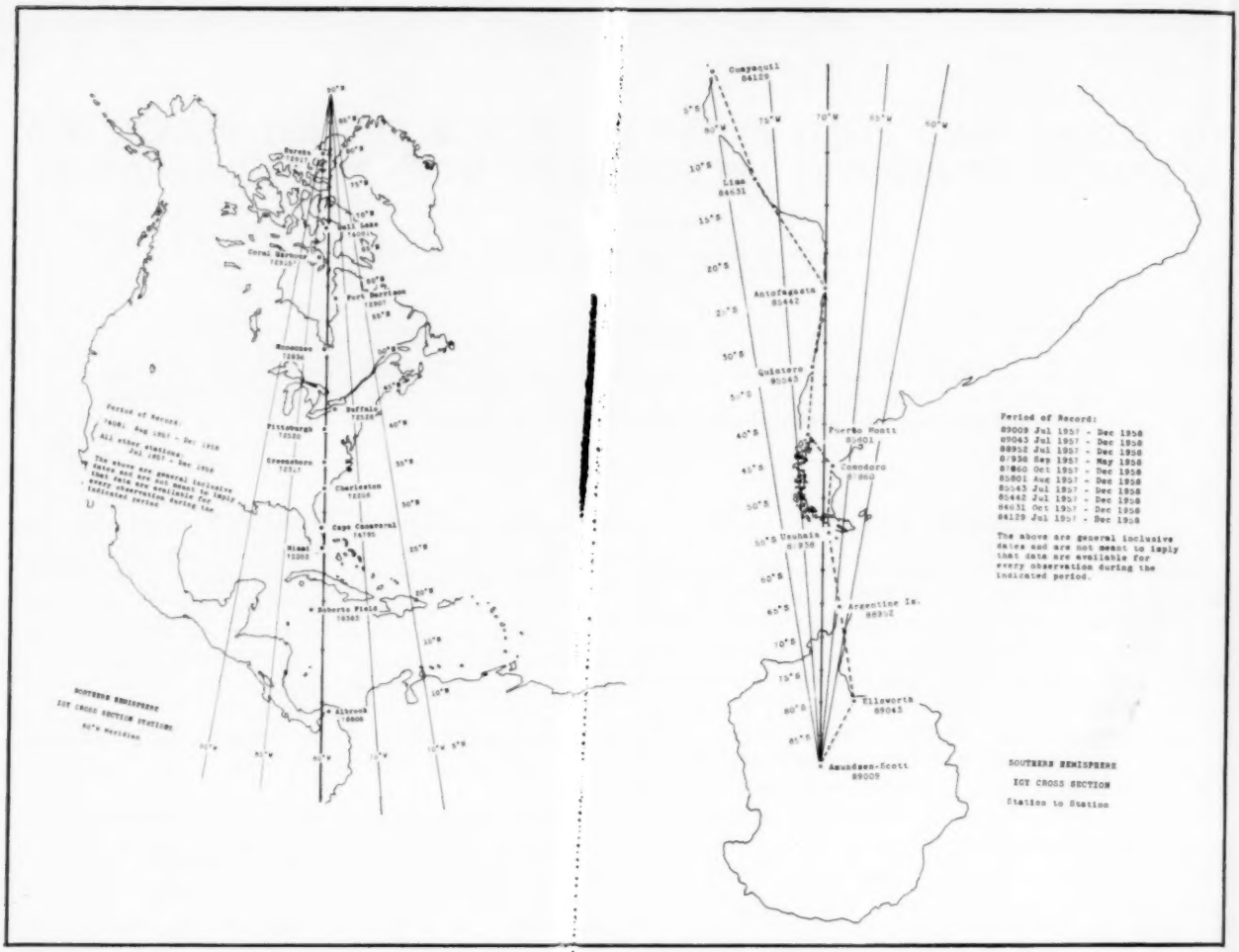
Period of Record:
89009 Jul 1957 - Dec 1958
89043 Jul 1957 - Dec 1958
88958 Jul 1957 - Dec 1958
87938 Sep 1957 - May 1958
87860 Oct 1957 - Dec 1958
85801 Aug 1957 - Dec 1958
85442 Jul 1957 - Dec 1958
84631 Oct 1957 - Dec 1958
84129 Jul 1957 - Dec 1958
The above are general inclusive dates and are not meant to imply that data are available for every observation during the indicated period.
SOUTHERN HEMISPHERE
IGY CROSS SECTION
Station to Station

FIGURE 1.—Upper air station distribution along 80°/70° W. While the Northern Hemisphere network has been in existence for some time, the IGY promoted most of the Southern Hemisphere cooperatives which completed the pole-to-pole chain. Asterisks indicate actual locations of stations. Station numbers are according to WMO Block and Index designations.

been discussed by Taylor [21], van Loon [23], and Hofmeyr [11].

Of interest is the rather abrupt and definite equatorward shift of the zonal maxima in the Northern Hemisphere in fall and winter and the poleward march in spring and summer, as compared with similar but less well defined shifts in the Southern Hemisphere. Comparisons of speeds and latitude fluctuations between the zonal maxima of the two hemispheres can also be made readily from figure 2.

A comparison of the positions of the mean summer and winter jet streams along longitudes 130° E. and 150° E. [7] with the Southern Hemisphere zonal wind maxima in figure 2 is interesting, but far from conclusive. While the July 1957 maximum is similar in height, strength, and latitude (200 mb., 50 m./sec. and 27° S.) to the winter maximum along 130° E., a predominantly continental longitude, the 1958 winter with double maxima of less strength is more analogous to the winter mean along 150° E., a predominantly oceanic longitude. In comparing summer values, the January 1958 zonal maximum is not quite as strong but in the same position as the summer mean for 130° E. longitude. No summer double maxima occurred during the IGY to compare with those shown on the mean chart for 150° E. longitude by Gibbs [7], or along the 170° E. longitude as shown by Hutchings [12]. On the other hand, van Loon [23] found no double maxima in summer or winter on cross-sections for a Southern Hemisphere oceanic region. While it appears these differences are attributable in part to a continental influence, it is beyond the scope of this presentation to establish to what degree these referenced cross-sections are representative of the mean zonal wind over the Southern Hemisphere.

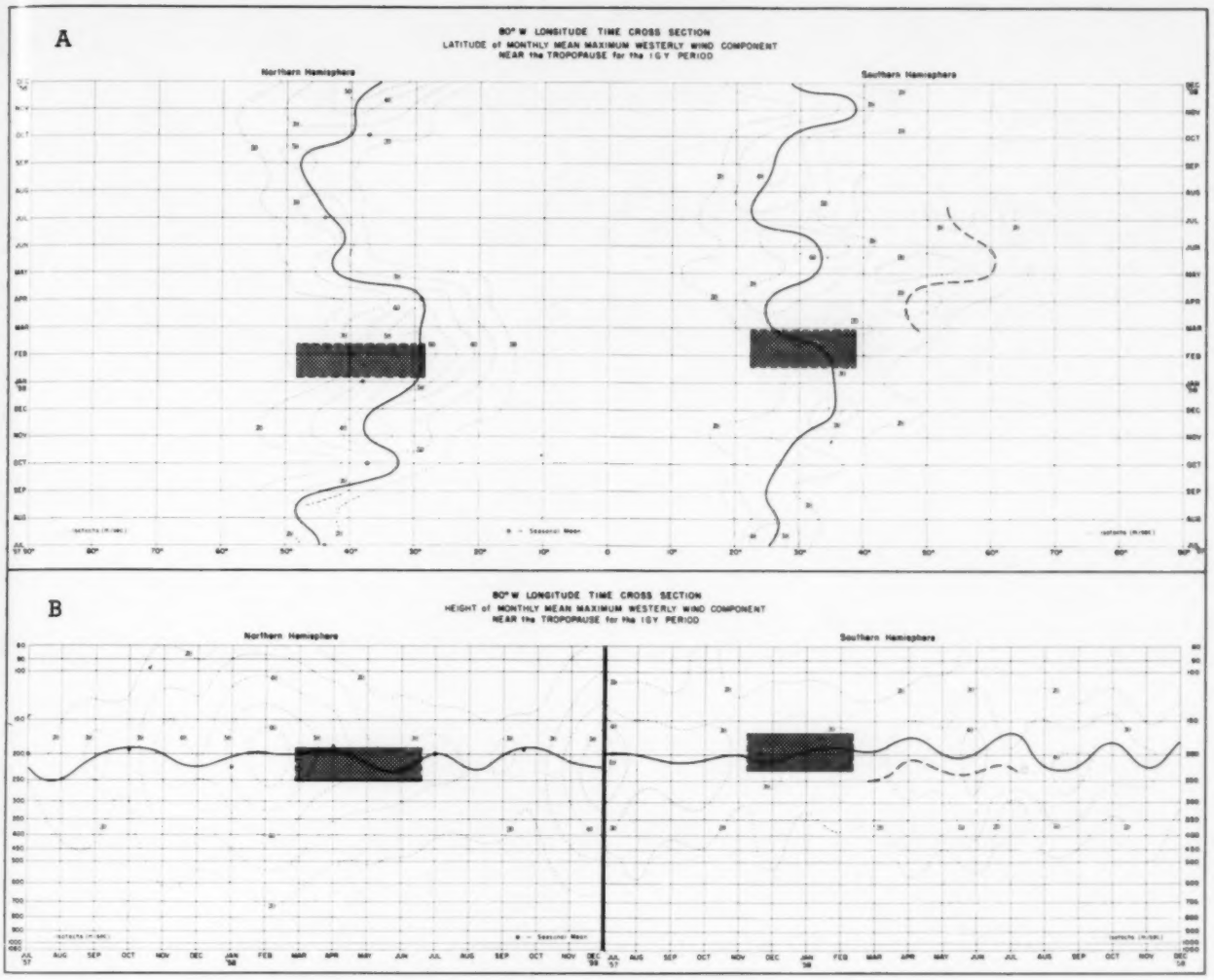
A
80° W LONGITUDE TIME CROSS SECTION
LATITUDE of MONTHLY MEAN MAXIMUM WESTERLY WIND COMPONENT
NEAR the TROPOPAUSE for the IGY PERIOD
Northern Hemisphere
Southern Hemisphere
B
80° W LONGITUDE TIME CROSS SECTION
HEIGHT of MONTHLY MEAN MAXIMUM WESTERLY WIND COMPONENT
NEAR the TROPOPAUSE for the IGY PERIOD
Northern Hemisphere
Southern Hemisphere

FIGURE 2.—Time cross sections by (A) latitude and (B) height of monthly mean westerly wind component near tropopause. Positions of the monthly mean west wind maxima are connected by the heavy solid line; isotachs in m./sec. are shown as dashed lines; range of latitudinal and height variation of west wind maxima for 18-month IGY period is cross-hatched. Seasonal mean positions (*) of west wind maxima are taken from [4].

3. NORTHERN HEMISPHERE ANOMALY CHARTS

Two sets of mean charts were used to subtract from the mean monthly charts in order to arrive at the anomaly charts presented. In addition to the interesting comparisons resulting from two independently produced sets of means, Crutcher [4] presented four seasonal charts to which the mid-season months of July, October, January, and April were compared, and Landsberg and Ratner [14], although preparing charts for only July and January, included temperatures and zonal winds to higher altitudes.

JULY 1957

The extremely flat gradients of west wind and temperature differences shown in figure 3 are significant in illustrating how nearly "normal" this month was in these parameters [9]. A trough off the east coast was effective in producing only slightly above normal west wind components and slightly cooler than normal temperatures (fig. 3B) in low and middle latitudes. The normality of the month is further evidenced by the proximity of the position of the seasonal to that of the actual mean west wind maximum as shown in figure 2. Of interest also is the coincident positioning at 55° N. of the 5 m./sec. deficiency of west wind component during the month, although these anomalies were computed independently from the two source means [4, 14]. It should also be noted that the greatest differences in the two anomaly charts for this month are in low latitudes.

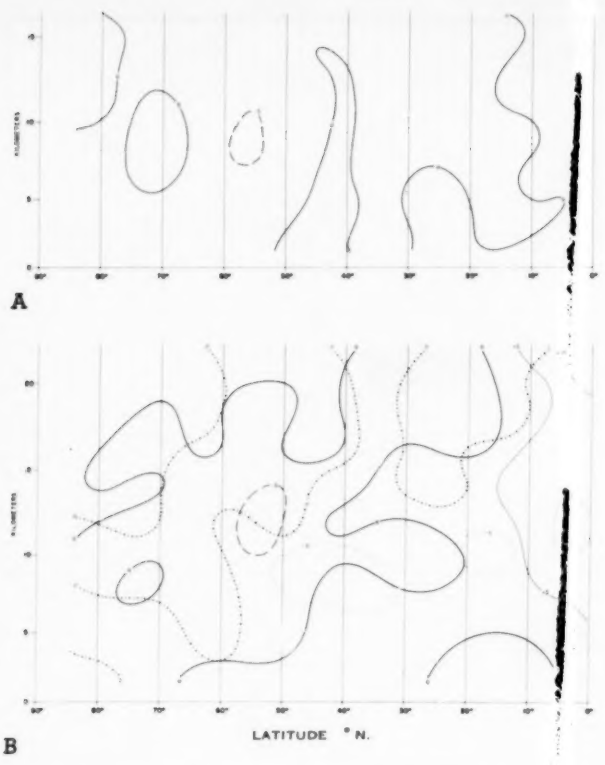

FIGURE 3.—July 1957: (A) west wind anomaly using means by Crutcher [4], and (B) west wind anomaly and temperature anomaly derived by subtracting west wind and temperature means by Landsberg and Ratner [14] from the July 1957 mean. Winds are heavy lines in intervals of 5 m./sec.; temperatures are broken or light-dashed lines in intervals of 5° C.

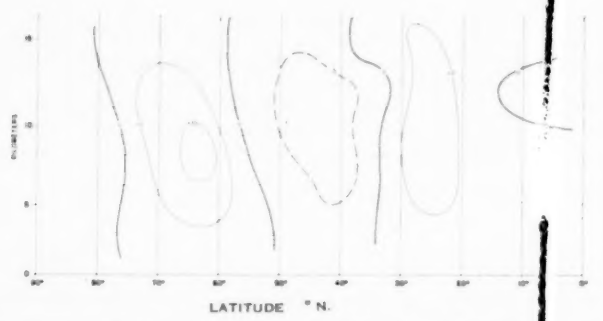

FIGURE 4.—October 1957 west wind anomaly. Excesses of west wind component over fall season mean [4] in higher and lower latitudes caused by a split in the main stream westerlies (see text).

OCTOBER 1957

As described more extensively in [6] the circulation for this month was characterized by a split in the westerlies resulting in two west wind maxima, one at 30° N. and another between 60° and 70° N. This feature was also reflected in the analysis of the mean monthly cross-sections, but since this double maximum feature existed only for one month it was not made a part of figure 2. This split is graphically presented in figure 4 as producing anomalies showing an excess of west wind component over the normal in the lower latitudes and even greater excesses about 65° N. As a natural result of this split in the main westerly stream away from its normal position at about 40° N., an extensive deficiency of west wind component appears near this latitude. More obviously evident here than in figure 3, but a feature on most of the anomaly charts presented, is the balancing in both extent and intensity of the areas of excesses and deficiencies of west wind components. This evidence of the conservation of the total momentum of the westerlies is a well known phenomenon and has been investigated in detail by Namias [18] and others.

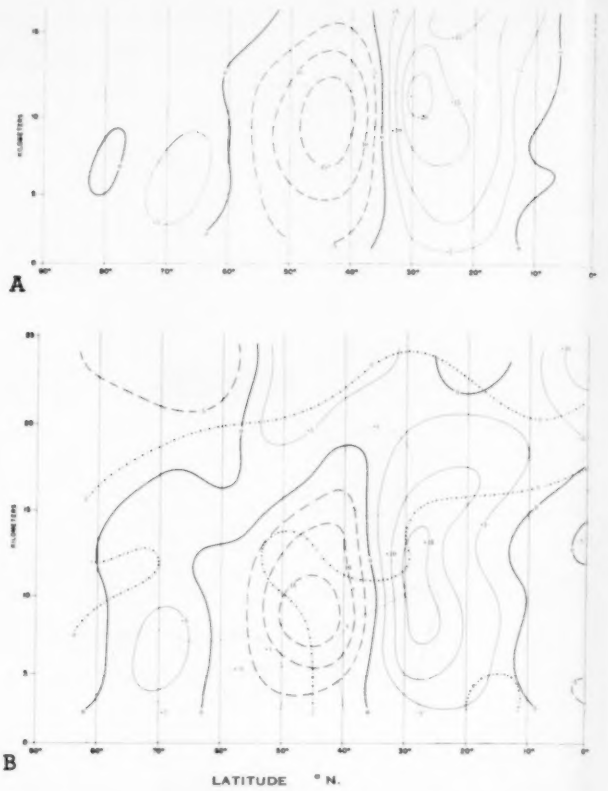

FIGURE 5.—January 1958: (A) west wind anomaly, and (B) west wind and temperature anomalies. Sources of means and contour intervals as explained for figure 3. Large anomalies result as mid-winter jet is displaced southward.

JANUARY 1958

With the migration southward of the upper-level westerlies into the subtropics (see fig. 2), followed by the formation of an abnormally large blocking anticyclone in the Davis Strait [19], January turned out to be the most anomalous month of the series. These features are well reflected in figure 5 with excesses of west wind component from 10° N. to 35° N. and up to the 40-mb. level (22 km.)

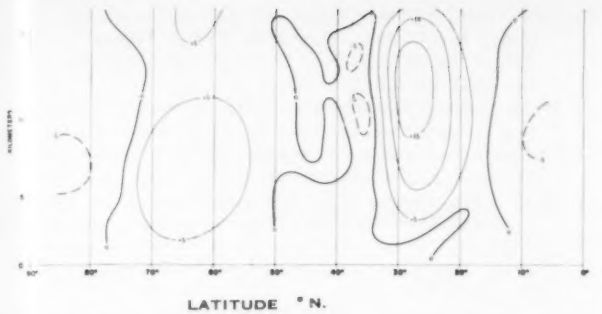

FIGURE 6.—April 1958 west wind anomaly. Large excesses of west wind component caused by circulation strength rather than by displacement from normal position. Notice the resulting excess of positive values over negative (deficiency of west wind from normal) values—a feature not evident in other months.

compensated for by similarly intense deficiencies of west wind from normal in temperate latitudes. The accompanying import of colder than normal temperatures in lower latitudes and up to the 10-km. (260-mb.) level is also evident. The striking similarity of west wind anomalies computed from the two different means is worthy of special note.

Near mid-month an almost record-breaking blocking anticyclone in the Davis Strait west of Greenland caused sustained advection of maritime air from the Atlantic to reach even farther inland than the 80° W. longitude [22]. The much above normal temperatures which resulted appear as +5° to +10° C. anomalies between 50° N. and 70° N. in figure 5B.

APRIL 1958

A fine illustration of the fact that *both* position *and* speed of the west wind maxima are important in reflecting excesses and deficiencies in the anomalies can be seen in figure 6. While the position of the mean maximum west wind for the month was coincident with the seasonal mean position (fig. 2), the excesses shown in figure 6 are of the same magnitude as those shown in figure 5 when the axis of the west wind component was displaced some 8° of latitude from the normal position. The excesses then, in figure 6, are the result of much stronger than normal west wind components during this particular month than would be expected in the mean.

April circulation through 80° W. longitude was also influenced by blocking in mid-latitudes resulting in a split of the jet stream at all levels up to 15 km. [20] and the corresponding west wind excesses between 60° N. and 70° N. as well as between 20° N. and 35° N. An incidental maximum is also evident in figure 6 at about 40° N.

As an exception to a statement made previously, the excesses far outweigh the deficiencies of west wind component for this month as shown in figure 6—at least through the lower 15 km.

JULY 1958

The main features of the circulation for this month,

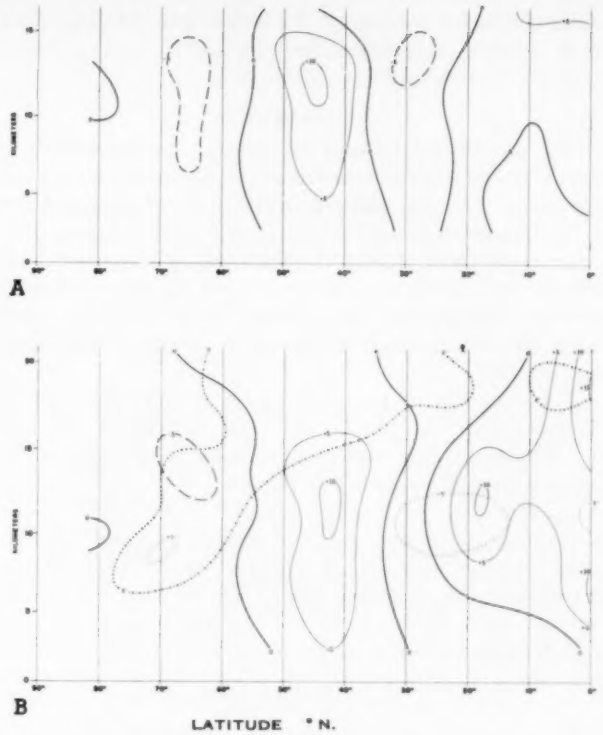

FIGURE 7.—July 1958: (A) west wind anomaly and (B) west wind and temperature anomalies (see legend to figure 3). Another example of reinforcement of west wind component in normal position. 10 m./sec. excess in mid-latitude as compared with July 1957 in figure 3 is also evident from isotachs in figure 2.

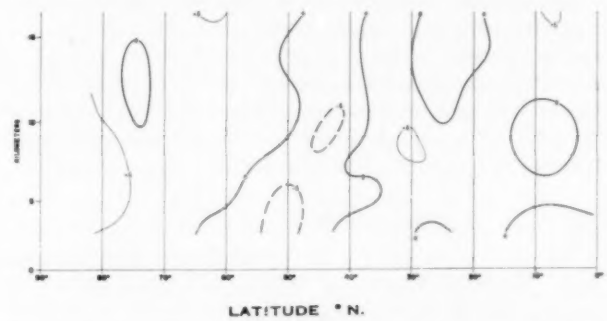

FIGURE 8.—October 1958 west wind anomaly. Although a large-amplitude cyclic variation of the zonal index was evident in the daily values (see text) the monthly mean west wind anomaly is relatively flat. The results of some splitting of the main westerly flow are also evident.

i.e., blocking in the North Atlantic and a stronger than normal Bermuda High [5], rather than shifting the position of the west wind jet, reinforced the jet in its normal position. That this strengthening amounted to about 10 m./sec. in the mean can be seen by comparing figure 7 with figure 3 and the relative positions and intensities of the west wind maxima in figure 2 for July 1957 and July 1958.

As mentioned previously, the two sources of mean data show greatest differences for this month and in lower latitudes at about 12 km. (195 mb.).

OCTOBER 1958

One of the weaknesses of "mean" presentations of specific parameters is reflected in the rather flat west wind component anomaly pattern in figure 8. As pointed out in [3] the month did gain its character from a pronounced index cycle—high during the first half of the month and low during the latter half—but due to the averaging process the monthly mean value of the 700-mb. zonal index showed as small an anomaly as any month since August 1957!

A comparison of figures 4 and 8 reveals the marked similarities of the 1957 and 1958 circulation through 80° W. during this month of climatic transition. Both years were influenced by a blocking in central Canada which caused a split in the main core of westerlies. This division of the main stream of westerlies away from its usual location near 40° N. resulted in generally similar patterns of excesses and deficiencies of west wind components for both Octobers, i.e., positive areas in low and high latitudes toward which the split jets were shunted, and negative areas in mid-latitudes which usually experience the full force of the primary mean westerly flow.

As has been noted in other cases, figure 8 shows a rather striking balance between positive and negative areas.

4. SUMMARY

Time cross-sections of the monthly mean maximum westerly wind components for the IGY period show a range in position of approximately 20° of latitude and 1.5 km. of altitude in the Northern Hemisphere, and 17° of latitude and 1.7 km. of altitude in the Southern Hemisphere. Height of the mean position oscillated about the 220-mb. (11.5-km.) level in the Northern and near the 200-mb. (12-km.) level in the Southern Hemisphere.

ACKNOWLEDGMENTS

The author is indebted to Mr. Stanley G. Holbrook and Miss Dorothy Goodman for their assistance in the preparation of the cross-sections.

REFERENCES

1. Air Weather Service, "Mean Monthly Maps of 500-, 200-, 100-, 50-, and 25-mb. Surfaces over North America." *Technical Report* 105–107, Washington, D.C., 1953, 44 pp.
2. Air Weather Service, "Temperatures at the 10-mb. (101,000-foot) Level," *Technical Report* 105–108, Washington, D.C., 1953, 33 pp.
3. J. F. Andrews, "The Weather and Circulation of October 1958—A Month Characterized by a Pronounced Index Cycle," *Monthly Weather Review*, vol. 86, No. 10, Oct. 1958, pp. 408–415.
4. H. L. Crutcher, "Meridional Cross Sections, Upper Winds over the Northern Hemisphere," U. S. Weather Bureau, *Technical Paper No. 41*, 1961. (See Charts 1–5, 2–5, 3–5, 4–5).
5. C. R. Dunn, "The Weather and Circulation of July 1958—Heavy Precipitation Associated With a Trough in Central United States," *Monthly Weather Review*, vol. 86, No. 7, July 1958, pp. 268–276.
6. H. M. Frazier, "The Weather and Circulation of October 1957—A Month with a Record Low Zonal Index for October in the Western Hemisphere," *Monthly Weather Review*, vol. 85, No. 10, Oct. 1957, pp. 341–349.
7. W. J. Gibbs, "Notes on the Mean Jet-Stream Over Australia," *Journal of Meteorology*, vol. 9, No. 4, Aug. 1952, pp. 279–284.
8. A. Gilchrist, "Upper Winds in the Tropics and Subtropics," Great Britain, Meteorological Research Committee, *M.R.P. 795*, April 1953, 15 pp.
9. H. F. Hawkins, Jr., "The Weather and Circulation of July 1957—Drought in the East," *Monthly Weather Review*, vol. 85, No. 7, July 1957, pp. 254–258.
10. S. L. Hess, "Some New Mean Meridional Cross Sections Through the Atmosphere," *Journal of Meteorology*, vol. 5, No. 6, Dec. 1948, pp. 293–300.
11. W. L. Hofmeyr, "Upper Air over the Antarctic," in *Meteorology of the Antarctic*, M. P. Van Rooy, (Editor), South Africa, Weather Bureau, Pretoria, 1957, pp. 173–208, (see pp. 183–184).
12. J. W. Hutchings, "A Meridional Atmospheric Cross Section for an Oceanic Region," *Journal of Meteorology*, vol. 7, No. 2, Apr. 1950, pp. 94–100.
13. A. Kochanski, "Cross Sections of the Mean Zonal Flow and Temperature Along 80° W.," *Journal of Meteorology*, vol. 12, No. 2, Apr. 1955, pp. 95–106.
14. H. E. Landsberg and B. Ratner, "Neue Klimatische Meridionalschnitte der Atmosphäre," F. Baur, *Link's Meteorologisches Taschenbuch*, 3d Edition, Akademie Verlag, Leipzig, (in press).
15. F. Loewe and U. Radok, "A Meridional Aerological Cross Section in the Southwest Pacific," *Journal of Meteorology*, vol. 7, No. 1, Feb. 1950, pp. 58–65.
16. W. M. McMurray, C. O. Erickson, and H. L. Crutcher, *Monthly Mean Aerological Cross Sections Pole to Pole Along 75° W. For the IGY Period*, U.S. Weather Bureau, Washington, D. C., 1961.
17. Y. Mintz and G. Dean, "The Observed Mean Field of Motion of the Atmosphere," *Geophysical Research Papers*, No. 17, U. S. Air Force, Cambridge Research Center, Aug. 1952, 65 pp.
18. J. Namias, "The Index Cycle and Its Role in the General Circulation," *Journal of Meteorology*, vol. 7, No. 2, Apr. 1950, pp. 130–139.
19. J. F. O'Connor, "The Weather and Circulation of January 1958—Low Index with Record Cold in Southeastern United States," *Monthly Weather Review*, vol. 86, No. 1, Jan. 1958, pp. 11–18.
20. P. Stark, "The Weather and Circulation of April 1958," *Monthly Weather Review*, vol. 86, No. 4, Apr. 1958, pp. 132–140.
21. R. C. Taylor, "Mean Monthly Meridional Cross-Sections of Temperature from the South Pole to the North Pole near 170° E.—A Preliminary Note," *Antarctic Meteorology, Proceedings of the Symposium Held in Melbourne February 1959*, Pergamon Press, 1960, pp. 439–452.
22. M. K. Thomas and R. L. Titus, "Abnormally Mild Temperatures in the Canadian Arctic During January 1958," *Monthly Weather Review*, vol. 86, No. 1, Jan. 1958, pp. 19–22.
23. H. van Loon, "A Note on Meridional Atmospheric Cross Sections in the Southern Hemisphere," *Notos*, vol. 4, No. 2, 1955, pp. 127–129.
24. H. C. Willett, *Descriptive Meteorology*, Academic Press, New York, 1944, 310 pp. (pp. 63–70 and 131–135).
25. U. S. Weather Bureau, *Daily Aerological Cross Sections Pole to Pole Along Meridian 75° W. for the IGY Period*, July 1957 to December 1958, Inclusive (to be published).

Weather Note

THE MIDDLE MISSISSIPPI VALLEY HYDROMETEOROLOGICAL STORM OF MAY 4–9, 1961

JERROLD A. LARUE AND RUSSELL J. YOUNKIN
National Meteorological Center, U.S. Weather Bureau, Washington, D.C.
[Manuscript received June 26, 1961; revised Aug. 14, 1961]

1. INTRODUCTION

A hydrometeorological storm of major importance occurred over the middle Mississippi Valley, mainly from eastern Oklahoma and eastern Kansas eastward into the Ohio Valley, during the period May 4–9, 1961. Flooding from the heavy rainfall ranged from the flashtype to large-scale overflow. Approximately ten fatalities were attributed to the heavy rain and flooding. Total evaluation of property damage is yet to be completed, but preliminary estimates of damage are in the millions of dollars. The magnitude of the storm is evident from figure 1A which is the smoothed analysis of total storm rainfall, as reported by selected stations during the 6-day period ending 1200 GMT May 9.

This note presents a short description of the surface and 500-mb. features of the storm, the vertical motions as computed by the warm-air advection method used by the Quantitative Precipitation Forecasting (QPF) Unit of the National Meteorological Center, and the Unit's operational, 24-hour, quantitative forecasts and their verification. A composite storm forecast and verification is given, since in larger river basins precipitation in successive 24-hour periods becomes increasingly important.

2. SYNOPTIC SITUATION

The May 3–9 series of 1200 GMT synoptic surface and 500-mb. charts is shown in figures 2–8. Observed precipitable water analyzed for increments of 0.25 inch and the observed 1-inch isohyet for the 24 hours prior to map time are superimposed on the surface charts. Computed average vertical motions for the 1000–500-mb. layer are superimposed on the 500-mb. charts.

The 500-mb. chart on May 3 (fig. 2B), immediately preceding the outbreak of the heavy precipitation, showed the long-wave trough position established over the western States. This position was maintained during the first half of the period, but on May 7 (fig. 6B) an eastward shift commenced and, by May 9 (fig. 8B) the long-wave trough had advanced to the Mississippi River. Prior to its displacement eastward, three short-wave troughs had moved through the long-wave trough and into the Central Plains.

The surface charts show only three distinct systems over the central United States during this period. The first surface Low, already established over the Panhandles of Texas and Oklahoma on the 3d (fig. 2A), remained nearly stationary for the first 48 hours. It then moved northeastward decreasing in intensity and becoming only a weak wave off the New England coast on May 8 (fig. 7A). The second surface Low formed rapidly over Kansas on the 7th (fig. 6A) and immediately moved northeastward through the Great Lakes. The final surface system formed as a wave on the front in Oklahoma on the 8th (fig. 7A) and moved on a northeastward course a little south of its predecessors.

3. VERTICAL MOTIONS

The vertical motions used by the QPF Unit are computed by a technique based primarily on the indicated rate of warm advection.* The precipitation rate was established by statistically relating the indicated rate of warm advection, the available moisture, and the observed precipitation. Conversion to cm. sec.$^{-1}$ was accomplished by a comparison of the indicated rate of warm advection and the vertical motion required to produce equal precipitation rates.

The indicated rate of warm advection is obtained operationally using the 1000–500-mb. thickness (Z_s) to describe the thermal field and the 1000-mb. geostrophic wind ($\mathbf{V}_0$), the wind field. The resultant vertical motion (W), which is a mean value for the 1000–500-mb. layer, is given by $W=C\ (\mathbf{V}_0\cdot\nabla Z_s)$ where C is constant.

The vertical motions shown in the accompanying figures were obtained during routine operation which makes use of the Radat 500-mb. chart, available much earlier than the regularly analyzed 500-mb. charts reproduced here. Only positive vertical motions were computed, since negative motions are unimportant to QPF.

On the first day of the period (fig. 2B), centers of positive vertical motion were over the Oklahoma Panhandle region and over southern Nevada. The eastern center lacked upper-air support and consequently failed to move

*More detailed descriptions of the operational computation of the vertical velocities, and of the QPF technique used by the Unit, have been included in the "Synoptic Meteorological Practices at the National Weather Analysis Center, Part II," which is expected to be available late in 1961.

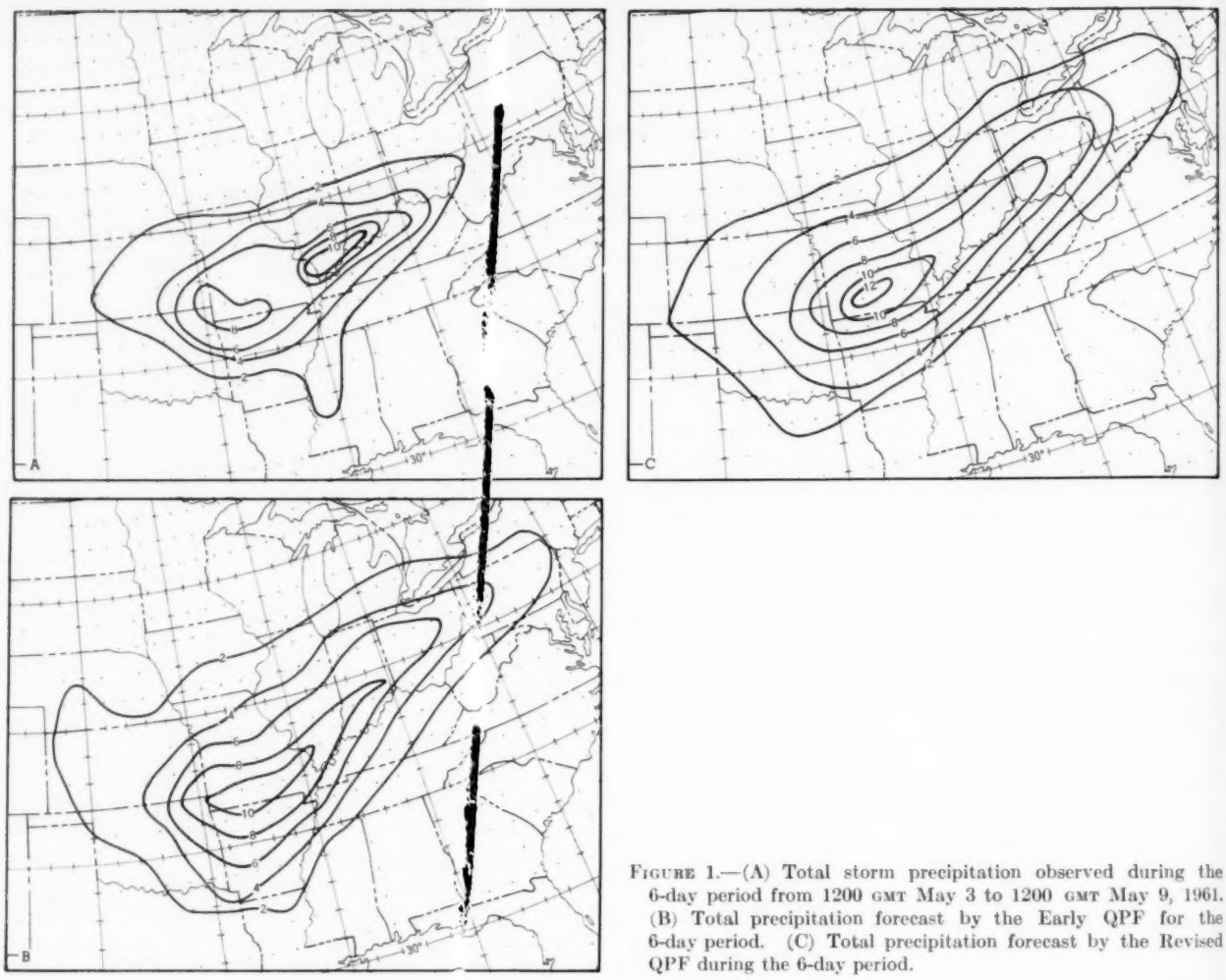

FIGURE 1.—(A) Total storm precipitation observed during the 6-day period from 1200 GMT May 3 to 1200 GMT May 9, 1961. (B) Total precipitation forecast by the Early QPF for the 6-day period. (C) Total precipitation forecast by the Revised QPF during the 6-day period.

during the ensuing 24 hours, but the one to the west moved eastward and combined with the center over Oklahoma. This appeared on May 5 (fig. 4B) to be the same center over southern Kansas, but a closer inspection of the vertical motion gradients indicate that that center had actually weakened and moved to Illinois and Iowa while a weak vertical motion area that had been over eastern Nevada reinforced the area of vertical motion to the east. At this time two other positive vertical motion areas were visible as they swung around the long-wave trough position. These two areas moved little during the next 24 hours while the area to the east moved on eastward, weakened, and became disorganized (fig. 5b). A drastic change in the vertical motion pattern had occurred by May 7 (fig. 6B) with the center over southwestern United States moving into Kansas and being replaced by the area that had been along the west coast. By May 8 (fig. 7B), the Kansas center had moved over the Great Lakes and again weakened as it did so, while the one in the Southwest had moved to northeastern Oklahoma. This latter center proved to be the last of the series and the final chart (fig. 8B) shows its eastward progression.

4. MOISTURE

The precipitable water, representing the moisture field in figures 2A–8A, is a measure of the moisture available to the precipitation process rather than an indicator of the location of the precipitation occurrence. Inspection shows that the 24-hour 1-inch precipitation amounts occurred in areas where the precipitable water values reached at least 0.75 inch sometime during the period, and that the larger amounts generally were associated with precipitable water areas of over 1 inch.

5. FORECASTS

The Quantitative Precipitation Forecasting Unit has

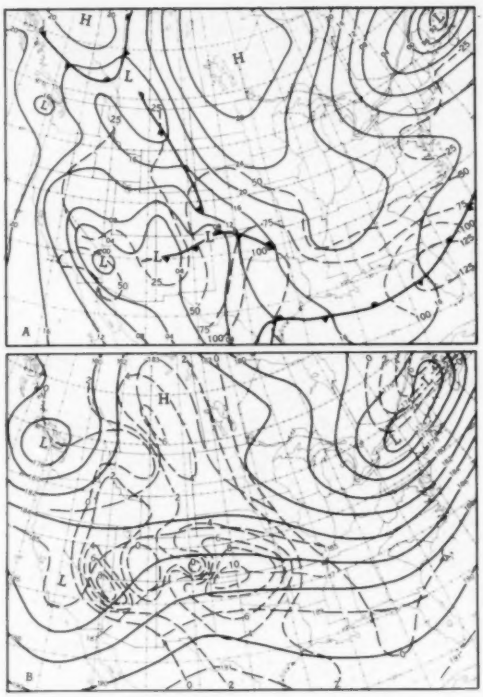

FIGURE 2.—(A) Surface (solid lines) and precipitable water (dashed lines) analyses, 1200 GMT, May 3, 1961. (B) Analyzed 500-mb. contours (solid lines) and computed positive vertical velocities (dashed lines) 1200 GMT May 3, 1961.

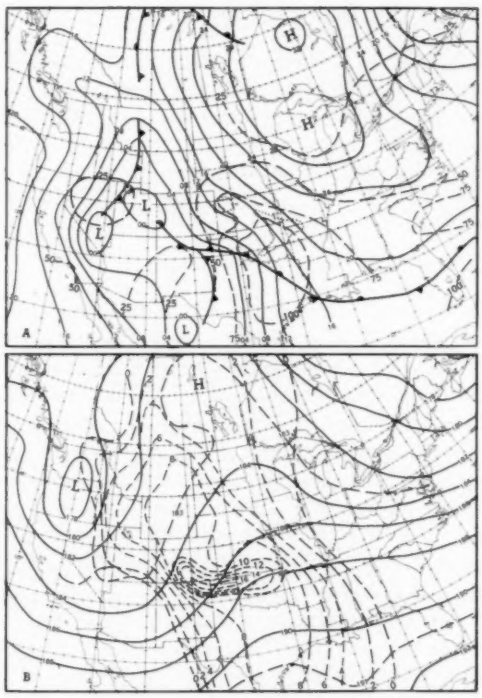

FIGURE 3.—(A) Surface (solid lines) and precipitable water (dashed lines) analyses 1200 GMT, May 4, 1961 with 1-inch isohyets (dotted lines) observed during the preceding 24 hours. (B) Same as figure 2B, but for 1200 GMT, May 4, 1961.

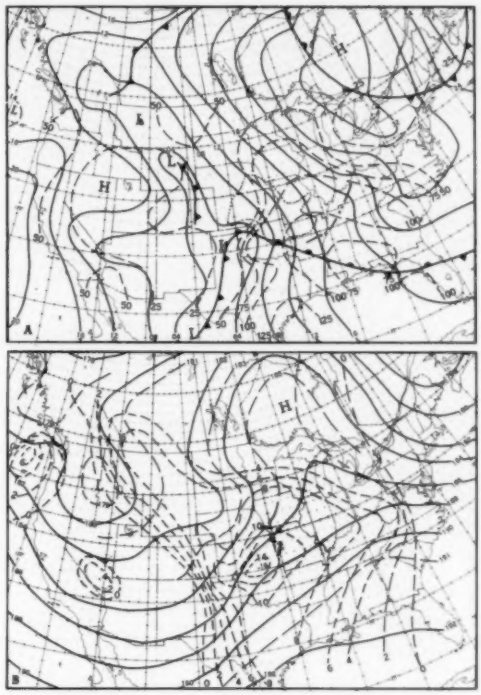

FIGURE 4.—(A) Surface (solid lines) and precipitable water (dashed lines) analyses 1200 GMT, May 5, 1961 with 1-inch isohyets (dotted lines) observed during the preceding 24 hours. (B) Analyzed 500-mb. contours (solid lines) and computed positive vertical velocities (dashed lines) 1200 GMT, May 5, 1961.

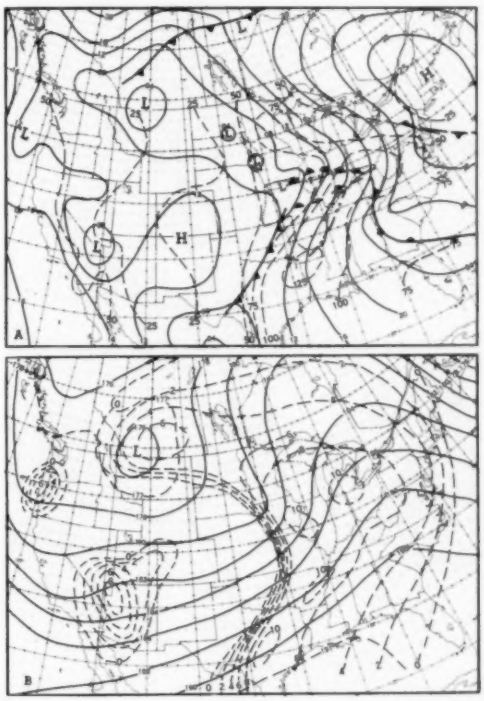

FIGURE 5.—Same analyses as in figure 4 but for 1200 GMT, May 6, 1961.

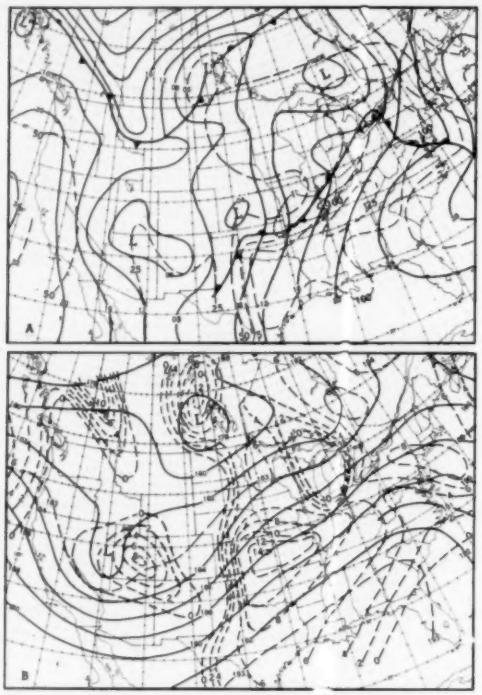

FIGURE 6.—(A) Surface (solid lines) and precipitable water (dashed lines) analyses 1200 GMT, May 7, 1961 with 1-inch isohyets (dotted lines) observed during the preceding 24 hours. (B) Analyzed 500-mb. contours (solid lines) and computed positive vertical velocities (dashed lines) 1200 GMT, May 7, 1961.

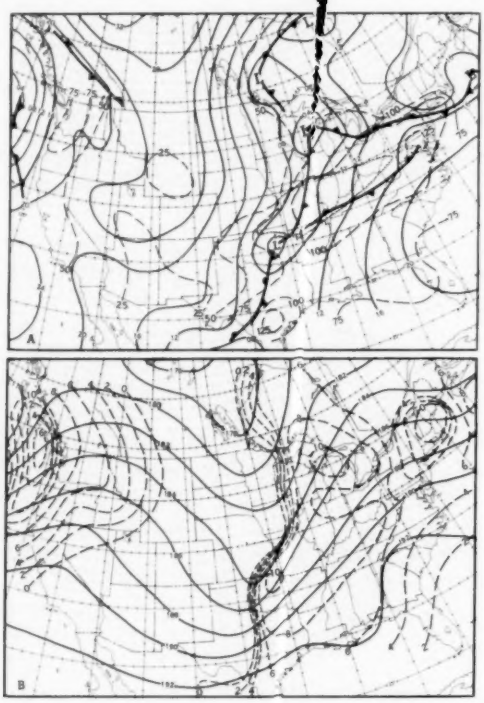

FIGURE 7.—Same analyses as in figure 6 but for 1200 GMT, May 8, 1961.

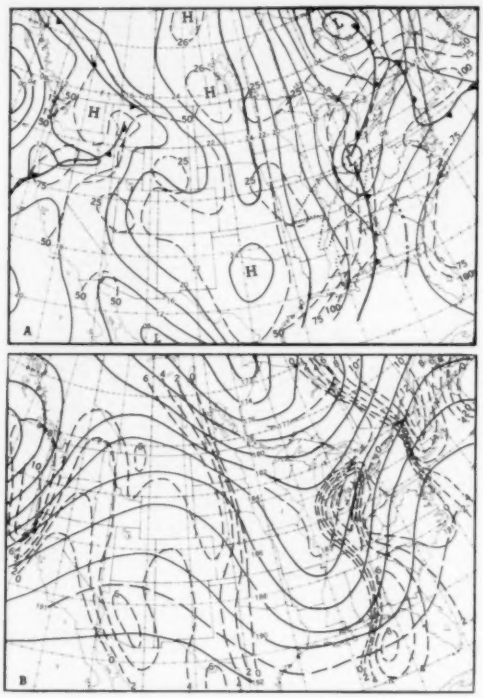

FIGURE 8.—(A) Surface (solid lines) and precipitable water (dashed lines) analyses 1200 GMT May 9, 1961 with 1-inch isohyets (dotted lines) observed during the preceding 24 hours. (B) Analyzed 500-mb. contours (solid lines) and computed positive vertical velocities (dashed lines) 1200 GMT, May 9, 1961.

responsibility for general guidance of other Weather Bureau offices, over the nation, in their 24-hour quantitative precipitation forecasts. Forecasts are issued twice daily by the Unit for the period 1200 GMT to 1200 GMT. The first forecast, which is referred to as the "Early Forecast," is issued at approximately 1200 GMT and the second, the "Revised Forecast," is issued at approximately 1700 GMT.

Daily 24-hour forecasts of precipitation amounts for selected stations were totaled over the storm period. These were analyzed to give a smooth isohyetal pattern (fig. 1B, C) of total forecast precipitation for the storm. An areal verification was then made of the total forecast against the total observed. The area forecast (A_f), the area observed (A_0), and the area correct (A_c) were measured with a planimeter. Having done this, it is a simple matter to obtain the "prefigurence," A_c/A_f, the "post-agreement," A_c/A_0, and the "threat score," $A_c/[(A_f-A_c)+(A_0-A_c)+A_c]$. The "prefigurence" is simply that portion of the area correctly forecast compared to the total area forecast, while the "post-agreement" compares the area correctly forecast to the total area observed. The "threat score" compares the area correctly forecast to the total area forecast and observed. Therefore a perfect forecast has a "threat score" of 1.00. These verification results are given in table 1.

TABLE 1.—*Verification scores of forecast precipitation amounts totaled for the storm period of 1200 GMT, May 3 to 1200 GMT, May 9, 1961. The Early Forecast refers to the one issued at approximately 1200 GMT and the revised to the one issued at 1700 GMT.*

EARLY FORECAST				REVISED FORECAST			
Amount (in.)	Prefigurence	Post-Agreement	Threat Score	Amount (in.)	Prefigurence	Post-Agreement	Threat Score
2.00	0.54	0.99	0.53	2.00	0.51	0.97	0.50
4.00	.55	.95	.53	4.00	.49	1.00	.49
6.00	.50	.92	.48	6.00	.56	1.00	.55
8.00	.39	.80	.35	8.00	.35	.95	.34
10.00	.09	.19	.06	10.00	.06	.19	.05
				12.00	0	0	0

TABLE 2.—*Average verification scores of forecast daily precipitation amounts (period ending 1200 GMT) for the storm of May 4–9, 1961. The Early Forecast refers to the one issued at approximately 1200 GMT and the revised to the one issued at 1700 GMT.*

EARLY FORECAST				REVISED FORECAST			
Amount (in.)	Prefigurence	Post-Agreement	Threat Score	Amount (in.)	Prefigurence	Post-Agreement	Threat Score
1.00	0.41	0.74	0.37	1.00	0.40	0.79	0.36
2.00	.19	.44	.15	2.00	.25	.73	.23
3.00	.01	.04	.01	3.00	.05	.18	.04
4.00	0	0	0	4.00	0	0	0

The averages of the daily scores for the same period (table 2) were, as might be expected, lower than the scores for the overall storm. In this particular 6-day period there was little difference in the scores between the Early Forecast and the Revised Forecast on either an overall storm basis or the daily average basis. However, a review of the monthly scores since October 1960 shows an average improvement in the threat score from the Early Forecast to the Revised Forecast for the 1-inch isohyetal of 0.07. This is a significant improvement and is a result of a more accurate description of the vertical motion and moisture fields at the beginning of the period through the use of 1200 GMT data, and the improved surface and upper-air prognosis possible over a shorter time period.

It is encouraging that the QPF's based on the semi-objective use of warm air advection and precipitable water have been as satisfactory as they have. Further progress may be expected as numerical methods increase their contribution to more refined prognostics.

ACKNOWLEDGMENTS

Thanks are expressed to Jane M. Violett for assistance in the preparation of figures and verification scores used in this article, and to Harlan K. Saylor for helpful comments and suggestions.

THE WEATHER AND CIRCULATION OF SEPTEMBER 1961

Including a Discussion of Tropical Storm Activity

CLIFTON F. TISDALE

Extended Forecast Branch, U.S. Weather Bureau, Washington, D.C.

1. INTRODUCTION

September 1961 was characterized by pronounced temperature regimes in the United States—very cool in the West and unusually warm in the East. This pattern of temperature was an abrupt change from that which prevailed in August and the summer season 1961 [1]. The most dramatic change occurred in the Northwest where temperatures during September averaged as much as 12° F. cooler than those observed in August.

This reversal in temperature regimes was associated with a pronounced reversal in the circulation, with the strong ridge over western North America during August being replaced by a deep trough in September. Substantial amounts of precipation fell in the Northern Plains as a result of this circulation reversal, thus alleviating the severe drought in that area.

Four tropical storms developed in the Atlantic and western Caribbean early in September, in marked contrast to the single storm which formed in these areas during the previous three months of the 1961 hurricane season. All four storms developed to full hurricane intensity and dominated weather headlines during the entire month.

2. MONTHLY MEAN CIRCULATION AND WEATHER

A strong upper-level ridge developed in the eastern Pacific in September where 700-mb. heights were as much as 280 ft. above normal (fig. 1). This anticyclogenesis appeared to have a marked influence in shaping the general location and amplitudes of the downstream trough-ridge systems across North America to Europe.

The trough which is normally present along the west coast of the United States in September [2] was much farther east and extended from a deeper-than-normal primary Low over Baffin Island southwestward across central Canada and the western United States (fig. 1). This was associated with shearing of the mean trough which dominated eastern North America during August (fig. 1 of [1]). The higher-latitude portion of this trough deepened as it advanced eastward to the central and eastern Atlantic in September. Concomitant with these trough developments was the strong anticyclogenesis which took place over eastern North America and central Europe, where 700-mb. heights were as much as 180 ft. above September normals. The resulting planetary-wave pattern at 700 mb. in September 1961 consisted of well-defined trough and ridge systems from the central Pacific eastward to Eurasia. This feature is well indicated by the height departures from normal (dotted lines in fig. 1).

The pattern over the eastern Pacific and North America is of special interest since it represents a complete reversal of those circulation features which had dominated this portion of the Northern Hemisphere during August and most of the summer season (see fig. 6A of [1]). Thus the trough in the East was supplanted by a ridge and the exceptionally strong ridge in the West was replaced by a deep trough in September. This circulation upheaval is clearly indicated by the 700-mb. anomalous height changes from August to September (fig. 2). The large height falls over the West and the extensive positive changes in the eastern Pacific are especially noteworthy. The month of September was one of generally low zonal index conditions over the United States with strong meridional flow resulting in unseasonable temperature extremes in many parts of the country.

The well-defined temperature and precipitation patterns for the month of September (fig. 3) are easily related to the monthly mean 700-mb. height and anomaly patterns (fig. 1). Temperatures averaged from 2° to 8° F. below normal over nearly the entire western two-thirds of the Nation under below normal heights and strong cyclonic flow. Note the almost perfect correspondence between the temperature and 700-mb. height anomaly patterns in the West (figs. 1, 3A). Average temperatures in the Northwest changed by as much as four class intervals[1] from August to September (fig. 4), highlighting the dramatic temperature reversal which occurred in this area. It was the coolest September of record at Glasgow, Mont., Albuquerque, N. Mex., Bismarck, N. Dak., and Grand Junction, Colo.

Temperatures over the eastern third of the Nation averaged from 2° to 6° F. above normal under the influence of above normal 700-mb. heights and strong anticyclonic conditions. This warming was especially note-

[1] Of a maximum possible 4-class change ranging from much above to much below normal.

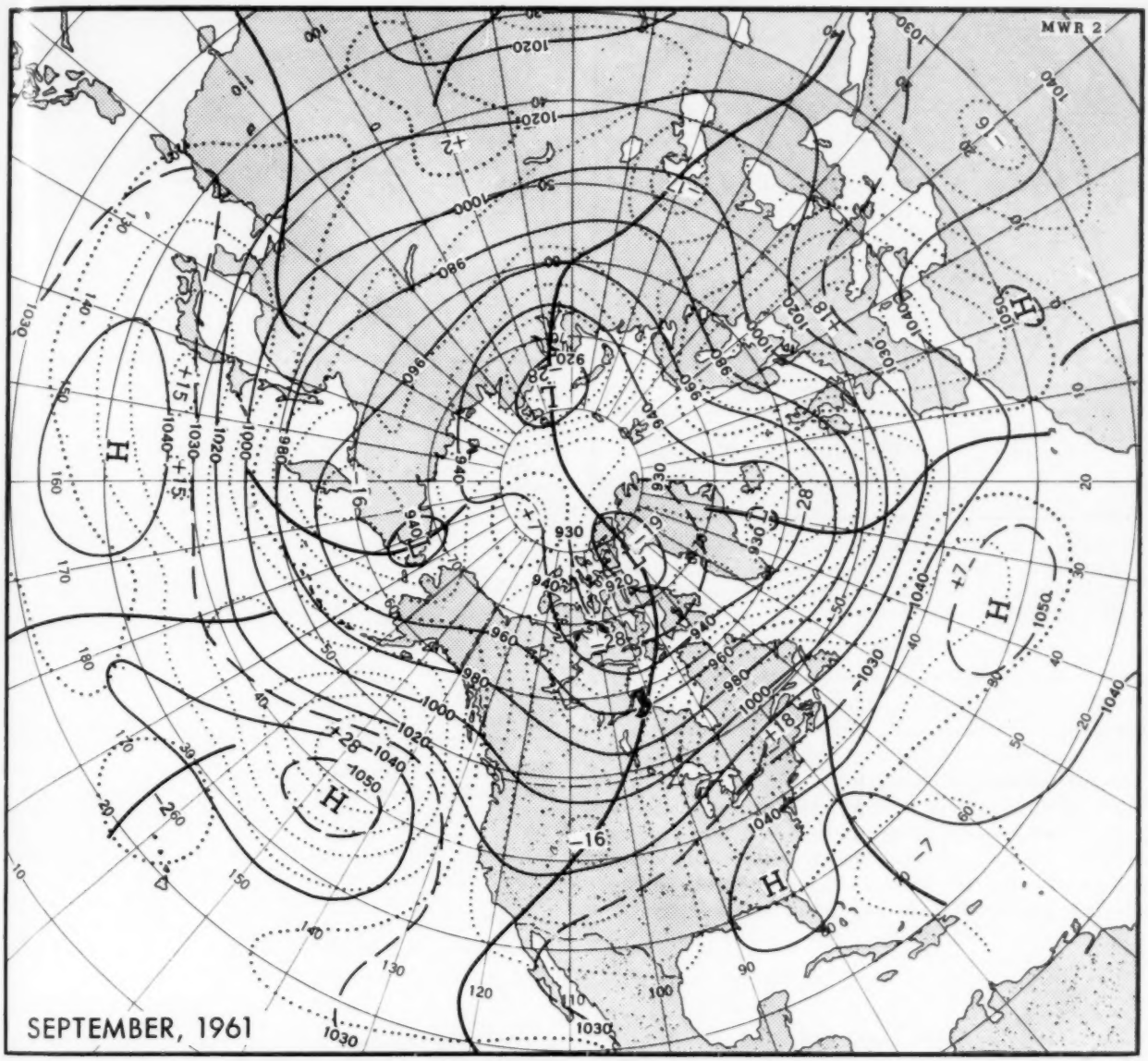

FIGURE 1.—Mean 700-mb. contours (solid) and height departures from normal (dotted) (both in tens of feet) for September 1961. The predominance of meridional flow from the central Pacific eastward to Eurasia is especially noteworthy.

TABLE 1.—*Monthly mean high temperature records established in September 1961*

Station	Temperature (°F.)		Remarks
	Average monthly	Departure from normal	
New Haven, Conn.	70.2	+6.6	warmest of record (1873)*
Concord, N.H.	67.1	+8.3	warmest of record (1881)*
Burlington, Vt.	65.4	+5.5	warmest since 1884
Binghamton, N.Y.	69.2	+6.7	warmest of record (1891)*
Buffalo, N.Y.	68.6	+6.2	warmest since 1881
New York City (Met. Obs., Central Park)	73.6	+5.3	warmest since 1869
Baltimore, Md.	76.7	+6.3	warmest of record (1881)*

*Denotes year records began.

worthy in some areas of the Southeast where monthly temperatures had averaged below normal since April. Sections of the Northeast experienced their warmest weather of 1961 this September, with near to record high average monthly temperatures reported at many locations (table 1).

Heavy precipitation fell from the southern Plains northeastward to the western Lakes Region in association with the deep trough in the West and strong southerly anomalous flow from the Gulf of Mexico (figs. 1, 3B). Most of this precipitation resulted from tropical storm Carla early in the month and from frequent frontal rains associated

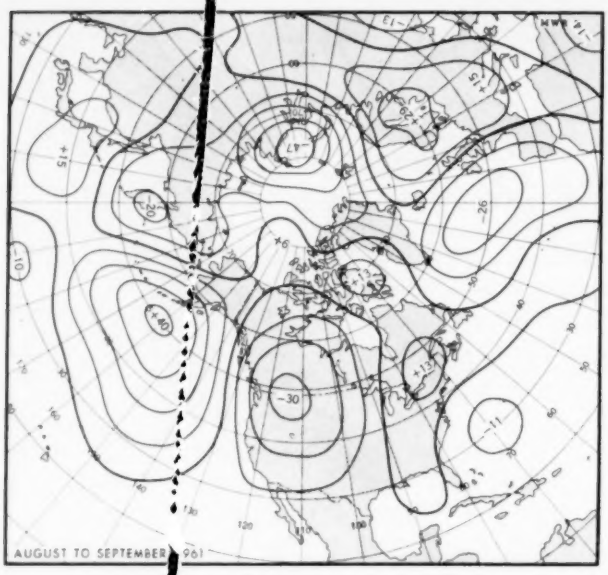

FIGURE 2.—Change in 700-mb. height departures from normal (tens of feet) from August 1961 to September 1961. Note the large height rises in the eastern Pacific and the corresponding height falls over western North America.

with strong thermal gradients in the mid-United States. Substantial precipitation amounts were also recorded from the northern Plains States southwestward across much of the central and western Rocky Mountain region (fig. 3B). This precipitation was also related to the deep trough over the West and occurred in conjunction with strong frontal systems which moved across the area at frequent intervals during the month. The heavy amounts in North Dakota and eastern Montana were especially beneficial, helping to alleviate general drought conditions in these areas. It was the wettest September of record in many sections of the Midwest (table 2).

Rainfall over much of the eastern third of the Nation was light (fig. 3B) as a result of the strong upper-level ridge which dominated the area (fig. 1). However, heavier amounts in extreme northeastern coastal sections resulted from tropical storm Esther during the latter part of the month. It was the driest September of record at Miami Beach, Fla., and at Knoxville, Tenn., as well as being notably dry at Greensboro, N.C. and Binghamton, N.Y.

TABLE 2.—*Heavy precipitation records established in September 1961.*

Station	Precipitation (in.)		Year records began
	Monthly total	Excess over normal	
Dubuque, Iowa	13.13	8.95	1905
Muskegon, Mich.	8.54	5.20	1905
Grand Rapids, Mich.	9.15	5.71	1904
Peoria, Ill.	13.09	9.36	1856
St. Joseph, Mo.	9.74	5.45	1910
Denver, Colo.	4.67	3.59	1871

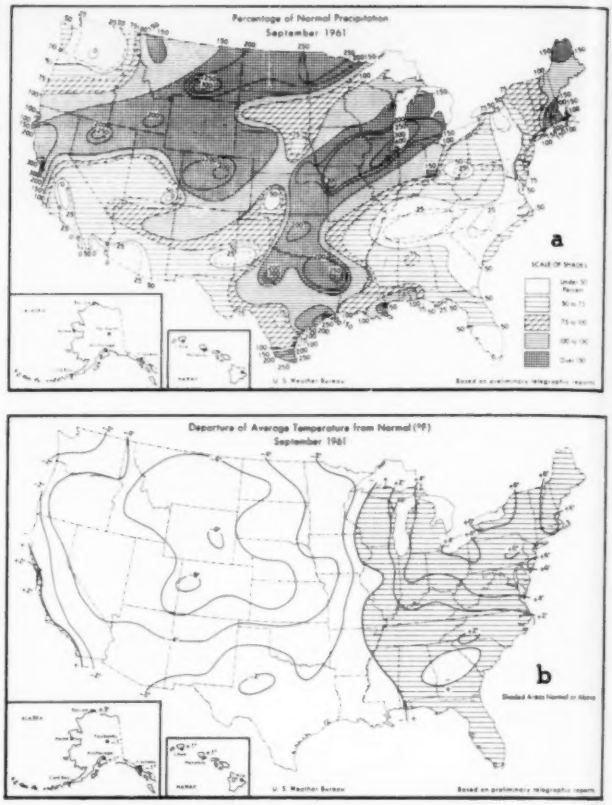

FIGURE 3.—(A) Departure of average surface temperature from normal (° F.) for September 1961. The pattern is noteworthy for the sharp demarcation between below-normal temperatures in the West (unshaded) and above-normal temperatures in the East (hatched). (B) Percentage of normal precipitation for September 1961. (From [9]).

3. TROPICAL STORMS RELATED TO THE MONTHLY CIRCULATION

ATLANTIC AND CARIBBEAN

Four tropical storms formed in the Atlantic and western Caribbean this September (fig. 5), all of which developed to full hurricane intensity. This is above the mean September frequency of three storms with two of hurricane intensity [3].

The month's circulation (fig. 1), from the central Atlantic to Europe, was apparently extremely favorable for storm formation in the eastern Atlantic, where three-fourths of the month's developments occurred. The pattern of 700-mb. height anomaly over the Atlantic and Europe resembled the circulation features in these areas found by Ballenzweig [4] as favoring tropical storm development in the eastern Atlantic.

The meridional character of the September circulation was also favorable for the transport of cooler-than-normal mid-tropospheric temperature and cyclonic vorticity into the Tropics, factors suggested by Namias [5] as conducive

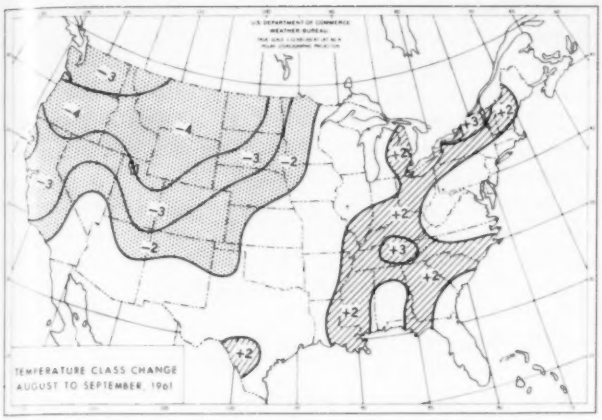

FIGURE 4.—Number of classes the anomaly of surface temperature changed from August to September 1961. Areas where the anomaly in September was two or more classes warmer are hatched; two or more classes cooler, stippled. The pattern represents a complete reversal in temperature regimes over the country from August to September.

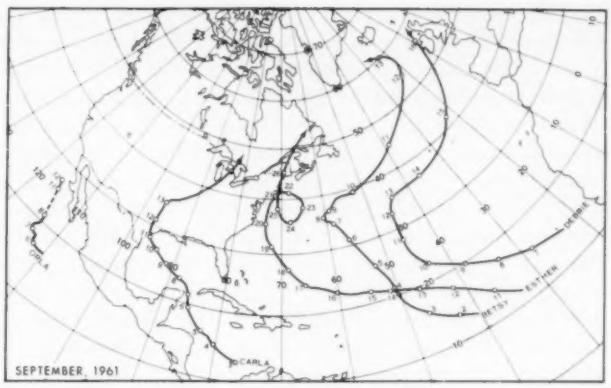

FIGURE 5.—Preliminary tracks of tropical storms during September 1961 in the Atlantic and eastern Pacific Oceans. Open circles and dates indicate 1200 GMT positions.

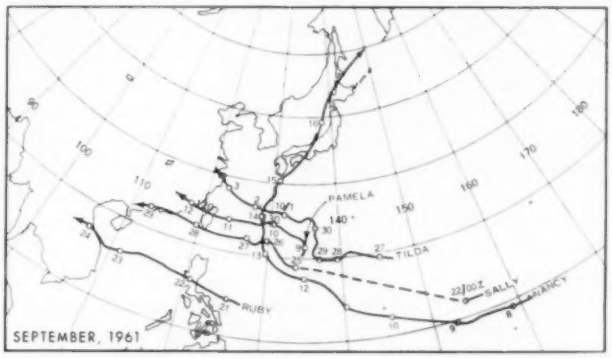

FIGURE 6.—Preliminary tracks of tropical storms during September 1961 in the western Pacific Ocean. Open circles and dates indicate 1200 GMT positions.

to storm formation, as well as allowing for a considerable degree of interaction between tropical and temperate-latitude activity.

The behavior of the tropical storms (fig. 5) can be interpreted, but only to a rather limited degree, in terms of the monthly mean circulation (fig. 1). The track of hurricane Betsy is fairly well indicated by the mean flow with the storm moving northwestward and then east-northeastward around the mean High in the eastern Atlantic. The motion of storm Carla, from the western Caribbean northwestward to southeastern Texas and then northeastward to the Lakes region follows the mean flow quite closely. The behavior of hurricane Debbie, however, is not well related to the monthly mean circulation, with the storm actually moving northwestward into and through west-central portions of the mean High in the eastern Atlantic.

The track of Esther, from the 11th to the 19th, parallels the mean flow across the South Atlantic with but little variation. The storm moved northward from the 20th to the 21st, then turned eastward and performed a complete loop which in four day's time brought it back to its original position off the southern New England coast (fig. 5). The mean Low and inverted trough off the east coast are, in major part, merely the reflection of hurricane Esther, the circulation of which dominated this area for over a week.

EASTERN PACIFIC

Tropical storm Orla, the only storm to develop in the eastern Pacific this September, was first detected on the 6th about 500 miles south of Baja California. The storm moved northwestward, as implied by the monthly mean flow, until the 8th when rapid disorganization of the circulation occurred. Weak remnants of the storm apparently continued northwestward to just west of Baja California where regeneration to tropical storm intensity occurred early on the 11th. Orla eventually dissipated on September 12 after moving only a short distance more to the northwest.

WESTERN PACIFIC

Five tropical storms were observed in this area during the month, four of which developed to typhoon intensity (fig. 6). This corresponds with a mean September frequency of five storms [3].

The monthly mean circulation in the Pacific was also apparently quite favorable for tropical developments this September, with the 700-mb. height anomaly pattern corresponding extremely well with the pattern suggested by Orgill [6] as favoring maximum typhoon development in the western Pacific.

Typhoon Nancy developed in the south-central Pacific on September 8 and moved west-northwestward with the mean flow until the 13th. The storm turned northward on the 13th and accelerated rapidly toward the north-

northeast, crossing central Japan by the 16th. This was the most devastating typhoon in the Pacific thus far this year. Maximum sustained winds well in excess of 200 m.p.h. were reported by aircraft on the 12th and 13th. Winds of 109 m.p.h. buffeted central Japan as the storm passed through the area on the 16th. This was the fastest moving storm ever to strike the main Japanese Islands. Its speed of translation was 31 m.p.h. when it crossed Honshu, increasing to over 50 m.p.h. as it moved into the Japan Sea. Typhoon Pamela was first detected south of Japan early on September 9. The storm moved west-northwestward as implied by the mean flow, crossing northern Formosa late on the 11th and eventually dissipating over eastern China on the 12th. Pamela was also a severe storm with winds up to 200 m.p.h. reported on the 11th. Tropical storm Ruby formed just southeast of Luzon in the Philippines on September 21. It moved west-northwestward with the mean flow, crossing central Luzon on the 22d. The storm then sped westward across the South China Sea, moving inland over Indo-China on the 24th without ever attaining typhoon intensity. The initial disturbance which eventually generated typhoon Sally was first detected well east of the Philippines on September 22. Because of the sparsity of data it was not picked up again until the 25th (dashed portion of track in fig. 6). It reached full typhoon intensity on the 26th just to the east of Formosa. The storm moved westward, brushing the extreme southern tip of Formosa early on the 28th, and dissipated over southeastern China on the 29th. Typhoon Tilda developed southeast of Japan on the 27th and 28th. This storm moved on a general west-northwestward track with the mean flow, passing just south of Okinawa early on October 2, and eventually moved inland into eastern China on the 4th.

4. TROPICAL STORMS RELATED TO THE 5-DAY MEAN CIRCULATION

The relation of the tropical storms of the Atlantic to the 5-day mean circulation is deserving of special attention this September, since their respective motions often were not readily apparent in the monthly mean circulation. Segments of each storm track corresponding to the period of each of a selected series of 700-mb. 5-day mean maps are reproduced in figure 7.

Conditions which attend and foster tropical storm development in the eastern Atlantic are usually shrouded in considerable uncertainty, because of the lack of data. The three developments in this area during September were not exceptions. A survey of 6-hourly surface charts revealed a considerable amount of thunderstorm and squall line activity over western Africa from late August into the early part of September. This activity probably developed in response to a trough of large amplitude which settled over the extreme eastern Atlantic during the latter part of August and which persisted through the first week of September (fig. 7A). Whether or not the initial disturbances which eventually evolved into hurricanes Betsy, Debbie, and Esther originated from these convective systems is conjectural, but there is some evidence in support of this possibility.

Tropical storm Betsy was first detected in the south-central Atlantic on September 2. The storm reached hurricane intensity on the 3d and moved northwestward to the mean trough position in the west-central Atlantic by the 6th (fig. 7A). Betsy slowly recurved in this trough area from the 7th to the 9th (fig. 7B) and then accelerated rapidly east-northeastward in the strong flow around the mean Low over southern Greenland (fig. 7B).

Hurricane Carla, one of the major storms of this century to threaten Gulf coastal areas, originated from an area of squally weather which was observed moving through the Windward Island group on the last day of August. This activity moved westward, with a weak circulation developing in the southwestern Caribbean northeast of Panama on September 3. The storm moved northwestward and had intensified to full hurricane strength just east of Yucatan by the 6th (fig. 7A). Moving northward through the Yucatan Channel during the 7th, Carla then turned west-northwestward and crossed the central Gulf of Mexico, striking the Texas coast on the 11th (fig. 7B). Rapid progression of the planetary wave train occurred over the United States at this time with the trough in the West (fig. 7B) advancing eastward to the Lakes region (fig. 7C). Carla turned sharply northward during the afternoon of the 11th, and moved up along the mean trough to northern Michigan from the 12th to the 14th (fig. 7C).

Hurricane force winds were reported from Galveston to Corpus Christi, Tex., a distance of approximately 200 miles, with winds in gusts in excess of 150 m.p.h. estimated at some coastal locations. The storm released 10 to 16 in. of rain along the first 50 miles of its path into southeastern Texas and also caused extensive flooding in many areas along the remainder of its track from Oklahoma to Michigan. In spite of the great size and severity of Carla, loss of life was held to a minimum by timely advices and evacuations, with an estimated 500,000 persons seeking safety inland from the low coastal areas and islands of Louisiana and Texas. Preliminary reports indicate about 46 fatalities, approximately half of which can be attributed to tornados and floods associated with the storm. The reader is referred to the *Weekly Weather and Crop Bulletin National Summary* [7] for a preliminary report on hurricane Carla.

Storm Debbie was first detected as an area of squally weather just west of the Cape Verde Islands on September 7 (fig. 7B). Surface data in the eastern Atlantic was sparse, with the storm position and intensity uncertain during the 8th and 9th. The storm's position on the 10th, however, was verified by TIROS III photographs. Debbie reached hurricane proportions late on the 10th and began recurving to the north in response to the progression of the mean trough from the western to the central Atlantic (figs. 7B, C). Eventual complete recurvature

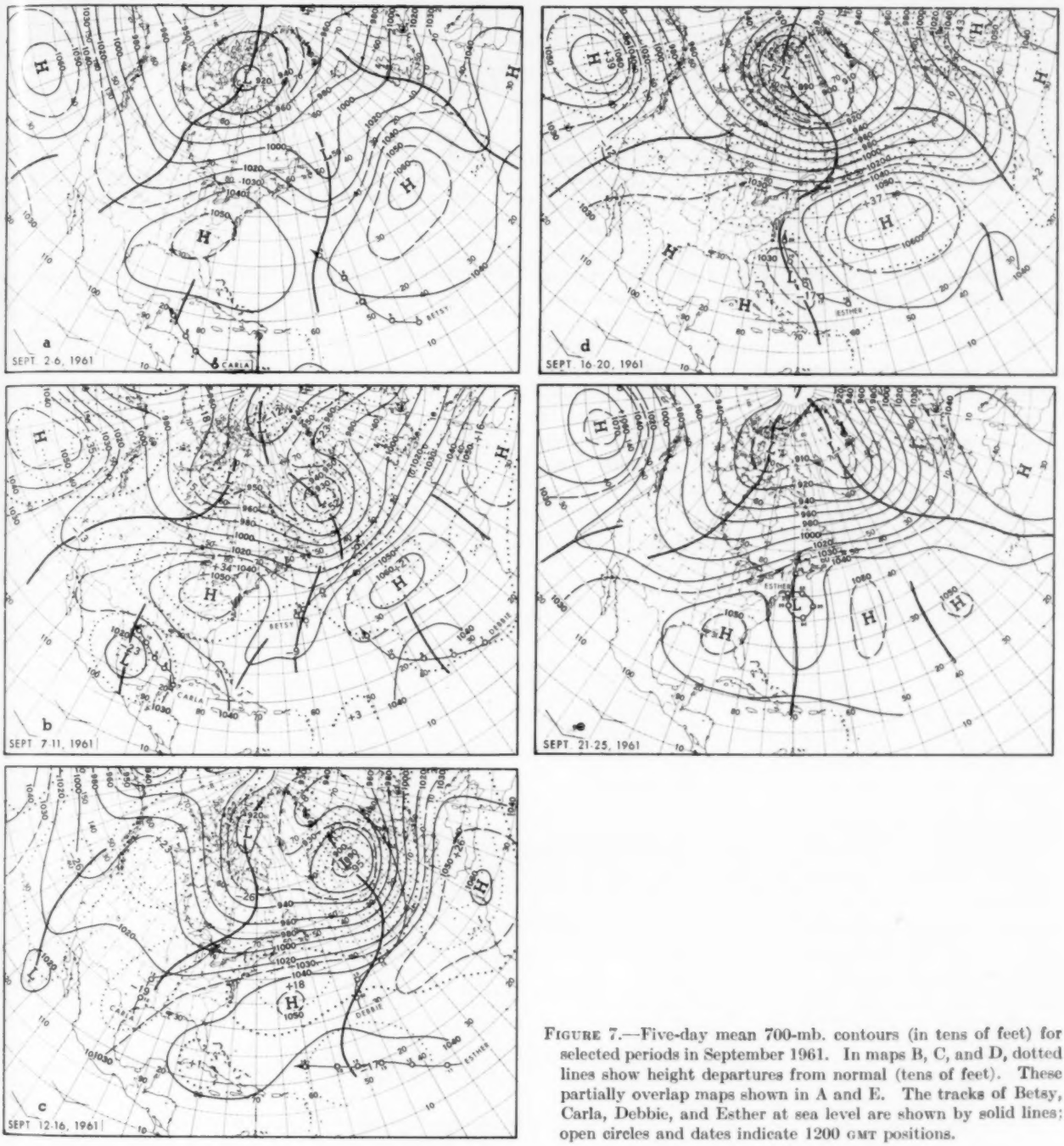

FIGURE 7.—Five-day mean 700-mb. contours (in tens of feet) for selected periods in September 1961. In maps B, C, and D, dotted lines show height departures from normal (tens of feet). These partially overlap maps shown in A and E. The tracks of Betsy, Carla, Debbie, and Esther at sea level are shown by solid lines; open circles and dates indicate 1200 GMT positions.

and rapid northeastward motion along and in advance of this trough occurred from the 12th to the 16th, with the storm causing considerable damage over Ireland as an intense extratropical system on the 16th.

Hurricane Esther was first detected when the weather satellite TIROS III on the afternoon of September 10 photographed a suspicious cloud area near 11° N., 30° W. Additional TIROS pictures and ship reports confirmed the existence of the storm on the 11th, with Esther having developed to full hurricane intensity when reconnaissance aircraft first entered the area on the 12th. This was the first hurricane discovered by means of a weather

satellite. The storm moved on a general west-northwestward track with the mean flow from the 12th to 16th (fig. 7C). Possible recurvature of Esther northward along the trough in the central Atlantic was apparently precluded by a strong ridge settling north of the storm (figs. 7C, D). This severe storm, with winds up to 140 m.p.h. accordingly continued to move west-northwestward, gradually turning to the north just east of Cape Hatteras on the 20th in the weak trough area along the east coast (fig. 7D). Moving north-northeastward, Esther approached Nantucket Island early on the 21st with gradually diminishing intensity. The storm then turned sharply eastward south of the Island, and by the afternoon of the 21st winds of barely tropical storm force were being reported. The unusually large, clockwise looping path of the storm, from the 22d to the 26th, occurred in a trough area (fig. 7E) which was, in major part, shaped by the storm's circulation. An influx of cool, dry air from mid-continent coupled with the notably cold ocean surface off New England may have been instrumental in causing the rapid diminution of storm intensity which occurred on the 21st. The *Weekly Weather and Crop Bulletin, National Summary* [8] contains a preliminary report on hurricane Esther.

REFERENCES

1. J. F. Andrews, "The Weather and Circulation of August 1961—Record Heat from the Northern Plains to the Pacific Coast," *Monthly Weather Review*, vol. 89, No. 11, Nov. 1961, pp. 495-500.
2. U.S. Weather Bureau, "Normal Weather Charts for the Northern Hemisphere," *Technical Paper* No. 21, Washington, D.C., 1952, 74 pp.
3. G. E. Dunn, "Tropical Cyclones," *Compendium of Meteorology*, American Meteorological Society, Boston, 1951, pp. 887–901.
4. E. M. Ballenzweig, "Relation of Long-Period Circulation Anomalies to Tropical Storm Formation and Motion," *Journal of Meteorology*, vol. 16, No. 2, Apr. 1959, pp. 121–139.
5. J. Namias, "Long-Range Factors Affecting the Genesis and Paths of Tropical Cyclones," *Proceedings of the UNESCO Symposium on Typhoons, Tokyo, 9–12 November 1954*, 1955, pp. 213–219.
6. M. M. Orgill, "An Investigation into the Relationship of Monthly Circulation Indices and Anomalies to Typhoon Development (In the Western Pacific)," *Scientific Report* No. 2, on Contract No. AF 19(604)–7229, August 1960, 42 pp.
7. U.S. Weather Bureau, *Weekly Weather and Crop Bulletin, National Summary* vol. XLVIII, No. 38, September 18, 1961 (Hurricane Carla, a preliminary report).
8. U.S. Weather Bureau, *Weekly Weather and Crop Bulletin, National Summary*, vol. XLVIII, No. 39, September 25, 1961, (Hurricane Esther, a preliminary report).
9. U.S. Weather Bureau, *Weekly Weather and Crop Bulletin, National Summary*, vol. XLVIII, Nos. 40–41, October 2, 9, 1961.

CONTENTS, VOLUME 89

NUMBER 1 **JANUARY 1961**

Use of Doppler Radar in Meteorological Observations — Robert L. Smith and David W. Holmes — 1–7
New Weather Bureau Publication — 7
Publications by Weather Bureau Authors — 8
Rainstorm in Southern Florida, January 21, 1957 — Robert H. Sourbeer and R. Cecil Gentry — 9–16
Weather Notes
Radar Echo of a Mountain Wave on February 15, 1960 — DeVer Colson, Charles V. Lindsay, and James H. Hand — 17–19
Tornadoes Near Nags Head, N.C., in May and June 1960 — Frank B. Dinwiddie — 20–23
The Weather and Circulation of October 1960 — James F. Andrews — 24–30
Correction — 19

NUMBER 2 **FEBRUARY 1961**

The Precipitation Day Statistic — C. K. Vestal — 31–37
Weather Bureau Technical News — 38
A Study of the Effect of Tree Leaves on Wind Movement — Ralph H. Frederick — 39–44
Description of the 50-mb. Patterns over Antarctica in 1958 — N. J. Ropar and T. I. Gray, Jr. — 45–52
New Weather Bureau Publication — 52
The Weather and Circulation of November 1960—Another November With a Mid-Month Reversal. — James F. O'Connor — 53–58

NUMBER 3 **MARCH 1961**

A Proposed Staggered-Grid System for Numerical Integration of Dynamic Equations — D. K. Lilly — 59–65
Publications by Weather Bureau Authors — 66
New Weather Bureau Publication — 66
Diagnosis of Divergence in a Three-Parameter Numerical Prediction Model — A. Wiin-Nielsen — 67–73
A Diagnostic Study of Mid-Tropospheric Development — George P. Cressman — 74–82
Case Studies of Numerical Wind Analyses — John A. Brown, Jr. and James R. Neilon — 83–90
A Note on Clear Air Turbulence During April and May 1960 — Frank J. Smigielski — 91–93
Analysis of Clear Air Turbulence During April 1960 — DeVer Colson — 94–98
Recent Articles in Other Weather Bureau Periodicals — 98
The Hurricane Season of 1960 — Gordon E. Dunn — 99–108
The Weather and Circulation of December 1960—An Unusually Cold Month in the United States — Robert H. Gelhard — 109–114

NUMBER 4 **APRIL 1961**

The Reduction of Truncation Error by Extrapolation Techniques — W. Lawrence Gates — 115–124
Time Section and Hodograph Analysis of Churchill Rocket and Radiosonde Winds and Temperatures — Sidney Teweles — 125–136
The Weather and Circulation of January 1961 — Raymond A. Green — 137–143
Weather Bureau Technical News — 144
Suggestions for Authors — 145
Publication of Weather Notes — 146

NUMBER 5 **MAY 1961**

Normal Heat Sources and Sinks in the Lower Troposphere in Winter — Philip F. Clapp — 147–162
Lee-Side Frontogenesis in the Rocky Mountains — Toby N. Carlson — 163–172
Some Aspects of the Thermal Energy Exchange on the South Polar Snowfield and Arctic Ice Pack — Kirby J. Hanson — 173–177
The Weather and Circulation of February 1961—An Example of Attenuation in the Long-Wave Pattern — L. P. Stark — 178–184
Publications by Weather Bureau Authors — 185
New Weather Bureau Publication — 186
Recent Articles in Other Weather Bureau Periodicals — 186

NUMBER 6 **JUNE 1961**

Computation and Uses of Gradient Winds ... Roy M. Endlich 187–191
Graphical Solution of the Penman Equation for Potential Evapotranspiration ... John C. Purvis 192–196
On Verification of Upper-Air Winds by Vertical Shear and Extremes ... Oskar M. Essenwanger, Robert E. Bradford, and William W. Vaughan 197–204
The Weather and Circulation of March 1961—Another Mild Month in the United States ... James F. Andrews 205–210

NUMBER 7 **JULY 1961**

Mean Circulation Patterns Based on 12 Years of Recent Northern Hemispheric Data ... James F. O'Connor 211–227
Publications by Weather Bureau Authors ... 228
A Southern Hemisphere Case Study with TIROS I Data ... Lester F. Hubert 229–242
Forecasting Precipitation with the Aid of a High-Speed Electronic Computer ... Joseph Vederman 243–250
Relative Motion of Hurricane Pairs ... Eugene W. Hoover 251–255
The Weather and Circulation of April 1961—Persistent Blocking in Eastern Canada and Cool Weather in the United States ... James F. O'Connor 256–262

NUMBER 8 **AUGUST 1961**

Some Experiments on the Measurement of Natural Ice Nuclei ... Dwight B. Kline and Glenn W. Brier 263–272
Estimation of Vertical Air Motions in Desert Terrain from Tetroon Flights ... J. K. Angell and D. H. Pack 273–283
Recent Articles in Other Weather Bureau Periodicals ... 284
Accuracy of the Airborne Economical Radiometer ... P. M. Kuhn 285–287
Publications by Weather Bureau Authors ... 288
Tropospheric Ozone: An Air Pollution Problem Arising in the Washington, D.C. Metropolitan Area ... R. C. Wanta, W. B. Moreland, and H. E. Heggestad 289–296
Correspondence
The Probing of the Tropopause by Balloons That Follow It—A Suggestion ... Wan-Cheng Chiu 297–298
The Weather and Circulation of May 1961—Persistent Cool Weather in the United States ... Robert H. Gelhard 299–305
Suggestions for Authors ... 306

NUMBER 9 **SEPTEMBER 1961**

Some Aspects of a Cycle of Available Potential Energy ... Jay S. Winston and Arthur F. Krueger 307–318
Low-Level Inversion Frequency in the Contiguous United States ... Charles R. Hosler 319–339
Weather Note
The Effect of Differential Friction Between Land and Water on the Movement of Donna in the Vicinity of Eastern North Carolina ... Eugene W. Hoover 340
Moisture and Cotton at Harvest Time in the Mississippi Delta ... J. A. Riley 341–353
Weather Note
The "Double Eye" of Hurricane Donna ... C. L. Jordan and Lt. Frank J. Schatzle 354–356
Distributions of Weekly Averages of Diurnal Temperature Means and Ranges About Harmonic Curves ... Christopher Bingham 357–367
The Weather and Circulation of June 1961—A Hot, Dry Month in the West ... L. P. Stark 368–373
Weather Bureau Technical News ... 373
Publications by Weather Bureau Authors ... 374

NUMBER 10 **OCTOBER 1961**

Cloud Streets Over the Caribbean Sea ... John Schuetz and Sigmund Fritz 375–382
A Western Atlantic Vortex Seen by TIROS I ... J. B. Jones 383–390
Behavior of the Principal Harmonics of Selected 5-Day Mean 500-mb. Charts ... Robert L. Haney 391–396
Relative Catches of Snow in Shielded and Unshielded Gages at Different Wind Speeds ... Leonard L. Weiss 397–400
A Comparison of Methods for Computing Daily Mean Values of Dry Bulb Temperature, Dew Point, and Relative Humidity ... Milton L. Blanc 401–410
Weather Note
Squall Line Passage at Barrow, Alaska, June 21, 1960 ... Ronald J. McCue, Jr., and G. Philip Weber 411–413
The Weather and Circulation of July 1961 ... Raymond A. Green 414–418

NUMBER 11 NOVEMBER 1961

Analysis of Satellite Infrared Radiation Measurements on a Synoptic Scale.
Melvin Weinstein and Verner E. Suomi 419–428
Satellite Pictures and Meteorological Analyses of a Developing Low in the Central United States.
Andrew Timchalk and Lester F. Hubert 429–445
New Weather Bureau Publications 446
Another View from TIROS I of a Severe Weather Situation—May 16,1960 Linwood F. Whitney, Jr. 447–460
On Short- and Long-Term Variations in Quasi-Barotropic Flow A. Wiin-Nielsen 461–476
The Nashville Daily Air Pollution Forecast Carl M. Boettger and Harold J. Smith 478–481
The Occurrence of Anomalous Winds and Their Significance M. A. Alaka 482–494
The Weather and Circulation of August 1961—Record Heat from the Northern Plains to the Pacific Coast.
James F. Andrews 495–500
Weather Note
Excessive Rainfall in the Montgomery, Ala., Area on August 31, 1961 Arthur R. Long 501
Publications by Weather Bureau Authors 502
Recent Articles in Other Weather Bureau Periodicals 502

NUMBER 12 DECEMBER 1961

On the Radiative Equilibrium and Heat Balance of the Atmosphere Syukuro Manabe and Fritz Möller 503–532
Three-Dimensional Pressure Pattern of the Dallas Tornado and Some Resultant Implications.
Walter H. Hoecker, Jr. 533–542
Sunshine-Cloudiness Relationships in the United States Ray L. Fox 543–548
The Zonal Wind Field Along 80° W. for the IGY Period and Northern Hemisphere Anomalies of Wind and Temperature William M. McMurray 549–554
Weather Note
The Middle Mississippi Valley Hydrometeorological Storm of May 4–9, 1961.
Jerrold A. La Rue and Russell J. Younkin 555–559
The Weather and Circulation of September 1961—Including a Discussion of Tropical Storm Activity.
Clifton F. Tisdale 560–566
Contents, Volume 89 567–569
Corrections 569
Index, Volume 89 570–577
Recent Articles in Other Weather Bureau Periodicals 578

CORRECTION NOTICES

Vol. 88, Aug. 1960:

p. 290: Under section 4, the reference to the map of monthly mean circulation in line 2 should be to figure 7; the figure referred to in line 8 from the bottom of that column should be figure 6.

p. 291: In column 1, line 8, reference should be to figure 7.

INDEX, VOLUME 89

A

Accuracy of the airborne economical radiometer. (2 figs.) P. M. Kuhn. 285–287.

Agricultural meteorology:
Moisture and cotton at harvest time in the Mississippi Delta. (9 figs.) J. A. Riley. 341–353.

Air pollution:
The Nashville daily air pollution forecast. (6 figs.) Carl M. Boettger and Harold J. Smith. 477–481.
Tropospheric ozone: An air pollution problem arising in the Washington, D.C. metropolitan area. (11 figs.) R. C. Wanta, W. B. Moreland, and H. E. Heggestad. 289–296.

ALAKA, M. A.:
The occurrence of anomalous winds and their significance. (13 figs.) 482–494.

Alaska:
Squall line passage at Barrow, Alaska, June 21, 1960. (4 figs.) [Weather Note] Ronald J. McCue, Jr. and G. Philip Weber. 411–413.

Analysis of clear air turbulence during April 1960. (4 figs.) DeVer Colson. 94–98.

Analysis of satellite infrared radiation measurements on a synoptic scale. (11 figs.) Melvin Weinstein and Verner E. Suomi. 419–428.

ANDREWS, J. F.:
The weather and circulation of October 1960. (11 figs.) 24–30.
The weather and circulation of March 1961—Another mild month in the United States. (11 figs.) 205–210.
The weather and circulation of August 1961—Record heat from the northern Plains to the Pacific coast. (6 figs.) 495–500.

ANGELL, J. K.:
and D. H. Pack. Estimation of vertical air motions in desert terrain from tetroon flights. (13 figs.) 273–283.

Another view from TIROS I of a severe weather situation—May 16, 1960. (13 figs.) Linwood F. Whitney, Jr. 447–460.

Antarctica:
Description of the 50-mb. patterns over Antarctica in 1958. (17 figs.) N. J. Ropar and T. I. Gray, Jr. 45–52.
Some aspects of the thermal energy exchange on the South Polar snowfield and Arctic ice pack. (3 figs.) Kirby J. Hanson. 173–177.

Arctic regions:
Some aspects of the thermal energy exchange on the South Polar snowfield and Arctic ice pack. (3 figs.) Kirby J. Hanson. 173–177.

Atmosphere. Circulation:
Behavior of the principal harmonics of selected 5-day mean 500-mb. charts. (13 figs.) Robert L. Haney. 391–396.
Description of the 50-mb. patterns over Antarctica in 1958. (17 figs.) N. J. Ropar and T. I. Gray, Jr. 45–52.
Mean circulation patterns based on 12 years of recent Northern Hemisphere data. (14 figs.) James F. O'Connor. 211–227.
The occurrence of anomalous winds and their significance. (13 figs.) M. A. Alaka. 482–494.
On short- and long-term variations in quasi-barotropic flow. (22 figs.) A. Wiin-Nielsen. 461–476.
Some aspects of a cycle of available potential energy. (9 figs.) Jay S. Winston and Arthur F. Krueger. 307–318.

B

Behavior of the principal harmonics of selected 5-day mean 500-mb. charts. (13 figs.) Robert L. Haney. 391–396.

BINGHAM, CHRISTOPHER:
Distributions of weekly averages of diurnal temperature means and ranges about harmonic curves. (6 figs.) 357–367.

BLANC, MILTON L.:
A comparison of methods for computing daily mean values of dry bulb temperature, dew point, and relative humidity. (10 figs.) 401–410.

BOETTGER, CARL M.:
and Harold J. Smith. The Nashville daily air pollution forecast. (6 figs.) 477–481.

BRADFORD, ROBERT E.:
and Oskar M. Essenwanger and William W. Vaughan. On verification of upper-air winds by vertical shear and extremes. (3 figs.) 197–204.

BRIER, GLENN W.:
and Dwight B. Kline. Some experiments on the measurement of natural ice nuclei. (7 figs.) 263–272.

BROWN, JOHN A.:
and James R. Neilon. Case studies of numerical wind analyses. (7 figs.) 83–90.

C

CARLSON, TOBY N.:
Lee-side frontogenesis in the Rocky Mountains. (13 figs.) 163–172.

Case studies of numerical wind analyses. (7 figs.) John A. Brown and James R. Neilon. 83–90.

CHIU, WAN-CHENG:
The probing of the tropopause by balloons that follow it—a suggestion. 297–298.
CLAPP, PHILIP F.:
Normal heat sources and sinks in the lower troposphere. (10 figs.) 147–162.
Clear air turbulence:
Analysis of clear air turbulence during April 1960. (4 figs.) DeVer Colson. 94–98.
A note on clear air turbulence during April and May 1960. (5 figs.) Frank J. Smigielski. 91–93.
Climatology:
Behavior of the principal harmonics of selected 5-day mean 500-mb. charts. (13 figs.) Robert L. Haney. 391–396.
A comparison of methods for computing daily mean values of dry bulb temperature, dew point, and relative humidity. (10 figs.) Milton L. Blanc. 401–410.
Distributions of weekly averages of diurnal temperature means and ranges about harmonic curves. (6 figs.) Christopher Bingham. 357–367.
Low-level inversion frequency in the contiguous United States. (9 figs.) Charles R. Hosler. 319–339.
Moisture and cotton at harvest time in the Mississippi Delta. (9 figs.) J. A. Riley. 341–353.
The precipitation day statistic. (5 figs.) C. K. Vestal. 31–37.
Sunshine-cloudiness relationships in the United States. (11 figs.) Roy L. Fox. 543–548.
The zonal wind field along 80° W. for the IGY period and Northern Hemisphere anomalies of wind and temperature. (8 figs.) William M. McMurray. 549–554.
Cloud streets over the Caribbean Sea. (8 figs.) John Schuetz and Sigmund Fritz. 375–382.
Clouds:
Another view from TIROS I of a severe weather situation—May 16, 1960. (13 figs.) Linwood F. Whitney, Jr. 447–460.
Cloud streets over the Caribbean Sea. (8 figs.) John Schuetz and Sigmund Fritz. 375–382.
Radar echo of a mountain wave on February 15, 1960. (4 figs.) [Weather Note] DeVer Colson, Charles V. Lindsay, and James H. Hand. 17–19.
Satellite pictures and meteorological analyses of a developing Low in the central United States. (17 figs.) Andrew Timchalk and Lester F. Hubert. 429–445.
A Southern Hemisphere case study with TIROS I data. (13 figs.) Lester F. Hubert. 229–242.
Sunshine-cloudiness relationships in the United States. (11 figs.) Roy L. Fox. 543–548.
A western Atlantic vortex seen by TIROS I. (7 figs.) J. B. Jones. 383–390.
COLSON, DEVER:
Analysis of clear air turbulence during April 1960. (4 figs.) 94–98.
and Charles V. Lindsay and James H. Hand. Radar echo of a mountain wave on February 15, 1960. (4 figs.) [Weather note] 17–19.
A comparison of methods for computing daily mean values of dry bulb temperature, dew point, and relative humidity. (10 figs.) Milton L. Blanc. 401–410.
Computation and uses of gradient winds. (1 fig.) Roy M. Endlich. 187–191.
Correspondence:
The probing of the tropopause by balloons that follow it—a suggestion. Wan-Cheng Chiu. 297–298.
CRESSMAN, GEORGE P.:
A diagnostic study of mid-tropospheric development. (13 figs.) 74–82.

D

Description of the 50-mb. patterns over Antarctica in 1958. (17 figs.) N. J. Ropar and T. I. Gray, Jr. 45–52.
Diagnosis of divergence in a three-parameter numerical prediction model. (5 figs.) A. Wiin-Nielsen. 67–73.
A diagnostic study of mid-tropospheric development. (13 figs.) George P. Cressman. 74–82.
DINWIDDIE, FRANK B.:
Tornadoes near Nags Head, N.C., in May and June 1960. (6 figs.) [Weather note] 20–23.
Distributions of weekly averages of diurnal temperature means and ranges about harmonic curves. (6 figs.) Christopher Bingham. 357–367.
The "double eye" of hurricane Donna. (3 figs.) [Weather note] C. L. Jordan and Frank J. Schatzle. 354–356.
DUNN, GORDON E.:
The hurricane season of 1960. (5 figs.) 99–108.

E

The effect of differential friction between land and water on the movement of Donna in the vicinity of eastern North Carolina. (1 fig.) [Weather note] Eugene W. Hoover. 340.
ENDLICH, ROY M.:
Computation and uses of gradient winds. (1 fig.) 187–191.
ESSENWANGER, OSKAR M.:
and Robert E. Bradford and William W. Vaughan. On verification of upper-air winds by vertical shear and extremes. (3 figs.) 197–204.
Estimation of vertical air motions in desert terrain from tetroon flights. (13 figs.) J. K. Angell and D. H. Pack. 273–283.

Evapotranspiration:
Graphical solution of the Penman equation for potential evapotranspiration. (3 figs.) John C. Purvis. 192–196.
Excessive rainfall in the Montgomery, Ala. area on August 31, 1961. [Weather note] Arthur R. Long. 501.

F

Forecasting precipitation with the air of a high-speed electronic computer. (7 figs). Joseph Vederman. 243–250.
Forecasts:
The Nashville daily air pollution forecast. (6 figs.) Carl M. Boettger and Harold J. Smith. 477–481.
Forecasts. Numerical:
Case studies of numerical wind analyses. (7 figs.) John A. Brown and James R. Neilon. 83–90.
Diagnosis of divergence in a three-parameter numerical prediction model. (5 figs.) A. Wiin-Nielsen. 67–73.
A diagnostic study of mid-tropospheric development. (13 figs.) George P. Cressman. 74–82.
Forecasting precipitation with the aid of a high-speed electronic computer. (7 figs.) Joseph Vederman. 243–250.
A proposed staggered-grid system for numercial integration of dynamic equations. (2 figs.) D. K. Lilly. 59–65.
The reduction of truncation error by extrapolation techniques. (5 figs.) W. Lawrence Gates. 115–124.
FOX, ROY L.:
Sunshine-cloudiness relationships in the United States. (11 figs.) 543–548.
FREDERICK, RALPH H.:
A study of the effect of tree leaves on wind movement. (4 figs.) 39–44.
FRITZ, SIGMUND:
and John Schuetz. Cloud streets over the Caribbean Sea. (8 figs.) 375–382.
Fronts:
Lee-side frontogenesis in the Rocky Mountains. (13 figs.) Toby Y. Carlson. 163–172.

G

GATES, W. LAWRENCE:
The reduction of truncation error by extrapolation techniques. (5 figs.) 115–124.
GELHARD, ROBERT H.:
The weather and circulation of December 1960—An unusually cold month in the United States. (10 figs.) 109–114.
The weather and circulation of May 1961—Persistent cool weather in the United States. (10 figs.) 299–305.
GENTRY, R. CECIL:
and Robert H. Sourbeer. Rainstorm in southern Florida, January 21, 1957. (8 figs.) [Weather note] 9–16.
Graphical solution of the Penman equation for potential evapotranspiration. (3 figs.) John C. Purvis. 192–196.
GRAY, T. I., JR.:
and N. J. Ropar. Description of the 50-mb. patterns over Antarctica in 1958. (17 figs.) 45–52.
GREEN, RAYMOND A.:
The weather and circulation of January 1961. (11 figs.) 137–143.
The weather and circulation of July 1961. (9 figs.) 414–418.

H

HAND, JAMES H.:
and DeVer Colson and Charles V. Lindsay. Radar echo of a mountain wave on February 15, 1961 (4 figs.) [Weather note] 17–19.
HANEY, ROBERT L.:
Behavior of the principal harmonics of selected 5-day mean 500-mb. charts. (13 figs.) 391–396.
HANSON, KIRBY J.:
Some aspects of the thermal energy exchange on the South Polar snowfield and Arctic ice pack. (3 figs.) 173–177.
Heat budget:
Normal heat sources and sinks in the lower troposphere. (10 figs.) Philip F. Clapp. 147–162.
On the radiative equilibrium and heat balance of the atmosphere. (26 figs.) Syukuro Manabe and Fritz Möller. 503–532.
Some aspects of the thermal energy exchange on the South Polar snowfield and Arctic ice pack. (3 figs.) Kirby J. Hanson. 173–177.
HEGGESTAD, H. E.:
and R. C. Wanta and W. B. Moreland. Tropospheric ozone: An air pollution problem arising in the Washington, D. C. metropolitan area. (11 figs.) 289–296.
HOECKER, WALTER H. JR.:
Three-dimensional pressure pattern of the Dallas tornado and some resultant implications. (9 figs.) 533–542.
HOLMES, DAVID W.:
and Robert L. Smith. Use of Doppler radar in meteorological observations. (9 figs.) 1–7.
HOOVER, EUGENE W.:
The effect of differential friction between land and water on the movement of Donna in the vicinity of eastern North Carolina. (1 fig.) [Weather note]. 340.
Relative motion of hurricane pairs. (7 figs.) 251–255.
HOSLER, CHARLES R.:
Low-level inversion frequency in the contiguous United States. (9 figs.) 319–339.

HUBERT, LESTER F.:
A Southern Hemisphere case study with TIROS I data. (13 figs.) 229–242.
and Andrew Timchalk. Satellite pictures and meteorological analyses of a developing Low in the central United States. (17 figs.) 429–445.
The hurricane season of 1960. (5 figs.) Gordon E. Dunn. 99–108.
Hurricanes:
The "double eye" of hurricane Donna. (3 figs.) [Weather note] C. L. Jordan and Frank. J. Schatzle. 354–356.
The effect of differential friction between land and water on the movement of Donna in the vicinity of eastern North Carolina. (1 fig.) [Weather note] Eugene W. Hoover. 340.
The hurricane season of 1960. (5 figs.) Gordon E. Dunn. 99–108.
The occurrence of anomalous winds and their significance. (13 figs.) M. A. Alaka. 482–494.
Relative motion of hurricane pairs. (7 figs.) Eugene W. Hoover. 251–255.
The weather and circulation of September 1961—Including a discussion of tropical storm activity. (7 figs.) Clifton F. Tisdale. 560–566.

I

Ice nuclei:
Some experiments on the measurement of natural ice nuclei. (7 figs.) Dwight B. Kline and Glenn W. Brier. 263–272.
Instruments:
Accuracy of the airborne economical radiometer. (2 figs.) P. M. Kuhn. 285–287.
Estimation of vertical air motions in desert terrain from tetroon flights. (13 figs.) J. K. Angell and D. H. Pack. 273–283.
The probing of the tropopause by balloons that follow it—A suggestion. Wan-Cheng Chiu. 297–298.
Relative catches of snow in shielded and unshielded gages at different wind speeds. (5 figs.) Leonard L. Weiss. 397–400.
International Geophysical Year:
The zonal wind field along 80° W. for the IGY period and Northern Hemisphere anomalies of wind and temperature. (8 figs.) William M. McMurray. 549–554.

J

JONES, J. B.
A western Atlantic vortex seen by TIROS I. (7 figs.) 383–390.
JORDAN, C. L.:
and Frank J. Schatzle. The "double eye" of hurricane Donna. (3 figs.) [Weather note] 354–356.

K

KLINE, DWIGHT B.:
and Glenn W. Brier. Some experiments on the measurement of natural ice nuclei. (7 figs.) 263–272.
KRUEGER, ARTHUR F.:
and Jay S. Winston. Some aspects of a cycle of available potential energy. (9 figs.) 307–318.
KUHN, P. M.:
Accuracy of the airbone economical radiometer. (2 figs.) 285–287.

L

LARUE, JERROLD A.:
and Russell J. Younkin. The middle Mississippi Valley hydrometeorological storm of May 4–9, 1961. (8 figs.) [Weather note] 555–559.
Lee-side frontogenesis in the Rocky Mountains. (13 figs.) Toby Y. Carlson. 163–172.
LILLY, D. K.:
A proposed staggered-grid system for numerical integration of dynamic equations. (2 figs.) 59–65.
LINDSAY, CHARLES V.:
and DeVer Colson and James H. Hand. Radar echo. of a mountain wave on February 15, 1960. (4 figs.) [Weather note] 17–19.
LONG, ARTHUR R.:
Excessive rainfall in the Montgomery, Ala. area on August 31, 1961. [Weather note] 501.
Low-level inversion frequency in the contiguous United States. (9 figs.) Charles R. Hosler. 319–339.

M

MANABE, SYUKURO:
and Fritz Möller. On the radiative equilibrium and heat balance of the atmosphere. (26 figs.) 503–532.
McCUE, RONALD J., JR.:
and G. Philip Weber. Squall line passage at Barrow, Alaska, June 21, 1960. (4 figs.) [Weather note] 411–413.
McMURRAY, WILLIAM M.:
The zonal wind field along 80°W. for the IGY period and Northern Hemisphere anomalies of wind and temperature. (8 figs.) 549–554.
Mean circulation patterns based on 12 years of recent Northern Hemisphere data. (14 figs.) James F. O'Connor. 211–227.
Micrometeorology:
A study of the effect of tree leaves on wind measurement. (4 figs.) Ralph H. Frederick 39–44.
The middle Mississippi Valley hydrometeorological storm of May 4–9, 1961. (8 figs.) [Weather note] Jerrold A. LaRue and Russell J. Younkin. 555–559.
Mississippi:
Moisture and cotton at harvest time in the Mississippi Delta. (9 figs.) J. A. Riley. 341–353.

MÖLLER, FRITZ:
and Syukuro Manabe. On the radiative equilibrium and heat balance of the atmosphere. (26 figs.) 503–532.
Moisture and cotton at harvest time in the Mississippi Delta. (9 figs.) J. A. Riley. 341–353.
MORELAND, W. B.:
and R. C. Wanta and H. E. Heggestad. Tropospheric ozone: An air pollution problem arising in the Washington, D.C., metropolitan area. (11 figs.) 289–296.

N

The Nashville daily air pollution forecast. (6 figs.) Carl M. Boettger and Harold J. Smith 477–481.
NEILON, JAMES R.:
and John A. Brown. Case studies of numerical wind analyses. (7 figs.) 83–90.
Nephanalysis:
Another view from TIROS I of a severe weather situation—May 16, 1960. (13 figs.) Linwood F. Whitney, Jr. 447–460.
Cloud streets over the Caribbean Sea. (8 figs.) John Schuetz and Sigmund Fritz. 375–382.
Satellite pictures and meteorological analyses of a developing Low in the central United States. (17 figs.) Andrew Timchalk and Lester F. Hubert. 429–445.
A Southern Hemisphere case study with TIROS I data. (13 figs.) Lester F. Hubert. 229–242.
A western Atlantic vortex seen by TIROS I. (7 figs.) J. B. Jones. 383–390.
Nomograms:
Graphical solution of the Penman equation for potential evapotranspiration. (3 figs.) John C. Purvis. 192–196.
Normal heat sources and sinks in the lower troposphere. (10 figs.) Philip F. Clapp. 147–162.
A note on clear air turbulence during April and May 1960. (5 figs.) Frank J. Smigielski. 91–93.

O

The occurrence of anomalous winds and their significance. (13 figs.) M. A. Alaka. 482–494.
O'CONNOR, JAMES F.:
Mean circulation patterns based on 12 years of recent Northern Hemisphere data. (14 figs.) 211–227.
The weather and circulation of November 1960—Another November with a mid-month reversal. (7 figs.) 53–58.
The weather and circulation of April 1961—Persistent blocking in eastern Canada and cool weather in the United States. (6 figs.) 256–262.
On short- and long-term variations in quasi-barotropic flow. (22 figs.) A. Wiin-Nielsen. 461–476.
On the radiative equilibrium and heat balance of the atmosphere. (26 figs.) Syukuro Manabe and Fritz Möller. 503–532.
On verification of upper-air winds by vertical shear and extremes. Oskar M. Essenwanger, Robert E. Bradford, and William W. Vaughan. (3 figs.) 197–204.
Ozone:
Tropospheric ozone: An air pollution problem arising in the Washington, D.C. metropolitan area. (11 figs.) R. C. Wanta, W. B. Moreland, and H. E. Heggestad. 289–296.

P

PACK, D. H.:
and J. K. Angell. Estimation of vertical air motions in desert terrain from tetroon flights. (13 figs.) 273–283.
The precipitation day statistic. (5 figs.) C. K. Vestal. 31–37.
Precipitation:
Excessive rainfall in the Montgomery, Ala. area on August 31, 1961. [Weather note] Arthur R. Long. 501.
The middle Mississippi Valley hydrometeorological storm of May 4–9, 1961. (8 figs.) [Weather note] Jerrold A. LaRue and Russell J. Younkin. 555–559.
The precipitation day statistic. (5 figs.) C. K. Vestal. 31–37.
Rainstorm in southern Florida, January 21, 1957. (8 figs.) [Weather note] Robert H. Sourbeer and R. Cecil Gentry. 9–16.
Precipitation measurement:
Relative catches of snow in shielded and unshielded gages at different wind speeds. (5 figs.) Leonard L. Weiss. 397–400.
The probing of the tropopause by balloons that follow it—A suggestion. [Correspondence] Wan-Cheng Chiu. 297–298.
A proposed staggered-grid system for numerical integration of dynamic equations. (2 figs.) D. K. Lilly. 59–65.
Publications by Weather Bureau authors. 8, 66, 185, 228, 288, 374, 502.
Publications. New Weather Bureau. 7, 52, 66, 186, 446.
PURVIS, JOHN C.:
Graphical solution of the Penman equation for potential evapotranspiration. (3 figs.) 192–196.

R

Radar echo of a mountain wave on February 15, 1960. (4 figs.) [Weather note] DeVer Colson, Charles V. Lindsay, and James H. Hand. 17–19.
Radar meteorology:
The "double eye" of hurricane Donna. (3 figs.) [Weather note] C. L. Jordan and Frank J. Schatzle. 354–356.

Radar meteorology—Continued
Radar echo of a mountain wave on February 15, 1960. (4 figs.) [Weather note] DeVer Colson, Charles V. Lindsay, and James H. Hand. 17–19.
Use of Doppler radar in meteorological observations. (9 figs.) Robert L. Smith and David W. Holmes. 1–7.
Radiation:
On the radiative equilibrium and heat balance of the atmosphere. (26 figs.) Syukuro Manabe and Fritz Möller. 503–532.
Radiation measurements:
Analysis of satellite infrared radiation measurements on a synoptic scale. (11 figs.) Melvin Weinstein and Verner E. Suomi. 419–428.
Accuracy of the airborne economical radiometer. (2 figs.) P. M. Kuhn. 285–287.
Rainstorm in southern Florida, January 21, 1957. (8 figs.) [Weather note] Robert H. Sourbeer and R. Cecil Gentry. 9–16.
Recent articles in other Weather Bureau periodicals. 98, 186, 284, 502, 578.
The reduction of truncation error by extrapolation techniques. (5 figs.) W. Lawrence Gates. 115–124.
Relative catches of snow in shielded and unshielded gages at different wind speeds. (5 figs.) Leonard L. Weiss. 397–400.
Relative motion of hurricane pairs. (7 figs.) Eugene W. Hoover. 251–255.
Riley, J. A.:
Moisture and cotton at harvest time in the Mississippi Delta. (9 figs.) 341–353.
Rocky Mountains:
Lee-side frontogenesis in the Rocky Mountains. (13 figs.) Toby Y. Carlson. 163–172.
Ropar, N. J.:
and T. I. Gray, Jr. Description of the 50-mb. patterns over Antarctica in 1958. (17 figs.) 45–52.

S

Satellite meteorology:
Analysis of satellite infrared radiation measurements on a synoptic scale. (11 figs.) Melvin Weinstein and Verner E. Suomi. 419–428.
Another view from TIROS I of a severe weather situation—May 16, 1960. (13 figs.) Linwood F. Whitney, Jr. 447–460.
Cloud streets over the Caribbean sea. (8 figs.) John Schuetz and Sigmund Fritz. 375–382.
Satellite pictures and meteorological analyses of a developing Low in the central United States. (17 figs.) Andrew Timchalk and Lester F. Hubert. 429–445.
A Southern Hemisphere case study with TIROS I data. (13 figs.) Lester F. Hubert. 229–242.
Satellite meteorology—Continued
A western Atlantic vortex seen by TIROS I. (7 figs.) J. B. Jones. 383–390.
Satellite pictures and meteorological analyses of a developing Low in the central United States. (17 figs.) Andrew Timchalk and Lester F. Hubert. 429–445.
Schatzle, Frank J.:
and C. L. Jordan. The "double eye" of hurricane Donna. (3 figs.) [Weather note] 354–356.
Schuetz, John:
and Sigmund Fritz. Cloud streets over the Caribbean Sea. (8 figs.) 375–382.
Smigielski, Frank J.:
A note on clear air turbulence during April and May 1960. (5 figs.) 91–93.
Smith, Harold J.:
and Carl M. Boettger. The Nashville daily air pollution forecast. (6 figs.) 477–481.
Smith, Robert L.:
and David W. Holmes. Use of Doppler radar in meteorological observations. (9 figs.) 1–7.
Some aspects of a cycle of available potential energy. (9 figs.) Jay S. Winston and Arthur F. Krueger. 307–318.
Some aspects of the thermal energy exchange on the South Polar snowfield and Arctic ice pack. (3 figs.) Kirby J. Hanson. 173–177.
Some experiments on the measurement of natural ice nuclei. (7 figs.) Dwight B. Kline and Glenn W. Brier. 263–272.
Sourbeer, Robert H.:
and R. Cecil Gentry. Rainstorm in southern Florida, January 21, 1957. (8 figs.) [Weather note] 9–16.
A Southern Hemisphere case study with TIROS I data. (13 figs.) Lester F. Hubert. 229–242.
Squall line passage at Barrow, Alaska, June 21, 1960. (4 figs.) [Weather note] Ronald J. McCue, Jr. and G. Philip Weber. 411–413.
Stark, L. P.:
The weather and circulation of February 1961—An example of attenuation in the long-wave pattern. (7 figs.) 178–184.
The weather and circulation of June 1961—A hot dry month in the West. (8 figs.) 368–373.
Stratosphere:
Time section and hodograph analysis of Churchill rocket and radiosonde winds and temperatures. (13 figs.) Sidney Teweles. 125–136.
A study of the effect of tree leaves on wind movement. (4 figs.) Ralph H. Frederick. 39–44.
Sunshine-cloudiness relationships in the United States. (11 figs.) Roy L. Fox. 543–548.
Suomi, Verner E.:
and Melvin Weinstein. Analysis of satellite infrared radiation measurements on a synoptic scale. (11 figs.) 419–428.

T

Temperature:
A comparison of methods for computing daily mean values of dry bulb temperature, dew point, and relative humidity. (10 figs.) Milton L. Blanc. 401–410.
Distributions of weekly averages of diurnal temperature means and ranges about harmonic curves. (6 figs.) Christopher Bingham. 357–367.
The zonal wind field along 80° W. for the IGY period and Northern Hemisphere anomalies of wind and temperature. (8 figs.) William M. McMurray. 549–554.
Temperature inversion:
Low-level inversion frequency in the contiguous United States. (9 figs.) Charles R. Hosler. 319–339.
Temperature. Upper air:
Time section and hodograph analysis of Churchill rocket and radiosonde winds and temperatures. (13 figs.) Sidney Teweles. 125–136.
TEWELES, SIDNEY:
Time section and hodograph analysis of Churchill rocket and radiosonde winds and temperatures. (13 figs.) 125–136.
Three-dimensional pressure pattern of the Dallas tornado and some resultant implications. (9 figs.) Walter H. Hoecker, Jr. 533–542.
TIMCHALK, ANDREW:
and Lester F. Hubert. Satellite pictures and meteorological analyses of a developing Low in the central United States. (17 figs.) 429–445.
Time section and hodograph analysis of Churchill rocket and radiosonde winds and temperatures. (13 figs.) Sidney Teweles. 125–136.
TIROS
Another view from TIROS I of a severe weather situation—May 16, 1960. (13 figs.) Linwood F. Whitney, Jr. 447–460.
Cloud streets over the Caribbean Sea. (8 figs.) John Schuetz and Sigmund Fritz. 375–382.
Satellite pictures and meteorological analyses of a developing Low in the central United States. (17 figs.) Andrew Timchalk and Lester F. Hubert. 429–445.
A Southern Hemisphere case study with TIROS I data. (13 figs.) Lester F. Hubert. 229–242.
A western Atlantic vortex seen by TIROS I. (7 figs.) J. B. Jones. 383–390.
TISDALE, CLIFTON F.:
The weather and circulation of September 1961—Including a discussion of tropical storm activity. (7 figs.) 560–566.
Tornadoes near Nags Head, N.C., in May and June 1960. (6 figs.). [Weather note] Frank B. Dinwiddie. 20–23.
Tornadoes:
Another view from TIROS I of a severe weather situation—May 16, 1960. (13 figs.) Linwood F. Whitney, Jr. 447–460.
Three-dimensional pressure pattern of the Dallas tornado and some resultant implications. (9 figs.) Walter H. Hoecker, Jr. 533–542.
Tornadoes near Nags Head, N.C., in May and June 1960. (6 figs.) [Weather note] Frank B. Dinwiddie. 20–23.
Tropical storms: (See also Hurricanes)
The weather and circulation of September 1961—Including a discussion of tropical storm activity. (7 figs.) Clifton F. Tisdale. 560–566.
Tropopause:
The probing of the tropopause by balloons that follow it—A suggestion. Wan-Cheng Chiu. 297–298.
Tropospheric ozone: An air pollution problem arising in the Washington, D.C. metropolitan area. (11 figs.) R. C. Wanta, W. B. Moreland, and H. E. Heggestad. 289–296.

U

Use of Doppler radar in meteorological observations. (9 figs.) Robert L. Smith and David W. Holmes. 1–7.

V

VAUGHAN, WILLIAM W.:
and Oskar M. Essenwanger and Robert E. Bradford. On verification of upper-air winds by vertical shear and extremes. (3 figs.) 197–204.
VEDERMAN, JOSEPH:
Forecasting precipitation with the aid of a high-speed electronic computer (7 figs.) 243–250.
Vertical motion:
Estimation of vertical air motions in desert terrain from tetroon flights. (13 figs.) J. K. Angell and D. H. Pack. 273–283.
VESTAL, C. K.:
The precipitation day statistic. (5 figs.) 31–37.

W

WANTA, R. C.:
and W. B. Moreland and H. E. Heggestad. Tropospheric ozone: An air pollution problem arising in the Washington, D.C. metropolitan area. (11 figs.) 289–296.
Weather Bureau Technical News:
Electronic weather map "plotter." 38.
New weather facsimile network. 38.
Special slide rule for computing evapotranspiration. 144.
Isotope-powered automatic weather station. 373.

Weather notes:
The "double eye" of hurricane Donna. (3 figs.) C. L. Jordan and Frank J. Schatzle. 354–356.
The effect of differential friction between land and water on the movement of Donna in the vicinity of eastern North Carolina. (1 fig.) Eugene W. Hoover. 340.
Excessive rainfall in the Montgomery, Ala. area on August 31, 1961. Arthur R. Long. 501.
The middle Mississippi Valley hydrometeorological storm of May 4–9, 1961. (8 figs.) Jerrold A. LaRue and Russell J. Younkin. 555–559.
Radar echo of a mountain wave on February 15, 1960. (4 figs.) DeVer Colson, Charles V. Lindsay, and James H. Hand. 17–19.
Rainstorm in southern Florida, January 21, 1957. (8 figs.) Robert Sourbeer and R. Cecil Gentry. 9–16.
Squall line passage at Barrow, Alaska, June 21, 1960. (4 figs.) Ronald J. McCue, Jr. and G. Philip Weber. 411–413.
Tornadoes near Nags Head, N.C. in May and June 1960. (6 figs.) Frank B. Dinwiddie. 20–23.
Weather, U.S.:
The weather and circulation of October 1960. (10 figs.) J. F. Andrews. 24–30.
The weather and circulation of November 1960—Another November with a mid-month reversal. (7 figs.) James F. O'Connor. 53–58.
The weather and circulation of December 1960—An unusually cold month in the United States. (10 figs.) Robert H. Gelhard. 109–114.
The weather and circulation of January 1961. (11 figs.) Raymond A. Green. 137–143.
The weather and circulation of February 1961—An example of attenuation in the long-wave pattern. (7 figs.) L. P. Stark. 178–184.
The weather and circulation of March 1961—Another mild month in the United States. (11 figs.) James F. Andrews. 205–210.
The weather and circulation of April 1961—Persistent blocking in eastern Canada and cool weather in the United States. (6 figs). James F. O'Conner. 256–262.
The weather and circulation of May 1961—Persistent cool weather in the United States. (10 figs.) Robert H. Gelhard. 299–305.
The weather and circulation of June 1961—A hot dry month in the West. (8 figs.) L. P. Stark. 368–373.
The weather and circulation of July 1961. (9 figs.) Raymond A. Green. 414–418.
The weather and circulation of August 1961—Record heat from the northern Plains to the Pacific coast. (6 figs.) James F. Andrews. 495–500.
The weather and circulation of September 1961—Including a discussion of tropical storm activity. (7 figs.) Clifton F. Tisdale. 560–566.
Weber, G. Philip:
and Ronald J. McCue, Jr. Squall line passage at Barrow, Alaska, June 21, 1960. (4 figs.) [Weather note] 411–413.
Weinstein, Melvin:
and Verner E. Suomi. Analysis of satellite infrared radiation measurements on a synoptic scale. (11 figs.) 419–428.
Weiss, Leonard L.:
Relative catches of snow in shielded and unshielded gages at different wind speeds. (5 figs.) 397–400.
A western Atlantic vortex seen by TIROS I. (7 figs.) J. B. Jones. 383–390.
Whitney, Linwood F., Jr.:
Another view from TIROS I of a severe weather situation—May 16, 1960. (13 figs.) 447–460.
Wiin-Nielsen, A.:
Diagnosis of divergence in a three-parameter numerical prediction model. (5 figs.) 67–73.
On short- and long-term variations in quasi-barotropic flow. (22 figs.) 461–476.
Winds:
Computation and uses of gradient winds. (1 fig.) Roy M. Endlich. 187–191.
The occurrence of anomalous winds and their significance. (13 figs.) M. A. Alaka. 482–494.
On verification of upper-air winds by vertical shear and extremes. Oskar M. Essenwanger, Robert E. Bradford, and William W. Vaughan. (3 figs.) 197–204.
A study of the effect of tree leaves on wind movement. (4 figs.) Ralph H. Frederick. 39–44.
The zonal wind field along 80° W. for the IGY period and Northern Hemisphere anomalies of wind and temperature. (8 figs.) William M. McMurray. 549–554.
Winds, Upper air:
Time section and hodograph analysis of Churchill rocket and radiosonde winds and temperatures. (13 figs.) Sidney Teweles. 125–136.
Winston, Jay S.:
and Arthur F. Krueger. Some aspects of a cycle of available potential energy. (9 figs.) 307–318.

Y

Younkin, Russell J.:
and Jerrold A. LaRue. The middle Mississippi Valley hydrometeorological storm of May 4–9, 1961. (8 figs.) [Weather note] 555–559.

Z

The zonal wind field along 80° W. for the IGY period and Northern Hemisphere anomalies of wind and temperature. (8 figs.) William M. McMurray. 549–554.

Recent Articles in Other Weather Bureau Periodicals

Mariners Weather Log, vol. 5

No. 6, November 1961:

"The U.S. Navy Hydrographic Office Ice Observing and Forecasting Program," by R. J. Perchal and S. O. Marcus, pp. 193–196.

"Cyclone Tracks Near Blocking Highs," by H. E. Rosental, pp. 196–199.

Weekly Weather and Crop Bulletin, National Summary, vol. XLVIII

No. 44, October 30, 1961:

"Relative Humidity," with a table of percent frequency of specified relative humidity values at selected hours during mid seasonal months, p. 8.

U. S. GOVERNMENT PRINTING OFFICE: 1961

QC
983
.A27

MONTHLY WEATHER REVIEW

VOLUME 89 NUMBER 12

DECEMBER 1961

CONTENTS

	Pages
On the Radiative Equilibrium and Heat Balance of the Atmosphere — Syukuro Manabe and Fritz Möller	503–532
Three-Dimensional Pressure Pattern of the Dallas Tornado and Some Resultant Implications — Walter H. Hoecker, Jr.	533–542
Sunshine-Cloudiness Relationships in the United States — Roy L. Fox	543–548
The Zonal Wind Field Along 80° W. for the IGY Period and Northern Hemisphere Anomalies of Wind and Temperature — William M. McMurray	549–554
Weather Note: The Middle Mississippi Valley Hydrometeorological Storm of May 4–9, 1961 — Jarrold A. LaRue and Russell J. Younkin	555–559
The Weather and Circulation of September 1961—Including a Discussion of Tropical Storm Activity — Clifton F. Tisdale	560–566
Contents, Volume 89	567–569
Correction Notices	569
Index, Volume 89	570–577
Recent Articles in Other Weather Bureau Periodicals	578

U.S. DEPARTMENT OF COMMERCE • WEATHER BUREAU

The Weather Bureau desires that the *Monthly Weather Review* serve as a medium of publication for original contributions within its field, but the publication of a contribution is not to be construed as official approval of the views expressed.

In order to maintain the schedule with the Public Printer, no proofs will be sent to authors outside of Washington, D.C.

Use of funds for printing this publication has been approved by the Director of the Bureau of the Budget, January 3, 1961.

PUBLICATIONS OF THE U.S. WEATHER BUREAU

As the national meteorological service for the United States, the Weather Bureau issues several periodicals, serials, and miscellaneous publications on weather, climate, and meteorological science as required to carry out its public service functions. The principal periodicals and serials are described on this page and on the inside of the back cover. A more complete listing of Weather Bureau publications is available upon request to the Chief, U.S. Weather Bureau, Washington 25, D.C.

Orders for publications should be addressed to the Superintendent of Documents, Government Printing Office, Washington 25, D.C.

MONTHLY WEATHER REVIEW

First published in 1872, the *Monthly Weather Review* serves as a medium of publication for technical contributions in the field of meteorology, principally in the branches of synoptic and applied meteorology. In addition each issue contains an article descriptive of the atmospheric circulation during the month over the Northern Hemisphere with particular reference to the effect on weather in the United States. Illustrated. Annual subscription: $4.00; additional for foreign mailing, $1.00; 40¢ per copy. Subscription to the *Review* does not include the *Supplements* which have been issued irregularly and are for sale separately.

WEEKLY WEATHER AND CROP BULLETIN

Issued on Tuesday of each week. A summary of the weather of the week and its effect on crops and farm activities over the entire country is presented with short reports from individual States supplemented by maps of average temperature and total precipitation for the week and for the month. For the winter months a snow depth chart is included along with a table of ice conditions on rivers and lakes. Descriptions of, and data on, current unusual conditions, such as drought, floods, blizzards, etc., are offered, often with charts. Short articles on the application of weather data to agricultural and industrial pursuits are included. Annual subscription: $3.00; additional for foreign mailing, $1.00; 10¢ per copy. For period December through March, $1.50; additional for foreign mailing, 50¢.

CLIMATOLOGICAL DATA

This monthly and annual publication presents detailed daily and monthly data in 46 sections for the United States, the Pacific, and the West Indies and Caribbean. Annual subscription $2.50 per section; additional for foreign mailing, $1.00; 20¢ per monthly issue.

Climatological Data National Summary contains monthly and annual data such as pressure, temperature, wind, rainfall, snowfall, and floods for the United States as a whole. A short article describing the weather of the month over the United States, tables of observational data, and a description of flood conditions are supplemented by a number of charts. Annual subscription, $4.00; additional for foreign mailing, $1.50; 30¢ for monthly issues; 50¢ for the annual.

LOCAL CLIMATOLOGICAL DATA

Issued monthly for cities in which Weather Bureau stations are located, this publication consists of a single sheet listing the daily observational data for the station, from both city and airport offices, when obtainable, and an annual issue describing the average climate and with tables of data for the current and past years. Subscription price (including annual): $1.00 per year; single issue 10 cents each, 15 cents for the annual. Most stations also issue a Supplement to cover hourly observations. Subscription price: $1.00 per year; single issues 10 cents (no annual). Both the Local Climatological Data (including annual) and the Supplement can be obtained for $1.50 per year. Additional for foreign mailing is $1.00.

(Continued on inside back cover)

PUBLICATIONS OF THE U.S. WEATHER BUREAU

(Continued from inside front cover)

STORM DATA

A monthly periodical beginning with January 1959 issue. Contains tables of storms and storm damage reported during month. Formerly part of *Climatological Data—National Summary*. Price: 15¢ per copy, annual subscription, $1.50 domestic, $2.00 foreign.

DAILY RIVER STAGES

Annual publication of daily river stages for about 625 stations on the principal rivers of the United States, with added data on elevation, drainage area, flood stage, and extreme stages for each station. Prices vary.

DAILY WEATHER MAP

Printed and distributed daily from Washington, D.C. This map consists of a 24″ x 19″ sheet on which is printed a large map of the United States showing the surface weather conditions as of 1:00 a.m., EST, and 2 small maps of North America, one showing the surface analysis at the 1:00 p.m., EST, the other the 500-mb. analysis at the 6:00 p.m., EST, previous to the large map. Precipitation areas and amounts and high and low temperatures for the 24 hours previous to the large map are also given. Occasionally short descriptive articles on some phase of applied meteorology or the Bureau's work are printed on the map back. Annual subscription: $9.60; $2.40 for 3 months (minimum subscription accepted).

AVERAGE MONTHLY WEATHER RÉSUMÉ AND OUTLOOK

A semimonthly publication presenting for the coming 30 days by means of charts the expected patterns of average temperature and precipitation over the United States and the average atmospheric circulation patterns for the same 30-day period. Also given are corresponding charts for the past 30-day period showing the observed averages. A brief description of expected conditions is included. These charts are best suited for use where a general picture of future conditions over a wide area is needed. They should be used in conjunction with the short-term forecasts issued by the nearest Weather Bureau Office. Annual subscription: $5.00; $2.50 for 6 months (minimum subscription accepted).

RESEARCH PAPERS

The research paper series and the technical paper series described below are issued at irregular intervals as the material becomes available. Each Research Paper is a report of original research in which at least part of the answer to a specific meteorological problem has been worked out and is presented as a contribution to knowledge of the weather. Forty-three have so far been issued covering such subjects as precipitation forecasting for the TVA basin, the artificial production of precipitation, the application of the hydraulic analogy to atmospheric flow problems, etc. Prices vary.

TECHNICAL PAPERS

This series contains compilations of meteorological and climatological data on such topics as temperatures in the upper air, daily total solar and sky radiation, thunderstorm days in the United States, normal maps for the Northern Hemisphere, etc. Thirty-nine have been issued so far. Prices vary.

UNIVERSITY OF MICHIGAN
NATURAL SCIENCE LIBRARY
1025 ANN ARBOR MICH

UNITED STATES
GOVERNMENT PRINTING OFFICE
DIVISION OF PUBLIC DOCUMENTS
WASHINGTON 25, D.C.

OFFICIAL BUSINESS

PENALTY FOR PRIVATE USE TO AVOID
PAYMENT OF POSTAGE, $300